Design and Implementation of Magnetic Levitation Based Modular Omnidirectional Conveyor System

by

Chanuphon Trakarnchaiyo

A thesis
presented to the University of Waterloo
in the fulfillment of the
thesis requirement for the degree of
Doctor of Philosophy
in
Mechanical and Mechatronics Engineering

Waterloo, Ontario, Canada, 2023

© Chanuphon Trakarnchaiyo 2023

Examining Committee Membership

The following served on the Examining Committee for this thesis. The decision of the Examining Committee is by majority vote.

External Examiner:	Mehrdad Radji Kermani Professor Department of Electrical and Computer Engineering Western University
Supervisor:	Mir Behrad Khamesee Professor Department of Mechanical and Mechatronics Engineering University of Waterloo
Internal Member:	Amir Khajepour Professor Department of Mechanical and Mechatronics Engineering University of Waterloo
	Marco Alfano Associate Professor Department of Mechanical and Mechatronics Engineering University of Waterloo
Internal-External Member:	Eihab Abdel-Rahman Professor Department of Systems Design Engineering University of Waterloo

Author's Declaration

This thesis consists of material all of which I authored or co-authored: see Statement of Contributions included in the thesis. This is a true copy of the thesis, including any required final revisions, as accepted by my examiners.

I understand that my thesis may be made electronically available to the public.

Statement of Contributions

Chanuphon Trakarnchaiyo was the sole author for Chapters 1, 3, 5, 7 and 8, which were written under the supervision of Dr. Behrad Khamesee and were not written for publication.

The thesis consists in part of three manuscripts written for publication. Exception to sole authorship of material are as follows:

Preliminary work on the MagTable presented in Chapter 2:

This research was conducted by two postdoctoral fellows—Dr. Xiaodong Zhang and Dr. Heng Zhang—and Chanuphon Trakarnchaiyo under the supervision of Dr. Behrad Khamesee at the University of Waterloo. Chanuphon Trakarnchaiyo conducted an analysis on a comparison of cylindrical and square coil arrays and participated in other analyses and experiments conducted by Dr. Xiaodong Zhang and Dr. Heng Zhang. The manuscript was prepared by Dr. Xiaodong Zhang with contributions from all co-authors.

Xiaodong Zhang, Chanuphon Trakarnchaiyo, Heng Zhang, and Mir Behrad Khamesee, "Magtable: A tabletop system for 6-DOF large range and completely contactless operation using magnetic levitation," *Mechatronics*, vol. 77, p. 102600, 2021.

Work on the 10-Coil Testbed presented in Chapters 4 and 6:

This research was conducted by Chanuphon Trakarnchaiyo and Yang Wang under the supervision of Dr. Behrad Khamesee at the University of Waterloo. Chanuphon Trakarnchaiyo conducted an analysis and design of a square coil array. Yang Wang was a primary coder. Chanuphon Trakarnchaiyo and Yang Wang conducted experiments. The manuscript was prepared by Chanuphon Trakarnchaiyo with contributions from all co-authors.

Chanuphon Trakarnchaiyo, Yang Wang, and Mir Behrad Khamesee, "Design of a compact planar magnetic levitation system with wrench–current decoupling enhancement," *Applied Sciences*, vol. 13, no. 4, 2023.

Work on the Maglev Floor Prototype presented in Chapter 4:

This research was conducted by Zhenchuan Xu, Chanuphon Trakarnchaiyo, and Curtis Stewart under the supervision of Dr. Behrad Khamesee at the University of Waterloo. Chanuphon Trakarnchaiyo conducted an analysis and design of the prototype system and participated in the experiments conducted by Zhenchuan Xu and Curtis Stewart. The manuscript was prepared by Zhenchuan Xu with contributions from all co-authors.

Zhenchuan Xu, Chanuphon Trakarnchaiyo, Curtis Stewart, and Mir Behrad Khamesee, "Modular Maglev: Design and implementation of a modular magnetic levitation system to levitate a 2D Halbach array," submitted to *Mechatronics* on August 16, 2022.

Abstract

Smart manufacturing is now required to be more intelligent and flexible to support mass customization. Magnetic levitation or maglev technology can increase the flexibility of modern manufacturing with its advantages of low friction and multi-directional motion. Two promising industrial applications of maglev are planar motors and precision stages.

This research aims to develop a novel planar maglev system, Magnetic Levitation Floor, and implement it as an omnidirectional conveyor. The contributions of this research are the design and analysis of a novel modular planar electromagnet stator and permanent magnet mover, wrench–current decoupling enhancement using multivariate linear interpolation, and the development of a decoupling strategy for long-range motion.

For maglev system development, the planar electromagnet stator is an array of square coil modules. The coil was designed to attain optimal levitation force with efficient power. The support frame has a modular structure for unlimited expansion and flexible layouts. Two planar maglev prototypes, 10-Coil Testbed and Maglev Floor Prototype, were built in addition to the Maglev Floor system for pilot testing. Next, a four-disc magnet mover was designed to achieve six-degrees-of-freedom motion. The magnet layout was optimized with analyses on condition number, maximum current, and power consumption.

For real-time levitation control, the cross-coupling effect in the system is decoupled by a wrench–current decoupling matrix. The Lorentz force-based wrench matrices are pre-computed and stored in the lookup table. With discrete lookup data, however, the levitation performance can deteriorate when the mover levitated at pose without data, especially in rotations. In this work, a multivariate linear interpolation was implemented to improve wrench–current decoupling effectiveness between lookup data.

For conveying applications, another limitation of the decoupling method using a lookup table is the storage usage which is directly proportional to the data range. To achieve long-range planar motion with efficient use of data storage, the decoupling strategy with small-range lookup data was developed in this work. The lookup data has the range of quarter coil area. The active coil set is selected from the mover location. Then, the wrench matrix is estimated from lookup data and mover pose relative to the active coil set.

The feasibility of flexibility enhancement in smart manufacturing using the designed planar maglev system was evaluated through long-range and fine motion experiments. The multivariate linear interpolation significantly improved the levitation performance which suffered from discrete data switching. The decoupling strategy enabled the mover to traverse the levitation area. Experiment results demonstrated the capability of the system for real-world omnidirectional conveying applications.

Acknowledgements

First of all, I would like to sincerely thank my supervisor, Prof. Mir Behrad Khamesee, for giving me this great opportunity to be the first PhD student of the Maglev Floor project. His patience and advice guided me from scratch through my research at the University of Waterloo. Next, I would like to thank my PhD thesis committee: Prof. Amir Khajepour, Prof. Marco Alfano, Prof. Eihab Abdel-Rahman, and Prof. Mehrdad Radji Kermani for their valuable comments and suggestions to improve my research.

I would like to thank the UW faculty and staff for their kind support of this project. RoboHub Director: Prof. William Melek, Manager: Dr. Brandon J. DeHart, and Staff: Alexander Werner and Robert Wagner for their support; MME electronics technician: Neil Griffett for his great helps, especially, during the pandemic; Engineering Machine Shop Manager: Rick Forgett, Lead hand: Mark Kuntz, and everyone in the EMS for their expertise in machining, welding, and fabrication.

Next, my colleagues and friends, former and current members of the Maglev Floor project: Dr. Xiaodong Zhang, Dr. Heng (Henry) Zhang, Dr. Hassan Askari, Dr. Moslem Sadeghi-Goughari, Zhenchuan (Daniel) Xu, Yang (Bob) Wang, Curtis Stewart, and Ridwan Bari; Maglev Microrobotics Laboratory members: Dr. Heba Elsayed Farag, Dr. Parichit Kumar, Azeem Singh Kahlon, Pooriya Kazemzadeh Heris, Saksham Malik, Yashesh Dasari, Joseph Nofech, and Afarin Khabbazian; and the University of Waterloo Thai Student Association (UW-TSA) members. May you all have a prosperous future.

I gratefully thank my teachers at King Mongkut's University of Technology Thonburi (KMUTT) and Asian Institute of Technology (AIT) for the great inspiration that has motivated me to come this far.

Last but not least, my family, I cannot thank you enough for their countless support and encouragement throughout these years of my study.

This research work was supported by the Canada Foundation for Innovation (CFI) and the Natural Sciences and Engineering Research Council of Canada (NSERC).

My PhD study at the University of Waterloo was financially supported by the Royal Thai Government Scholarship from Thailand.

Table of Contents

List of Tables xi

List of Figures xiii

List of Symbols and Units xviii

1 Introduction 1

1.1 Motivation 1

1.2 Research Objectives 4

1.3 Research Contributions 5

1.4 Thesis Outline 6

2 Background and Preliminary Study 8

2.1 Magnetic Levitation Technology 8

2.2 Research on Magnetic Levitation Stages 10

2.3 Coil Design and Fabrication 18

2.4 Magnetic Levitation Modeling and Control 20

2.5 Preliminary Study: MagTable 28

2.6 Summary 36

I Modular Planar Magnetic Levitation System Design 37

3 Magnetic Levitation Modeling 38

3.1 Lorentz Levitation Model . . . 38
3.1.1 Magnetic Flux Density Computation . . . 40
3.1.2 Magnetic Force and Torque Computation . . . 41
3.1.3 Model Validation . . . 46
3.2 Model Implementation for Real-Time Wrench–Current Decoupling . . . 51
3.2.1 Wrench–Current Decoupling . . . 51
3.2.2 Lookup Table Method . . . 52
3.3 Wrench–Current Decoupling Enhancement Using Multivariate Linear Interpolation . . . 53
3.4 Wrench–Current Decoupling Strategy for Long-Range Planar Motion . . . 55
3.5 Summary . . . 58

4 Planar Coil Array Stator 59

4.1 Electromagnets . . . 59
4.2 Maglev Prototype: 10-Coil Testbed . . . 65
4.3 Magnetic Levitation Floor and Prototype (Proto-MagFloor) . . . 68
4.3.1 Conceptual Design . . . 68
4.3.2 Coil Module . . . 68
4.3.3 Modular Planar Stator Unit . . . 72
4.3.4 Maglev Prototype: Maglev Floor Prototype (Proto-MagFloor) . . . 74
4.3.5 Magnetic Levitation Floor . . . 76
4.4 Summary . . . 78

5 Disc-Magnet Mover 79

5.1 Single-Disc Magnet Mover . . . 79
5.2 Multiple-Disc Magnet Mover . . . 81
5.3 Summary . . . 88

II System Implementation **89**

6 Implementation on 10-Coil Testbed **90**

6.1 10-Coil Testbed System Setup . . . 90

6.1.1 System Setup . . . 90

6.1.2 Lookup Table . . . 91

6.1.3 Multivariate Linear Interpolation . . . 92

6.1.4 Control System . . . 93

6.2 Experiment Results on 10-Coil Testbed . . . 94

6.2.1 Linear Interpolation Performance Verification . . . 94

6.2.2 Step and Microstep Responses . . . 96

6.2.3 Full-Range Trajectory Tracking . . . 99

6.3 Summary . . . 103

7 Implementation on Magnetic Levitation Floor Prototype **104**

7.1 Magnetic Levitation Floor Prototype (Proto-MagFloor) System Setup . . . 104

7.1.1 System Setup . . . 104

7.1.2 Lookup Table . . . 105

7.1.3 Multivariate Linear Interpolation . . . 107

7.1.4 Control System and Long-Range Decoupling Strategy . . . 107

7.2 Experiment Results on Proto-MagFloor: Single-Disc Magnet Mover . . . 110

7.2.1 Step Motion Responses and Interpolation Implementation . . . 110

7.2.2 Long-Range Trajectory Tracking . . . 113

7.3 Experiment Results on Proto-MagFloor: Multiple-Disc Magnet Mover . . . 118

7.3.1 Step Motion Responses . . . 118

7.3.2 Long-Range Trajectory Tracking . . . 121

7.4 Summary . . . 129

8 Conclusions **130**

8.1 Conclusions 130

8.2 Future Works 132

References **133**

APPENDICES **143**

A Simulation Settings **144**

A.1 ANSYS: Cylindrical and Square Coils 144

A.2 ANSYS: Vertical Force between Disc Magnet and Coil with Different Heights 145

A.3 ANSYS: Forces and Torques between Single-Coil Single-Magnet for Wrench Model Validation 146

A.4 ANSYS: Straight and Zigzag Coil Array 148

A.5 ANSYS: Coil Array with Steel Sheet 149

A.6 SolidWorks: Stress Analysis on Steel Table 150

B List of Publications **151**

B.1 Published Journal Articles 151

B.2 In-process Journal Articles 151

List of Tables

2.1 Review of previous research works on planar maglev stages. 11
2.2 Comparison of commercial planar maglev stage products. 17
2.3 MagTable: Coil parameters 30
2.4 Mass properties of three movers. 31

3.1 Gaussian node and weight for number of points $N = 1$ to 4. 41
3.2 Permanent disc magnet specifications 46
3.3 Force and torque sensor specifications. 48
3.4 Force and torque measurement and simulation parameters. 49
3.5 Lookup first row index weight for each DOF. 52
3.6 Multivariate linear interpolation. 54

4.1 Simulation (I): Magnetic flux density comparison between square and cylindrical coils. 61
4.2 Simulation (II): Parametric simulation of the force between a square coil and a single-disc magnet. 63
4.3 Coil parameters 64
4.4 Square coil array configuration parameters. 66
4.5 Compact planar maglev system specifications. 67

5.1 Condition number comparison between 2-inch, 3-inch, and 4-inch Neodymium disc magnets grade N52 with 20 mm levitation gap. 80

5.2 Mass properties of the designed movers. 88

6.1 10-Coil Testbed: 5-DOF lookup data range for a single-disc magnet mover. 92
6.2 10-Coil Testbed: 5-DOF PID controller parameters. 94
6.3 10-Coil Testbed: 5-DOF step response characteristics. 96

7.1 Proto-MagFloor: 5-DOF lookup data range for a single-disc magnet mover. 106
7.2 Proto-MagFloor: 6-DOF lookup data range for a four-disc magnet mover. . 106
7.3 Proto-MagFloor: 5-DOF PID controller parameters for a single-disc magnet mover. 108
7.4 Proto-MagFloor: 6-DOF PID controller parameters for a four-disc magnet mover. 108

A.1 Simulation settings: Comparison between cylindrical and square coils in Figure 4.2. 144
A.2 Parametric simulation settings: Vertical force in Figure 4.3. 145
A.3 Parametric simulation settings: Forces and torques validation in Figure 3.6b. 146
A.4 Simulation settings: Array configuration comparison in Figure 4.5. 148
A.5 Parametric simulation settings: 4-by-4 coil array with steel sheet in Figure 4.8a. 149
A.6 Simulation settings: Steel Table with Vertical Load in Figure 4.11. 150

List of Figures

1.1 Examples of products for flexible manufacturing. 2

1.2 Graphical diagram highlighting the research progress. 7

2.1 Types of magnetic levitation techniques [37, 38]. 9

2.2 Planar maglev stages from previous works. 12

2.3 Commercial planar maglev stage products. 17

2.4 Fabry factor plot. 18

2.5 Orthocyclic winding with equal number of turns per layer. 19

2.6 Single-coil single-magnet model with the notation of 3-D wrench (forces and torques) on the magnet 21

2.7 Rectangular bar magnet and equivalent current model 22

2.8 Cubic magnet and equivalent charge model 22

2.9 Magnetic node representation of cubic permanent magnet (F. Bancel, 1999) [88] 24

2.10 Planar maglev system plant diagram with cross-coupling effect in current-to-wrench conversion. 25

2.11 Feedback control diagram for a planar maglev system with a decoupling matrix $\mathbf{K}^{+}$. 27

2.12 MagTable system overview. 28

2.13 MagTable: Electromagnet array stator. 29

2.14 Magnetic field comparison between round **(left)** and square **(right)** coil array at 20 mm above the array. 29

2.15 MagTable: Movers tested in the experiment. 30
2.16 Three-disc magnet mover design: Condition number. 31
2.17 Three-disc magnet mover design: Total energy consumption and maximum current in 70 coils with various R at different levitation locations. 32
2.18 Comparison of performance among three movers. 32
2.19 MagTable: Hardware connection diagram. 33
2.20 MagTable: 6-DOF motion control diagram. 34
2.21 MagTable experiment results: Step motion. 35
2.22 MagTable experiment results: High-speed sweep motion. 35

3.1 Coordinate systems in planar magnetic levitation. 39
3.2 Coil sections. 42
3.3 Gaussian nodes on the coil. **(a)** Isometric view. **(b)** Top view with current direction. 42
3.4 Disc-shaped permanent magnet model in ANSYS and magnetic node representation 46
3.5 Magnetic field comparison above disc-shaped permanent magnet along X-axis at z = 20 mm 47
3.6 Force and torque measurement setup and simulation model. 49
3.7 Forces and torques comparison. 50
3.8 Wrench–current decoupling strategy for long-range planar motion. 57

4.1 Round-corner square coil with key dimensions. **(a)** Top view. **(b)** Side view. 60
4.2 Magnetic flux density comparison between cylindrical and square coils along the diagonal distance from center to corner at different heights. 62
4.3 Normalized Fabry factor (red ♦) and normalized z-component of the force (blue ●) on a 4-inch diameter × 1/2-inch thickness disc magnet grade N50 with a 20 mm gap above the center of a square coil with different numbers of vertical turns. 63
4.4 Actual square coil. 64

4.5 Magnetic flux density on the area of 300 mm × 300 mm at 20 mm above the 9-coil array with **(a)** straight configuration, **(b)** zigzag configuration. . 66
4.6 Compact planar maglev prototype structure. 67
4.7 Waterloo RoboHub pit as-built with dimensions in millimeters. 69
4.8 Magnetic field at 20 mm above the 4-by-4 coil array. **(a)** ANSYS simulation with and without steel sheet. **(b)** Magnetic field line plot from −100 mm to 100 mm along Y-axis. 70
4.9 CAD model of the coil module. 71
4.10 Actual coil module. 71
4.11 Stress analysis setup. **(a)** Vertical force 7200 N. **(b)** Model mesh. 72
4.12 Stress analysis result: von Mises stress. 73
4.13 Stress analysis result: displacement. 73
4.14 Maglev Floor Prototype (Proto-MagFloor). **(left)** CAD design. **(right)** Actual system. 75
4.15 Proto-MagFloor: System diagram 75
4.16 Magnetic Levitation Floor (Maglev Floor, MagFloor): CAD design 77
4.17 RoboHub Maglev Floor: Actual system 77

5.1 Condition number plot of wrench matrices between 2-inch, 3-inch, and 4-inch diameter and 1/2-inch thickness disc magnets grade N52 and 3-inch square coil with 20 mm levitation gap. 80
5.2 Single 4-inch disc magnet mover 80
5.3 Four-disc magnet layout 81
5.4 Four disc magnet analysis: Condition number map at 20 mm gap with various R. 82
5.5 Four disc magnet analysis: Max current map at 20 mm gap with various R and vertical force 15 N. 83
5.6 Four disc magnet analysis: Total power consumption map at 20 mm gap with various R and vertical force 15 N. 84
5.7 Four disc magnet analysis: Overall analyzed maximum-minimum-average values at 20 mm gap with various R and vertical force 15 N. 85

5.8 Four disc magnet analysis: Condition number, maximum current, and total power consumption map at 20 mm gap and vertical force 15 N with $R = 40$ mm and various yaw angles. 86
5.9 Four-disc magnet mover. **(a)** CAD model. **(b)** Actual mover. 87

6.1 10-Coil Testbed: Overall system setup. 91
6.2 10-Coil Testbed: 5-DOF PID control diagram 93
6.3 x–y and ψ–θ axes interpolation results: **(a)** step responses without linear interpolations. **(b)** step responses with 2-D linear interpolations. 95
6.4 All axes step responses. 97
6.5 All axes fine step responses. 98
6.6 The disc magnet mover levitated at 26 mm and rotated with pitch angle of 10 degrees. 99
6.7 Full-range trajectory following. 100
6.8 Full-range trajectory following performance. 101
6.9 ψ–θ axes ramp responses. 102

7.1 Proto-MagFloor: System setup. 105
7.2 Proto-MagFloor: Multi-DOF PID control diagram. 108
7.3 Proto-MagFloor: TwinCAT program user interface. 109
7.4 Simulink task processing time in TwinCAT program. 109
7.5 Proto-MagFloor with a single 4-inch disc magnet mover. 110
7.6 Proto-MagFloor single 4-inch PM experiment results 1: 5-DOF step motion. **(left)** without interpolation. **(right)** with interpolation. 111
7.7 Proto-MagFloor single 4-inch PM experiment results 2: Fine step motion. . 112
7.8 Proto-MagFloor single 4-inch PM experiment results 3: X-Y-Z full-range motion. 113
7.9 Proto-MagFloor single 4-inch PM experiment results 4: X-Y-Z full-range motion with 5-DOF responses. 114
7.10 Proto-MagFloor single 4-inch PM experiment results 5: Roll and Pitch full-range motion. 116

7.11 Proto-MagFloor single 4-inch PM experiment results 6: In-place rotation ±10 degrees. . . . 117
7.12 Proto-MagFloor single 4-inch PM experiment results 7: In-place rotation ±20 degrees. . . . 117
7.13 Proto-MagFloor with a four 2-inch disc magnet mover. . . . 118
7.14 Proto-MagFloor four 2-inch PM experiment results 1: 6-DOF step motion. 119
7.15 Proto-MagFloor four 2-inch PM experiment results 2: X-Y-Z fine step motion. 120
7.16 Proto-MagFloor four 2-inch PM experiment results 3: Roll-Pitch-Yaw fine step motion. . . . 120
7.17 Proto-MagFloor four 2-inch PM experiment results 4: ±75 mm XY-plane long-range motion. . . . 122
7.18 Proto-MagFloor four 2-inch PM experiment results 5: ±150 mm XY-plane long-range motion. . . . 123
7.19 Proto-MagFloor four 2-inch PM experiment results 6: ±10 degrees Roll and Pitch full-range motion. . . . 125
7.20 Proto-MagFloor four 2-inch PM experiment results 7: ±10 degrees Roll and Pitch in-place rotation. . . . 126
7.21 Proto-MagFloor four 2-inch PM experiment results 8: 360 degrees Yaw rotation with angular speed of 180 deg/s. . . . 127
7.22 Proto-MagFloor four 2-inch PM experiment results 8: Other DOF responses. 128

A.1 ANSYS coil models. **(a)** Cylindrical coil. **(b)** Square coil. . . . 144
A.2 ANSYS single-coil single-disc magnet model. **(a)** Isometric view. **(b)** Front view. . . . 145
A.3 ANSYS measurement setup model with a motion path. **(a)** Front view. **(b)** Top view. . . . 147
A.4 ANSYS coil array models. **(a)** Straight configuration. **(b)** Zigzag configuration. . . . 148
A.5 ANSYS coil array with steel sheet model. **(a)** Isometric view. **(b)** Front view. 149
A.6 SolidWorks stress analysis setup. **(a)** Vertical force 7200 N. **(b)** Model mesh. 150

List of Symbols and Units

Unit convention: The units used in this thesis are intended to be SI units. However, most of the structural materials used in this work are available in imperial units. Therefore, the equivalent value in imperial units will be provided in parentheses along with the SI units. Additionally, the angle unit is mainly represented in the degree unit. The radian unit is used where necessary.

The following list provides descriptions of the symbols, which are frequently used in this thesis. Any modifications or exceptions to this list will be described where it appears.

${}^{i}[\ ]_{k}^{j}$	matrix representation of a vector/matrix of k in $\{i\}$ coordinate with operation j
$\boldsymbol{A}$, $\boldsymbol{a}$	general vector
$\mathbf{A}$, $\mathbf{a}$	general matrix
A, a	scalar
a_s	linear interpolation weighting parameter
B_r	remanence or remanent magnetization or residual magnetization
G	Fabry factor
$\mathbf{I}$	identity matrix
$\boldsymbol{i}$	current vector
$\boldsymbol{J}$, $\boldsymbol{j}$	current density vectors
$\mathbf{K}$	wrench matrix
$\mathbf{K}^{+}$	decoupling matrix

$\boldsymbol{p}$	position vector $\boldsymbol{p} = [\, x,\, y,\, z \,]^{\mathsf{T}}$
$\boldsymbol{q}$	orientation vector with roll (ϕ), pitch (θ), and yaw (ψ); $\boldsymbol{q} = [\, \phi,\, \theta,\, \psi \,]^{\mathsf{T}}$
$\boldsymbol{r}$	moment arm
$\boldsymbol{w}$	wrench vector or the vector of forces $\boldsymbol{F}$ and torques $\boldsymbol{T}$, where $\boldsymbol{w} = [\, \boldsymbol{F} \;\; \boldsymbol{T} \,]^{\mathsf{T}}$

Chapter 1

Introduction

1.1 Motivation

Customer requirements and technological advancements affect the manufacturing process in various ways. The requirements are diverse which causes the product life cycle becomes shorter. Customized products on the same model such as cars or computers cause a change in the nature of the production system from low-mixed high-volume manufacturing to high-mixed low-volume manufacturing or mass customization [1]. The traditional manufacturing system, which dedicates to mass production no longer suits the current situation. For example, most of the production lines utilize the traditional conveyor, which costs long machine downtime in changing the layout for different products.

The smart factory with the concept of a flexible manufacturing system (FMS) has been proposed [2] and developed throughout the decades to support various customer desires. Some examples of this system are versatile computer numerical control (CNC) machines which can instantly change the operation program based on the model selection, the flexible transfer lines which deliver the parts to each machine for individual operation, and flexible manufacturing cells which handle a group of products.

The flexibility in the manufacturing system can be classified into eight types [3, 4] including machine flexibility, expansion flexibility, operation flexibility, product flexibility, process flexibility, routing flexibility, volume flexibility, and production flexibility. The components of flexible manufacturing systems are categorized as machine tools, material handling systems, storage areas for in-process inventory, and computer control, which are used to classify the differences between each flexible manufacturing system.

Based on the flexibility and component of the system, there are four types of flexible manufacturing systems: flexible machining cell, flexible machining system, flexible transfer line, and flexible transfer multi-line. In large factories, the conveyor systems are important. Currently, the system should handle the shorter product life cycle and product variations while maintaining a smooth production flow. Hence, the concept of flexible manufacturing is applied to design the process. However, traditional conveyor systems have problems with mechanical constraints and low flexibility to change rapidly, which cannot support flexible manufacturing.

Several products were developed to provide flexible transfer systems. One example of a product that supports the flexible manufacturing system is a cellular conveyor, Celluveyor [5], as shown on the left side in Fig. 1.1. This product can flexibly mobilize objects in any horizontal direction with yaw rotation using omnidirectional wheels on the top surface. With its modular structure, the conveyor layout can be designed and changed in a short time to reach a high level of flexibility with decentralized route planning [6, 7].

Another product is autonomous mobile robots. The mobile robot is one of the popular industrial robotic solutions due to its easy installation and use. The robot shown on the right side in Fig. 1.1 is an LD-series mobile robot with a roller conveyor top module from OMRON [8]. The advantages of mobile robots are easy integration into production lines with few or no factory layout modifications, flexible path planning, and high payload.

Even though the aforementioned systems and commercial products are applicable for several manufacturing systems, it is difficult to use in some applications such as clean room manufacturing, which controls the amount of small particles. Since the aforementioned products are a contact-type transfer line system, the particles can arise from the wearing between the object and actuator or inside the actuator mechanism.



Figure 1.1: Examples of products for flexible manufacturing.
(left) Cellular conveyor, Celluveyor, by cellumation GmbH [5].
(right) Autonomous mobile robot, LD series, by OMRON [8].

Nowadays, magnetic levitation (maglev) technology is applicable in various fields. This technology can untethered levitate a magnetized object by manipulating the outputs of the actuator to provide an attractive or repulsive force on the levitating object. Hence, maglev has the advantages of low friction and contactless motion. High-speed transportation, such as maglev trains [9] and hyperloop [10], is one of the well-known maglev applications. For example, an L0-series maglev train by JR Central in Japan could have a speed of over 500 km/h in 2015 [11].

For robotics, magnetics technology can be applied in several applications as reviewed in [12]. It can be used for delicate operations such as micromanipulators [13–15], microrobots [16–19], and medical tools [20], haptics [21–23], and bilateral teleoperation [24]. Meanwhile, it can also be utilized for industrial applications. For example, magnetic bearing [25] for high speed electrical machines, metal melting [26], clutch [27, 28], metal 3-D printing or additive manufacturing [29], and sensor using eddy-current effect [30].

Another industrial application of maglev systems is for manufacturing systems. Since the suspended object can be controlled for multiple degree-of-freedom (DOF) motions, the maglev system is a promising technology to improve the flexibility of the machining or material handling tasks in the production line. For these tasks, the repulsive-type planar maglev system, which has the mover levitated on top of the stator, is more suitable than the attractive-type system because it enables the system to work with other automation systems such as CNC machines and industrial robots.

Another application of the maglev is for positioning system which uses the combination of electromagnets and permanent magnets. With the advantages of the maglev system in non-contact motion between an object and maglev actuators, the system flexibility can be increased from planar motion to the form of 3D motion with precision motion [31]. In addition, the system can be used in the dust-control area due to frictionless transportation from micro-scale factory [32] to large-scale factory [33–36].

Since smart manufacturing is now required to be more intelligent and flexible to support mass customization, maglev technology has great potential to increase the flexibility of material handling tasks in modern manufacturing. With two aforementioned promising industrial applications of maglev which are planar motors and precision stages, the planar maglev system can perform as a conveyor and positioning stage in production lines.

However, two challenges in the development of maglev-based omnidirectional conveyors in modern smart manufacturing systems must be addressed. First, the design of the planar maglev system must be suitable for modern manufacturing. Next, the cross-coupling effect in levitation due to the magnetic field interaction can cause force and torque in other degrees of freedom.

1.2 Research Objectives

Magnetic levitation technology has advantages in contactless, dustless, and low-friction motion. Hence, a high-flexibility conveyor system using magnetic levitation technology is a potential solution to the problems of traditional conveyor systems.

The main goal of this research is to design a novel modular planar magnetic levitation system and implement it for omnidirectional conveying applications. To achieve this goal, the following research objectives must be fulfilled:

1. To design a modular planar magnetic levitation system for achieving high levitation performance
    - Develop the magnetic levitation model of magnetic force and torque between electromagnets and disc magnets
    - Design and analyze the modular planar electromagnet stator using an array of square coils
    - Design and analyze the permanent magnet movers to achieve multi-degree-of-freedom motion
    - Design the Magnetic Levitation Floor, the modular planar magnetic levitation system in RoboHub, Engineering 7, University of Waterloo
2. To develop maglev prototypes for omnidirectional conveyor system
    - 10-Coil Testbed
    - Magnetic Levitation Floor Prototype (Proto-MagFloor)
3. To implement and evaluate the modular planar maglev system for omnidirectional conveying application
    - Develop the levitation model and implement for wrench–current decoupling with lookup table method
    - Implement multi-degree-of-freedom linear interpolation to enhance the wrench–current decoupling performance
    - Develop the strategy for wrench–current decoupling using small-range lookup data for long-range motion
    - Test and evaluate the developed control strategies on the maglev systems

1.3 Research Contributions

In this thesis, a novel planar magnetic levitation system is developed. The levitation performance of the system is evaluated through experiments. With research works and experiments presented in the thesis, the main contributions of this thesis are as follows:

C.1 Design and analysis of a novel modular planar maglev system

The first contribution of this work is the design and analysis of a novel modular planar magnetic levitation system, namely, Magnetic Levitation Floor (Maglev Floor or MagFloor). With a modular structure, this design enables the system to be expandable and customizable for the specific space. The system is designed by considering magnetic, mechanical, and electrical design aspects. To the best of my knowledge, this system is distinct from previous research works and commercial products.

C.2 Design and optimization of the multiple-disc magnet mover

After the electromagnet stator of the planar maglev platform has been designed, the second contribution is the design and optimization of a permanent magnet mover. The disc magnet is used in this research. With a single-disc magnet mover, only five degrees-of-freedom motion can be controlled except yaw rotation. The mover with a combination of multiple-disc magnets is designed to achieve six degrees-of-freedom motion. The specifications and the arrangement of disc magnets are determined by defining the levitation and payload capability.

C.3 Wrench–current decoupling enhancement using multivariate linear interpolation

The cross-coupling effect is a major control problem of the magnetic levitation system. The decoupling solution using a wrench–current decoupling matrix is used in this work. The wrench matrices for the mover with a specific range of motion are pre-calculated and stored in the lookup table. However, the levitation performance can deteriorate at some mover pose due to discrete lookup data. Therefore, multivariate linear interpolation is used to enhance the decoupling by estimating the data at no-data poses.

C.4 Wrench–current decoupling strategy for long-range planar motion with small lookup data

Since levitation control in this work relies on wrench–current decoupling using the lookup table approach, the levitation range is limited by the data range. To enable unlimited horizontal motion range for conveying applications, in this work, a strategy to extend the use of small lookup data for long-range planar motion is developed. The data is generated with a horizontal range of a quarter area of the square coil in the first quadrant 16-coil array. For other quadrants, the mover pose is transformed to lookup for data in the first quadrant and then transformed back to its original quadrant.

1.4 Thesis Outline

This thesis consists of eight chapters, and each chapter is outlined as follows:

- Chapter 1 introduces the motivation of this research. Then, objectives and scopes are given with research contributions.
- Chapter 2 provides a comprehensive review of previous related research works on the design, modeling, and control of planar maglev systems. The preliminary study on the planar maglev prototype, MagTable, is presented in this chapter.

The rest of this thesis is divided into two parts as highlighted in Fig. 1.2. **Part I** presents the design of the planar maglev systems and permanent magnet movers using disc magnets.

- Chapter 3 presents the Lorentz force-based magnetic levitation model for wrench, forces and torques, computation. The model is further used in the system design process. Then, the implementation of the wrench model for real-time wrench–current decoupling in the control system is described.
- Chapter 4 presents the design of the planar coil array stator. The process begins with the conceptual design, the design of a square coil, coil array arrangement, and modular support structure. Two planar maglev prototypes, 10-Coil Testbed and Maglev Floor Prototype (Proto-MagFloor) are designed and built for pilot testing. Next, the design of the Maglev Floor system is detailed.
- Chapter 5 presents an analysis and design of permanent magnet movers using disc magnets. Magnet movers range from a single-disc magnet mover with 5-DOF motion to a multiple-disc magnet mover with 6-DOF motion.

Part II presents the implementation of the designed modular planar maglev systems for omnidirectional conveying applications.

- Chapter 6 presents the 5-DOF levitation experiment results on the maglev prototype, 10-Coil Testbed, with a single-disc magnet mover. A 5-DOF linear interpolation is used to solve the existing problems of lookup table approach.
- The decoupling strategy for long-range planar motion is implemented on the maglev prototype, Proto-MagFloor system. The experiment results with a single-disc and a multiple-disc magnet mover are reported in Chapter 7.
- Finally, conclusions, discussions, and future works are presented in Chapter 8.

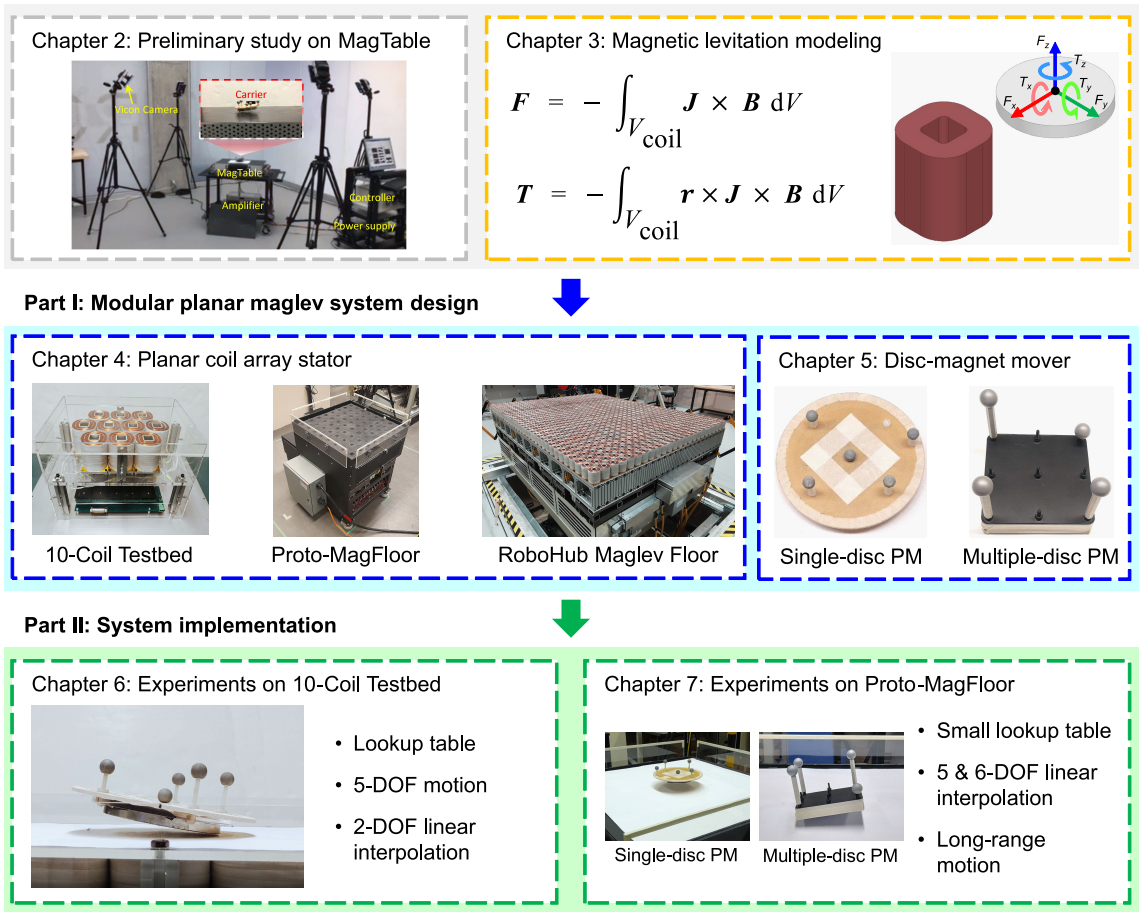


Figure 1.2: Graphical diagram highlighting the research progress.

Chapter 2

Background and Preliminary Study

This chapter provides a comprehensive review of previous related research works on the design, modeling, and control of planar maglev systems. Next, the preliminary study on the planar maglev prototype, MagTable, is presented in this chapter.

2.1 Magnetic Levitation Technology

Magnetic levitation or maglev is the phenomenon that an object is freely levitated in space without any support but only from the force when it experiences an external magnetic field. Typically, the magnetic force is produced to counter the effect of the gravitational force and move the object. The difference between suspension and levitation can be observed from the resultant force on the object which is the attractive or repulsive force, respectively.

Figure 2.1 represents ten types of maglev techniques. The first nine types were reported by Jayawant in [37]. Each technique uses different types of stators and levitating objects. However, most of the techniques are not practical for real-world applications. One of the existing application is a magnetic bearing that uses the concept of *vii*) electromagnet and ferromagnetic body with tuned RLC circuit.

The tenth technique, "*Lorentz Levitation*", was introduced in [38]. This technique uses the Lorentz force principle for levitation or suspension of the current-carrying conductor immersed in a magnetic field. The levitation force is directly proportional to the current. A bi-directional force can be provided by inverting the current. Most of the research works on planar maglev systems are based on this Lorentz Levitation technique.

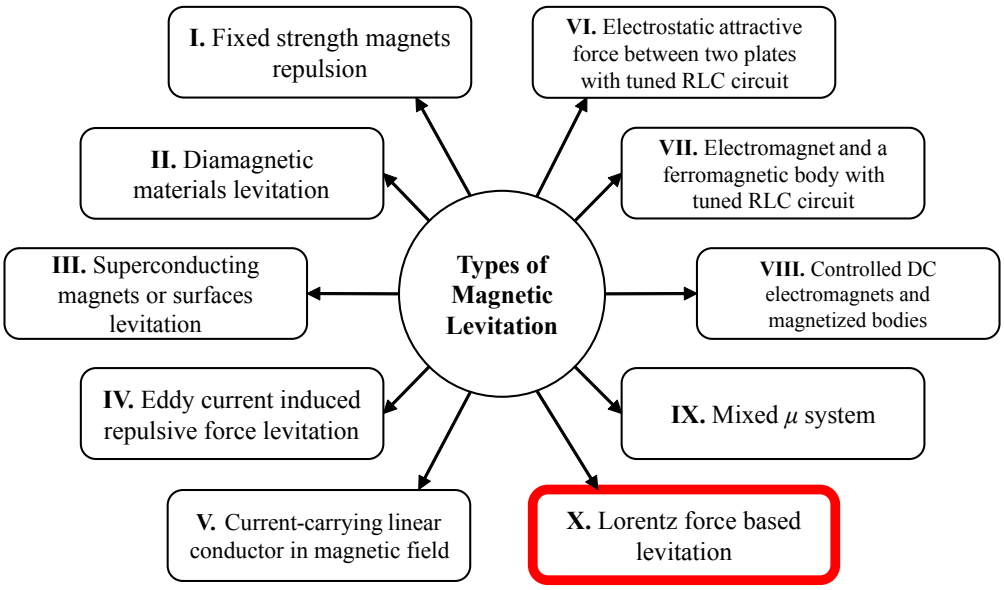


Figure 2.1: Types of magnetic levitation techniques [37, 38].

Regarding the force between the stator and mover, there are two types of magnetic levitation systems called attractive- and repulsive-type levitation. For material handling or conveying applications, repulsive-type levitation is more suitable for this application. The repulsive levitation system structure has the mover levitating above the stator. The system can be installed on the factory floor, which resembles the conveyor system.

However, several challenges of repulsive-type levitation must be addressed. First, the system control of the repulsive type is more complicated than the attractive type since it resembles the inverted pendulum problem. The challenge of this system lies in stabilizing the levitating object in the air. Meanwhile, the orientation of the object must be controlled which increases the difficulty in levitation control.

Moreover, the cross-coupling effect is another major problem of this system. The repulsive-type maglev systems usually have a number of coils more than the degrees of freedom of the levitating object. The system is a multiple-input-multiple-output (MIMO) system and has a strong coupling effect due to each coil providing forces and torques in all axes. Hence, the decoupling solution must be provided.

With the advantages and challenges of repulsive-type levitation, the rest of this chapter presents a review of previous research works on planar maglev systems including design, modeling, and proposed solutions to the aforementioned challenges.

2.2 Research on Magnetic Levitation Stages

This section presents a review of previous research on the magnetic levitation stages. Table 2.1 represents research works on maglev stages from several research groups by timeline. The photos of their systems are shown in Fig. 2.2.

In 1998, a high-precision magnetic levitation stage was developed by Kim and Trumper at MIT for photolithography [39] in semiconductor manufacturing. The stator has four horizontal windings arranged perpendicular to each other. The mover has four 1-D Halbach arrays at each corner as shown in Fig. 2.2a. The system is equipped with three laser interferometers for planar motions and three capacitance probes for vertical motions. The system can provide 6-DOF motion in a planar area of 50 mm $\times$ 50 mm, 400 μm height. The motion error is 5 nm rms in X and Y-axis, 10 nm rms in Z-axis.

Dr. Kim continued his research on the nano-positioning planar maglev stage at Texas A&M University. Figure 2.2d shows the system developed in [42, 59]. The system has a moving coil mover and a magnet array stator. The triangular mover has 3-phase windings to control 6-DOF motions. Three aerostatic bearings were used to support vertical force. The stator is a 2-D Halbach array consisting of magnets with conventional vertical and diagonal horizontal magnetization. The laser interferometers and proximity sensors were used to detect the motion in the horizontal range of 160 mm.

Figure 2.2e presents the Δ-stage developed in [43, 60]. The mover is a triangular aluminum plate mounted with three horizontal and three vertical cylindrical magnetic actuators. The actuator has a cylindrical magnet on the mover inserted in a cylindrical coil mounted on the stator as described in [61]. The mover motions are detected by capacitance sensors. The motion range is 300 μm in all translations and 3 mrad for rotations.

The next generation maglev stage was presented in [45]. The stage shown in Fig. 2.2g has a Y-shaped mover with a magnet at each end with its corresponding coil pair on the stator for horizontal and vertical motion control. The interferometers and capacitance probes were used to detect the horizontal and vertical motions respectively. Compared to the Δ-stage, the Y-stage provides a larger planar motion range of 5 mm with vertical motion of 500 μm, and small rotations of 0.1 deg due to sensor specifications.

The Ohio State University developed a 6-DOF maglev stage as presented in [40, 62]. The system depicted in Fig. 2.2b has a mover confined in the stator case. The mover has ten iron plates mounted on top and four sides. Ten electromagnets are installed in the stator surrounding the mover and paired with iron plates. The motion of the mover is detected by laser interferometers. Due to the design, the system has small motion ranges of 4 mm in planar motion, 2 mm in the vertical direction, and 1 degree of rotation.

Table 2.1: Review of previous research works on planar maglev stages.

Year	Stator	Mover	Sensor	Motion range
1998 [39] (2.2a)	Four horizontal windings	Four 1-D Halbach arrays	Laser interferometers, Capacitance probes	XY: 50 mm, Z: 400 µm 1 g acceleration
2002 [40] (2.2b)	3-D surround electromagnets	Floater with iron plates	Laser interferometers with retro-reflectors	XY: 4 mm, Z: 2 mm Rx,y,z: 1 deg
2004 [41] (2.2c)	2-D Halbach magnet array	Four horizontal coils	Inductive sensor	N/A
2004 [42] (2.2d)	2-D Halbach array	3-phase coils and aerostatic bearings	Laser interferometers Proximity sensors	XY: 160 mm
2005 [43] (2.2e)	Three horiz./vert. cylindrical coils	Triangular plate Δ with cyl. magnets	Laser interferometers Capacitance sensors	XYZ: 300 µm Rx,y,z: 3 mrad
2007 [44] (2.2f)	Cylindrical coil array	Rectangular and cylindrical magnets	LED & eddy current displacement sensors	XY: 1 mm, Z: 2 mm Rx,y,z: 0.1 deg
2007 [45] (2.2g)	Three pairs of coils	Y-shape frame with magnets	Laser interferometers Capacitance probes	XY: 5 mm, Z: 500 µm Rx,y,z: 0.1 deg
2008 [46] (2.2h)	Long rect. coils in herringbone	2-D Halbach array	Eddy current sensing probes	XY: 230 mm, Z: 1.5 mm Rx,y,z: 6 mrad
2008 [47] (2.2i)	Planar array of cylindrical coils	Single disc magnet	Optical motion tracking sensors	X,Y,Z: 30,90,12 mm Rx,y: 1 deg
2012 [48] (2.2j)	Multi-layer PCB conductors	Four 1-D Halbach array	Stereo-vision based position sensor	X: 260 mm, Y: 60 mm Z: 2.5 mm
2013 [49] (2.2k)	Planar array of cylindrical coils	Two disc magnets	Optical motion tracking sensors	XY: 80 mm, Z: 25 mm Rx,y,z: 80,30,unlimited
2014 [50] (2.2l)	Planar array of cylindrical coils	Ball shape with six disc magnets	Optical motion tracking sensors	Z: 4 mm, Rx,y: ±100 deg Rz: unlimited
2016 [51] (2.2m)	Three pairs of long coils	Three 1-D Halbach arrays	Capacitive sensors Optical sensors	XY: 100 mm, Z: 100 µm Rx,y,z: 0.5°,0.5°,200 µrad
2016 [52] (2.2n)	Vert. & Horiz. cylindrical coils	Platen with cylindrical magnets	Laser sensors Eddy gauges	XYZ: 2 mm Rx,y,z: 80,80,40 mrad
2017 [53] (2.2o)	Four coil arrays	Four 1-D Halbach arrays	Laser interferometers Capacitive sensors	XY: 30 mm, Z: 1 mm Rx,y,z: 6,6,10 mrad
2017 [54] (2.2p)	Circular PCB conductor	Circular Halbach array	Capacitive proves Optical encoders	Rz: unlimited
2019 [55] (2.2q)	Four pairs of long coils	Four 1-D Halbach arrays	Laser sensors and Eddy gauges	N/A
2019 [56] (2.2r)	3-phase coil arrays 1-phase coil arrays	1-D Halbach arrays Magnet pairs	Laser interferometers Capacitive sensors	XY: 2 mm, Z: 1 mm
2020 [57] (2.2s)	Coil PCB board	Four pairs of 1-D Halbach arrays	Optical inc. sensors Hall sensors	N/A
2020 [58] (2.2t)	Coils and magnets arranged in grid	Magnets and yokes arranged in grid	Interferometers Capacitance sensors	XY: 200 mm

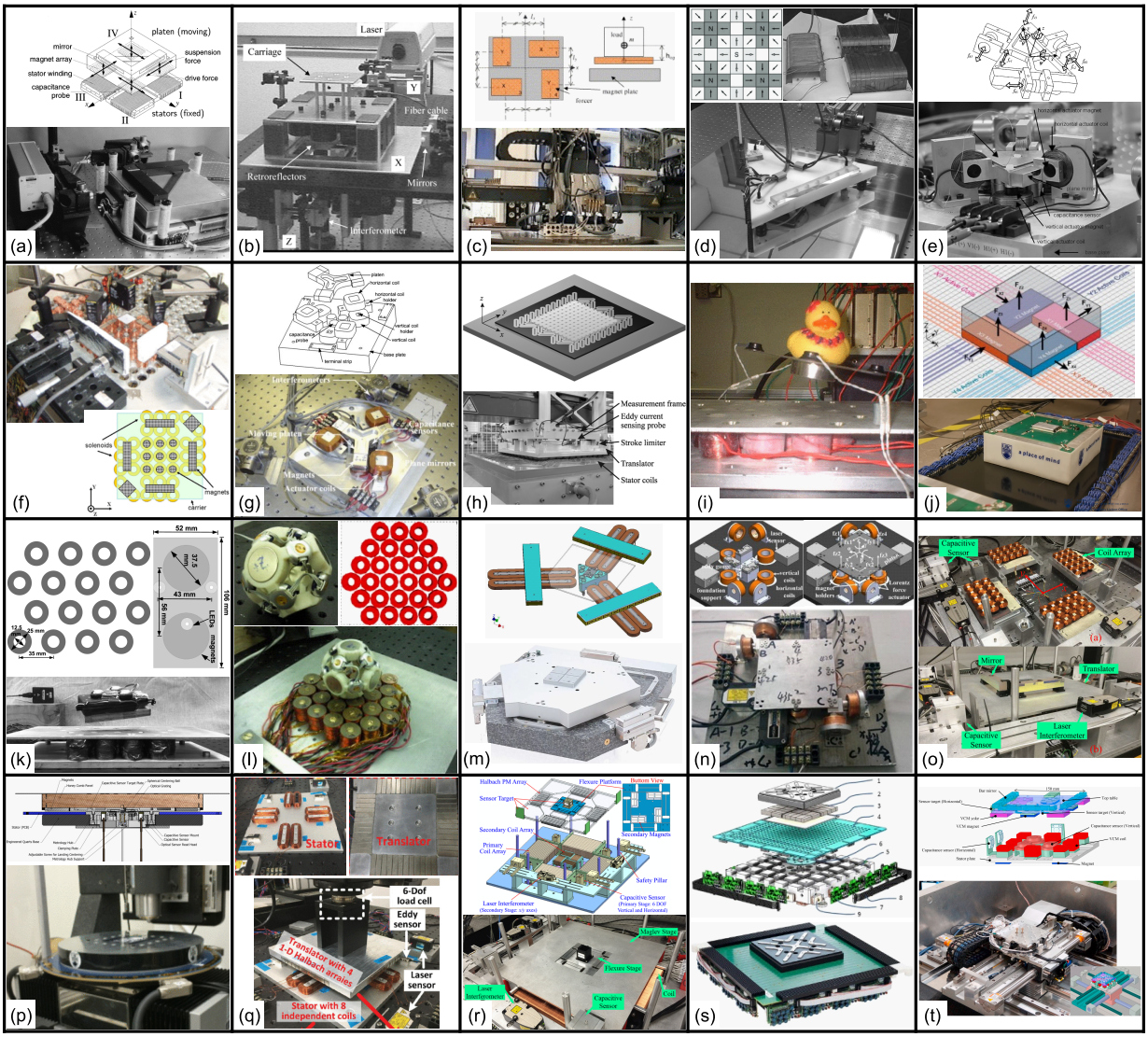


Figure 2.2: Planar maglev stages from previous works. **(a)** MIT maglev stage for Photolithography [39]. **(b)** Ohio State Univ. maglev stage [40]. **(c)** TU/e moving coil stage [41]. **(d)** Texus A&M Univ. moving-coil triangular stage [42]. **(e)** Texus A&M Univ. Δ-stage [43]. **(f)** National Taiwan Univ. mixed magnet stage [44]. **(g)** Texus A&M Univ. Y-stage [45]. **(h)** TU/e herringbone-pattern stage [46]. **(i)** UH Manoa single-disc mover [47]. **(j)** UBC PCB stage [48]. **(k)** UH Manoa two-disc mover [49]. **(l)** UH Manoa ball-shape mover [50]. **(m)** PiMag 6D [51]. **(n)** Wuhan Univ. cylindrical actuators [52]. **(o)** SIMTech-NUS four-array stage [53]. **(p)** UBC rotary table [54]. **(q)** Wuhan Univ. four-pair actuators [55]. **(r)** SIMTech-NUS Maglev-PAD [56]. **(s)** MAG-6D [57]. **(t)** Hitachi coarse-fine stage [58].

The National Taiwan University developed a maglev stage using a mixed-type magnet mover [44] in 2007. From Fig. 2.2f, the mover has an array of nine-disc magnets at the center, bar magnets on four sides, and two square magnets at two corners. The stator is an array of cylindrical coils. Four LED and two eddy current displacement sensors were used to detect the 6-DOF motion. For translation, the mover can move 0.4 mm on X-axis, 1 mm on Y-axis, and 2 mm on Z-axis. For rotation, the mover can rotate 0.1 degrees.

At the Eindhoven University of Technology (TU/e), an alternative 6-DOF maglev stage using a moving coil mover was proposed by Dr. Compter in [41]. As shown in Fig. 2.2c, the stator is a 2-D Halbach magnet array. The mover has four horizontal coils arranged perpendicular to each other. In the experiment, the prototype was built and mounted to a 3-D gantry with 3-D force sensors in between. Inductive sensors are used to detect planar motion. The concept of motion sensing using two Hall-effect sensor arrays was proposed.

The research on the planar maglev stage at TU/e continued by the Electromechanics and Power Electronics Group. Figure 2.2h presents their novel design with a planar array of rectangular coils arranged in a herringbone pattern [46, 63]. Their analysis indicates that the herringbone pattern has lower wrench ripples and ohmic loss than the typical straight coil array. In the experiment, a 2-D Halbach array mover was levitated at 1.5 mm above the stator and moved over the area of 230 $\times$ 230 mm. The mover motion was detected by eddy current sensing probes and encoders on the xy positioning system.

One promising research work on the maglev stage for the unlimited planar motion was developed by Dr. Lu at the University of British Columbia [48]. As shown in Fig. 2.2j, the stator has 16 layers of conductors on a PCB board. Each layer is perpendicular to other layers. The mover has four 1-D Halbach arrays. The forces and torques on the mover are controlled by activating corresponding coils under each magnet array. The experiment demonstrated the potential of the system for unlimited planar motion. Further studies presented in [64, 65] improved the levitation with force and torque ripple self-attenuation.

The UBC researchers also developed a 6-DOF magnetically levitated rotary table [54, 66] as shown in Fig. 2.2p. The mover has a circular Halbach array levitated above the circular conductor stator. Four capacitive sensors and optical encoders are installed at the center of the stator to measure the levitation gap and yaw rotation respectively. The mover can have unlimited yaw rotation. However, the motion ranges in other axes are limited by the sensor specifications. The system was applicable for precision micromachining.

German researchers developed a precision maglev stage PIMag 6D in [51]. Figure 2.2m illustrates their maglev system. The stator has three long coil pairs arranged in a Y shape with motion sensors at the center. The mover has three 1-D Halbach arrays mounted to the bottom of the mover frame in a triangular shape. The planar motions are measured by

optical sensors and grid plate on the mover. The vertical motion is measured by capacitive sensors. The experiments demonstrated long-stroke motions of 100 mm in both X and Y axes with 50 μm levitation gap and small errors in other axes.

Their further maglev stage design MAG-6D was presented in [57, 67]. Figure 2.2s presents the system structure. The stator has a PCB board with multiple planar coils on the top layer. The optical increment sensors and hall sensors are mounted under the coil board at the center of the stator for 6-DOF motion. An advantage of this stator design is the compact system with integrated motion sensors which is more practical than other previous designs. The mover has four pairs of 1-D Halbach arrays.

The research team at Wuhan University developed a maglev stage using multiple single-axis actuators [52]. The stage has four vertical actuators and two pairs of horizontal actuators as presented in Fig. 2.2n. Each actuator has a cylindrical coil mounted on the stator and a cylindrical magnet mounted on the mover. The horizontal and vertical motions are measured by the laser sensors and the eddy current gauges respectively. With this design, the 6-DOF motion ranges are small.

The next design of the planar maglev stage was presented in [55]. As shown in Fig. 2.2q, the mover has four 1-D Halbach arrays attached on four sides. The forces and torques on each magnet array are controlled by a pair of long rectangular coils. The laser sensors and the eddy current gauges were still used to measure the horizontal and vertical motions respectively. Since this work mainly focused on the development and validation of the force and torque model for real-time decoupling, the levitation experiment was not conducted.

A joint laboratory between the Singapore Institute of Manufacturing Technology and the National University of Singapore (SIMTech-NUS) developed a precision planar maglev stage in [53]. Their system stator has four sets of coil arrays as shown in Fig. 2.2o. Each coil array is used to drive the 1-D Halbach array on the mover. The horizontal and vertical motions are captured by laser interferometers and capacitive sensors respectively. The planar motion range is 30 mm at 1 mm levitation height with small rotations. The concept of unlimited planar motion and nanopositioning was proposed in [68, 69].

To improve the precision of the system, a magnetically levitated parallel actuated dual-stage (Maglev-PAD) was proposed in [56]. The system comprises primary and secondary stages as shown in Fig. 2.2r. The primary stage was studied and developed in [70, 71]. The stator has four three-phase coil arrays to support four 1-D Halbach arrays on the mover. The secondary stage was previously studied in [72] and developed to use four single-phase coil arrays and four magnet pairs at the center of the stage. The 6-DOF primary stage motions are measured by six capacitive sensors. The 2-DOF secondary stage motions are measured by two laser interferometers.

Hitachi Ltd. Research and Development Group developed a coarse-fine stage using a typical XY table and a maglev stage [58]. An overall system is shown in Fig. 2.2t. This research aimed to design a fine-motion maglev stage using a lightweight mover. The mover has yokes and magnets with a total mass of 0.81 kg. The stator has coils and capacitance sensors with magnets at the bottom for gravity compensation. It is mounted on the coarse-motion XY table. The total planar motion range is 200 mm measured by interferometers.

The research group from the University of Hawaii at Manoa developed a series of planar maglev stages using a planar array of cylindrical coils and disc magnets. In 2008, the maglev stage with a single disc magnet mover was developed. The forces and torques measurement data was used to develop a force-torque transformation [73]. Levitation experiments were conducted on the planar cylindrical coil array with 5 coils [47], 10 coils [74], and 16 coils [75] as shown in Fig. 2.2i. The mover equipped with IR markers can move with 5-DOF motions except for the yaw rotation.

Then, a mover with two disc magnets was developed in [49] to achieve 6-DOF motion. Figure 2.2k represents the design of the stator and mover in this work. The stator is an array of 16 cylindrical coils with offset for each row. The rectangular mover has two 37.5 mm-diameter disc magnets and is equipped with three LED markers. The system provided long-range motions in all directions. The planar motion range is 80 mm with a maximum levitation height of 25 mm. The rotation ranges are ± 40 degrees in roll, ± 15 degrees in pitch, and unlimited yaw. The use of low-cost motion sensors was further presented in [76].

Lastly, the magnetic levitation stage with unlimited omnidirectional rotation range was presented in [50, 77]. The stator is a compact planar array of 27 cylindrical coils. The mover has a unique design of a ball shape frame with six-disc magnets as shown in Fig. 2.2l. The levitation experiments demonstrated the large rotation ranges of ± 100 degrees in both roll and pitch and unlimited yaw rotation. The minimum air gap is 4 mm. However, the errors in positions and orientations were large.

Thus far, the literature has reviewed several maglev stages from several research groups. The stage designs with an electromagnet stator and a permanent magnet mover are mostly used. For stator design, the previous system stators can be categorized into two groups: i) multiple magnetically levitated actuators, and ii) planar coil array. Most systems were developed for the fine-motion stage with short or medium motion range. Some designs using the planar coil array have the potential for long-stroke motion by expanding the stator. For mover design, the Halbach array is very popular with its advantage of focusing a strong magnetic field on one side. However, most movers have heavy weight which results in a low levitation gap. Alternatively, the disc magnet mover can provide large motion ranges, but the motion errors must be improved.

Commercial Planar Maglev Stage Products

With decades of research works on planar maglev systems, commercial planar maglev stage products are now available in the market for factory automation. Figure 2.3 presents three planar maglev stage products with details as follows.

First, Planar Motor Inc. (PMI) introduced the Planar Motor system [33]. The system has a mover (XBot) and a modular stator (Flyway) as shown in Fig. 2.3a. Refer to their patent [78], the stator is an integrated module consisting of coils, sensors, amplifiers, and a controller. The magnet mover comprises four magnet arrays. Each array has multiple rectangular magnets with a plurality of magnetization. PMI partnered with B&R Industrial Automation GmbH in 2021 to develop a planar motor product, ACOPOS 6D [36].

The next product is XPlanar by Beckhoff Automation GmbH & Co. KG [34] as shown in Fig. 2.3b. Their system design presented in [79] has a modular stator array of conductor strips with integrated sensor modules and electrical drive units. This patent provides a sensor module improvement. The magnetic field sensors are arranged in two sets of sensor grid arrays with offsets in X and Y directions. The magnet mover also has four magnet units. However, each magnet unit is a 1-D Halbach array.

The most recent planar maglev stage product available in late 2022 is ctrlX FLOW^{6D} by Bosch Rexroth AG [35] as shown in Fig. 2.3c. This planar system was introduced as a part of their ctrlX AUTOMATION solution. Unlike other commercial products, this system uses permanent magnets for both the mover and the stator. The permanent magnet mover has a rounded shape. A strong magnetic field is generated and controlled by changing the angular position of the tile magnets in the stator.

The system specification comparison between these three commercial products is shown in Table 2.2. Overall, the stator is a tile-like square module structure with a comparable size. Various mover sizes are available with different payloads. For levitation capability, all products have an unlimited horizontal range of motion and yaw rotation. However, levitation height is small except ctrl FLOW^{6D} which can levitate up to 20 mm. The mover can move at high speed with a small levitation gap.



(a) (b) (c)

Figure 2.3: Commercial planar maglev stage products. **(a)** Planar Motor by Planar Motor Inc. **(b)** XPlanar by Beckhoff Automation GmbH & Co. KG. **(c)** ctrlX FLOW^{6D} by Bosch Rexroth AG.

Table 2.2: Comparison of commercial planar maglev stage products.

Product specifications	**Planar Motor** Planar Motor Inc.	**XPlanar** Beckhoff Automation	**ctrlX FLOW^{6D}** Bosch Rexroth
Stator module size (W×L×H)	Multi-layer PCB 240 × 240 × 70 mm	Multi-layer PCB 240 × 240 × 67 mm	Permanent magnets 239 × 239 × 216 mm
Mover	Four 1-D Halbach arrays Square & Rect. shape 120 – 450 mm	Four 1-D Halbach arrays Square & Rect. shape 113 – 235 mm	Permanent magnet Round shape ⌀ 160 and 220 mm
Motion range	XY: Unlimited Z: 0.4 - 4 mm Tilt: 5 deg Yaw: Unlimited	XY: Unlimited Z: 5 mm Tilt: 5 deg Yaw: Unlimited	XY: Unlimited Z: 20 mm Tilt: 10 deg Yaw: Unlimited
Repeatability	< 5 µm	±50 µm	±5 µm
Max speed	3 m/s	2 m/s	3 m/s
Payload	0.6 – 14.4 kg	0.4 – 4.2 kg	3.0 – 6.0 kg

2.3 Coil Design and Fabrication

Coil Design

A coil is a winding of electrical conductor wire which can generate a magnetic field when energized. The direction and magnitude of the magnetic field can be varied by varying the direction and amount of the supplied current. The coil design usually aims to achieve effective use of electrical power to produce the magnetic field. Therefore, the relationship between electrical power and the magnetic field is important.

The Fabry factor G proposed by Fabry in [80] provides the coil design optimization solution based on the coil dimensions. This factor represents the relationship between an axial magnetic field and electrical power. The detail of this relationship for cylindrical coil was derived in [81]. Three main coil dimensions to be considered in the Fabry factor are coil inner radius r_i, outer radius r_o, and height H, expressed by:

$$G_{(\alpha,\beta)} = \frac{1}{5}\sqrt{\frac{2\pi\beta}{\alpha^2-1}}\,\ln\left(\frac{\alpha+\sqrt{\alpha^2+\beta^2}}{1+\sqrt{1+\beta^2}}\right). \tag{2.1}$$

where $\alpha = r_o/r_i$ and $\beta = (H/2)/r_i$. The Fabry factor plot is depicted in Fig. 2.4.

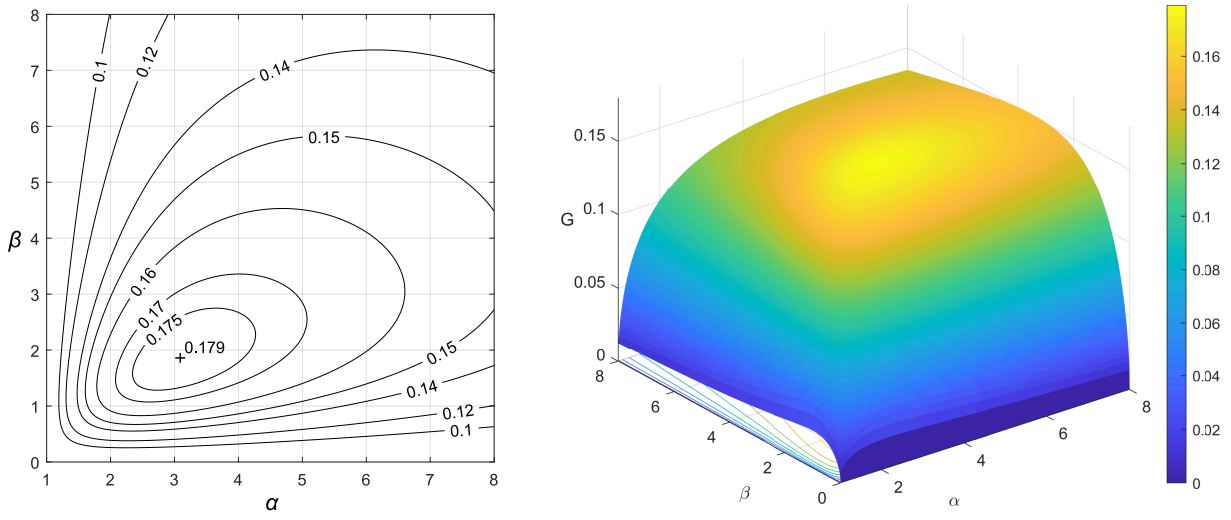


Figure 2.4: Fabry factor plot.

Coil Fabrication

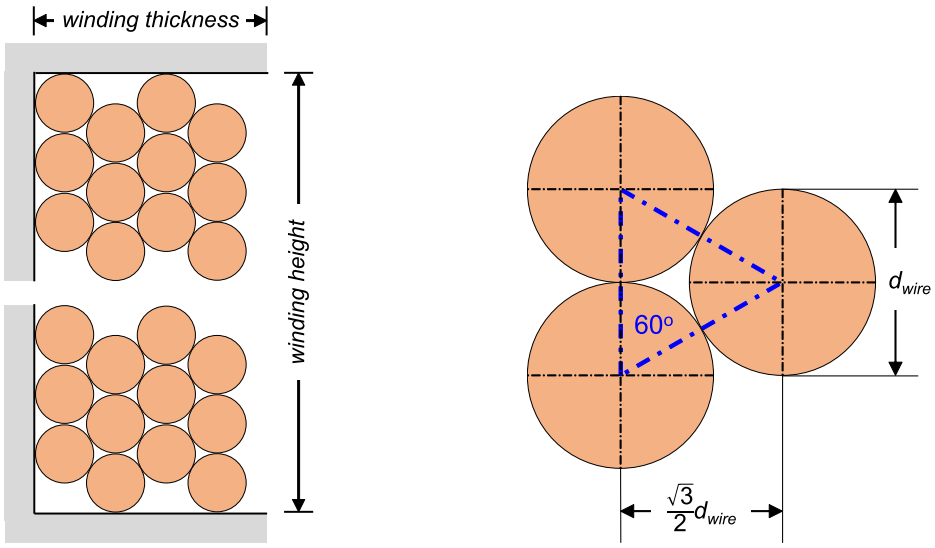
In coil winding fabrication, the orthocyclic winding as shown in Fig. 2.5a can ideally provide an optimal fill factor of 90.7% [82]. By placing the magnetic wire diameter d_{wire} into the grooves created by the previous layer, the winding space can occupy the most area as shown in Fig. 2.5b. The height and thickness of the winding can be calculated by:

$$\text{Winding height} = \text{vertical number of turns} \times d_{wire}. \tag{2.2}$$

$$\text{Winding thickness} = (1 + (n-1)\sin 60^\circ) \times d_{wire} \pm 10\%. \tag{2.3}$$

Considering the triangle in Fig. 2.5b, the fill factor of the orthocyclic winding can be calculated by:

$$\text{Fill factor} = \frac{\text{Winding area}}{\text{Triangle area}} = \frac{3 \cdot \frac{60}{360} \cdot \frac{\pi}{4} d_{wire}^2}{\frac{\sqrt{3}}{4} d_{wire}^2} = 0.907 \;\text{ or }\; 90.7\%. \tag{2.4}$$



(a) (b)

Figure 2.5: Orthocyclic winding with equal number of turns per layer.
(a) Winding pattern. **(b)** Fill factor.

2.4 Magnetic Levitation Modeling and Control

Lorentz Levitation Modeling

From the review of the planar maglev system design in the previous section, most of the proposed systems consist of electromagnet array stator and permanent magnet mover. The levitating forces and torques or wrench on the mover are based on the Lorentz force law.

Generally, the Lorentz force is computed from the cross-product between the current flown in the electromagnet length and the magnetic flux density originating from the permanent magnets in the mover. For a 1-D system, the Lorentz force on the current-carrying wire length $\boldsymbol{l}$ with current i placed in the external magnetic field $\boldsymbol{B}$ can be expressed by:

$$\boldsymbol{F} = i\ \boldsymbol{l} \times \boldsymbol{B}\ . \tag{2.5}$$

For Lorentz levitation in a 3-D system as shown in Fig. 2.6, the permanent magnet mover is levitated above an electromagnet array. The electromagnets with current density $\boldsymbol{J}$ are immersed in the magnetic field $\boldsymbol{B}$ from the permanent magnets. The 3-D Lorentz forces and torques can be computed by finding the results of the triple integral over the coil volume V_{coil}. Since the Lorentz force model results in a wrench on the electromagnet, the forces and torques on the mover are the reaction wrench of the calculation results as:

$$\boldsymbol{F} = -\int_{V_{coil}} \boldsymbol{J} \times \boldsymbol{B}\, \mathrm{d}V\ , \tag{2.6}$$

$$\boldsymbol{T} = -\int_{V_{coil}} \boldsymbol{r} \times (\boldsymbol{J} \times \boldsymbol{B})\, \mathrm{d}V\ . \tag{2.7}$$

Since the mover is freely suspended in the air without mechanical linkages or constraints, the mover can move in three dimensions with 3-D forces and torques. Therefore, the complication in the Lorentz force computation lies in two problems:

1. Magnetic flux density computation from the permanent magnet at any pose in three dimensions.

2. Finding the result of the cross product over the coil volume from volume integral.

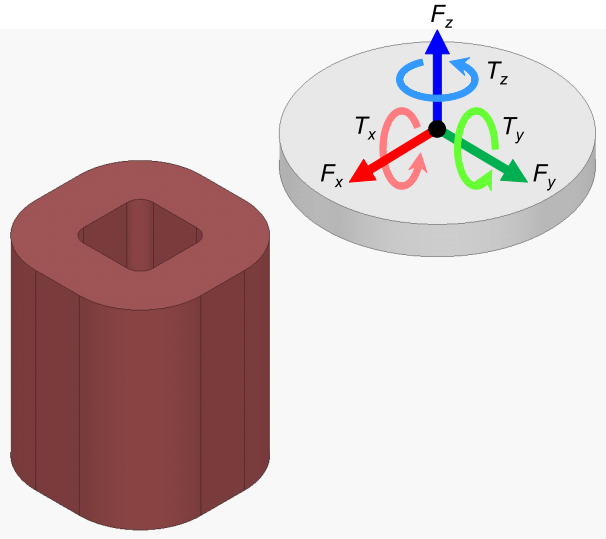


Figure 2.6: Single-coil single-magnet model with
the notation of 3-D wrench (forces and torques) on the magnet

Permanent Magnet Model

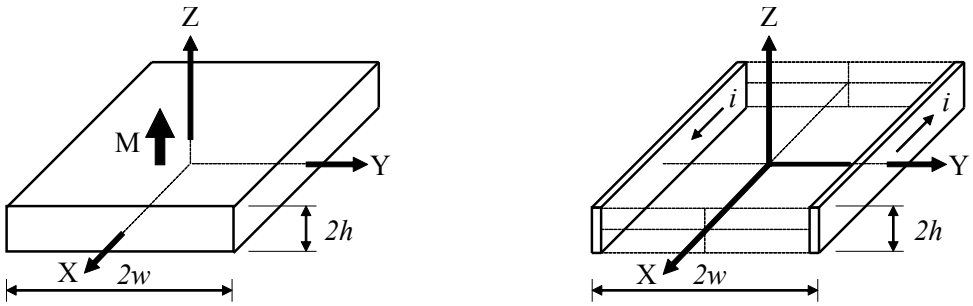
For the magnetic flux density computation, three permanent magnet models are presented in this section: the current model, the charge model, and the magnetic node model. The selected method is applied to model the disc magnet which is used in this thesis.

1.) Current model

For the Current model, the magnet is reduced to a distribution of equivalent current sheets [83]. Figure 2.7a illustrates a long-length rectangular bar magnet. The magnet has $2w$ width and $2h$ height with uniform magnetization M along Z-axis. For the current model, the magnet is considered to be two equivalent current sheets with current i flows in the opposite direction as illustrated in Fig. 2.7b.

The magnetization M is considered to be confined within the magnet volume V and becomes zero outside. The magnetic field calculation from the current model can be derived from:

$$\boldsymbol{B}_{(\boldsymbol{x})} = \frac{\mu_0}{4\pi} \int_V \boldsymbol{J}_{m(\boldsymbol{x}')} \frac{(\boldsymbol{x} - \boldsymbol{x}')}{|\boldsymbol{x} - \boldsymbol{x}'|^3} \mathrm{d}v' + \frac{\mu_0}{4\pi} \oint_S \boldsymbol{j}_{m(\boldsymbol{x}')} \frac{(\boldsymbol{x} - \boldsymbol{x}')}{|\boldsymbol{x} - \boldsymbol{x}'|^3} \mathrm{d}s' \tag{2.8}$$



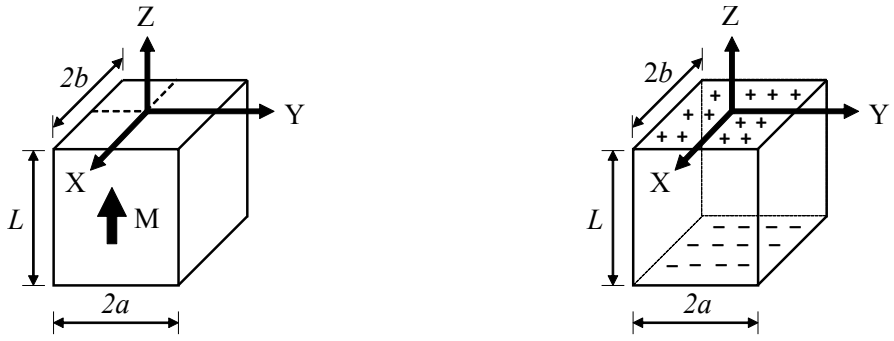
(a) Rectangular bar magnet (b) Equivalent current model

Figure 2.7: Rectangular bar magnet and equivalent current model

where $\boldsymbol{x}$ is observation point and $\boldsymbol{x}'$ is source point. $\boldsymbol{J}_m$ and $\boldsymbol{j}_m$ are volume and surface current densities. S is the magnet surface.

2.) Charge model

For the Charge model, the permanent magnet is modeled as the parallel charge surfaces. Figure 2.8a depicts a cubic magnet. The magnet has $2a$ width, $2b$ length, and L height with uniform magnetization M along Z-axis. The charge model of the magnet is modeled with two parallel charge surfaces as shown in Figure 2.8b.



(a) Cubic magnet (b) Equivalent charge model

Figure 2.8: Cubic magnet and equivalent charge model

Similar to the current model, the magnetization M is considered to be confined within the magnet volume V and becomes zero outside. The magnetic field calculation from the charge model can be found from:

$$\boldsymbol{B}_{(\boldsymbol{x})} = \frac{\mu_0}{4\pi} \int_V \frac{\rho_{m(\boldsymbol{x}')} \left(\boldsymbol{x} - \boldsymbol{x}'\right)}{\left|\boldsymbol{x} - \boldsymbol{x}'\right|^3} \mathrm{d}v' \; + \; \frac{\mu_0}{4\pi} \oint_S \frac{\sigma_{m(\boldsymbol{x}')} \left(\boldsymbol{x} - \boldsymbol{x}'\right)}{\left|\boldsymbol{x} - \boldsymbol{x}'\right|^3} \mathrm{d}s' \,. \tag{2.9}$$

where $\boldsymbol{x}$ is observation point and $\boldsymbol{x}'$ is source point. S is the magnet surface. The volume and surface current densities are $\boldsymbol{J}_m$ and $\boldsymbol{j}_m$. The model was used for the force computation between two parallel cuboidal magnets in [84] and the planar motor in [85].

3.) Magnetic node model

The magnetic nodes approach is the variation of the charge model from [86, 87] which was proposed by F. Bancel in 1999 [88]. The approach modeled the cubic permanent magnet by setting its eight corners with uniform magnetization nodes as illustrated in Figure 2.9. As a consequence of Maxwell's equation, this approach was based on two assumptions, which are i) no disturbance or contribution from other materials to the magnetic field of the analyzed objects. ii) the magnet is an ideal magnet with fixed and uniform magnetization. The magnetic field produced by each magnetic node k can be expressed as:

$$B_{xk} = \frac{\epsilon_k}{4\pi} \ln \left(- y_r + \sqrt{x_r^2 + y_r^2 + z_r^2} \; \right) , \tag{2.10a}$$

$$B_{yk} = \frac{\epsilon_k}{4\pi} \ln \left(- x_r + \sqrt{x_r^2 + y_r^2 + z_r^2} \; \right) , \tag{2.10b}$$

$$B_{zk} = \frac{\epsilon_k}{4\pi} \arctan \left(\frac{x_r y_r}{z_r \sqrt{x_r^2 + y_r^2 + z_r^2}} \right) , \tag{2.10c}$$

where x_r, y_r and z_r are equal to $x - x_k$, $y - y_k$, and $z - z_k$, respectively. ϵ_k is magnetization with a coefficient sign of each node. The magnetization can be inverted when switching the coefficient sign of the node. For example, if the magnet is flipped upside down, the magnet can be modeled by reversing the sign of the nodes. The 3-D forces and torques between two rectangular magnets in parallel can be found in [89].

This method can be applied to the complex shape. To model the complex-shaped permanent magnet, the following conditions must be satisfied. The node configuration on the magnet or electromagnet must be switched from one node to the adjacent node:

- by only shifting in parallel along X, Y, or Z-axis;
- by changing the sign of node magnetization.

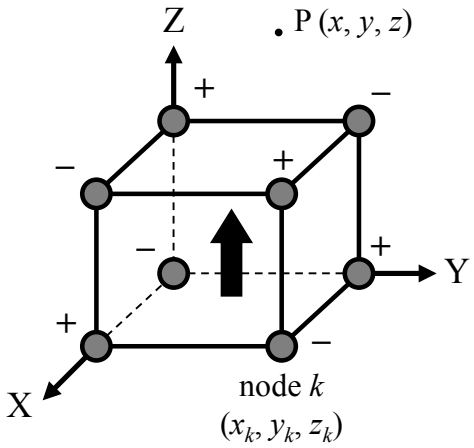


Figure 2.9: Magnetic node representation of cubic permanent magnet (F. Bancel, 1999) [88]

Among the three modeling methods, the magnetic nodes method has an advantage over the other methods. For the complex-shaped magnet, the magnetic nodes can be implemented for parallel computation which is feasible for real-time control [90]. In this work, the magnetic nodes approach is used for the magnetic field calculation.

Magnetic Levitation Control and Cross-Coupling Effect

The planar maglev system is an over-actuated system and each coil can induce 6-DOF wrench (forces and torques) on the mover as shown in Fig. 2.10. The interaction between the coil current and the wrench on the mover is called the cross-coupling effect. This effect can cause difficulty in levitation control to maintain the system stability.

Compare to a brushless DC motor (BLDC motor), the motor constant K_t represents the relationship between armature current i_a and output torque τ_m, expressed by:

$$\tau_m \;=\; K_t \, i_a \;, \tag{2.11}$$

Likewise, the current-to-wrench conversion in 3-D magnetic levitation can be expressed by:

$$\boldsymbol{w} \;=\; \mathbf{K} \, \boldsymbol{i} \;, \tag{2.12}$$

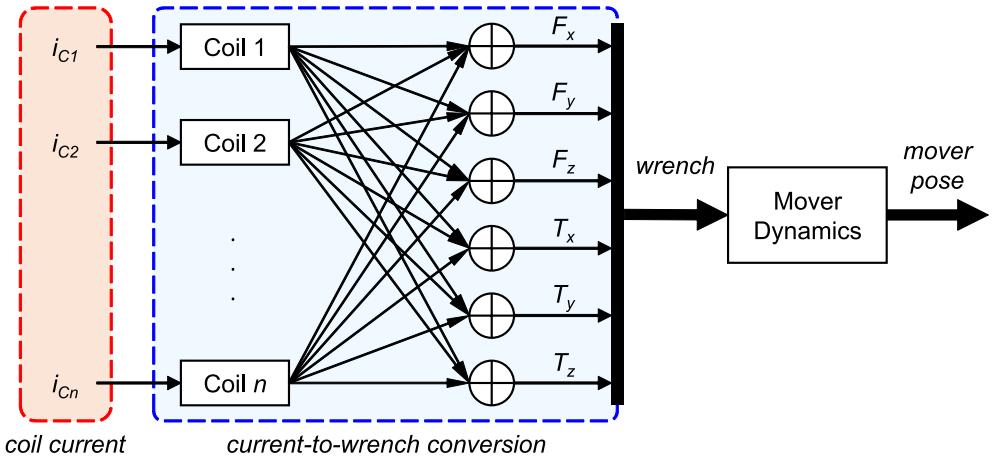


Figure 2.10: Planar maglev system plant diagram
with cross-coupling effect in current-to-wrench conversion.

$$\boldsymbol{w} = \begin{bmatrix} \boldsymbol{k}_{\text{coil}\,1} & \boldsymbol{k}_{\text{coil}\,2} & \dots & \boldsymbol{k}_{\text{coil}\,n} \end{bmatrix} \quad \boldsymbol{i}\,, \tag{2.13}$$

$$\begin{bmatrix} F_x \\ F_y \\ F_z \\ T_x \\ T_y \\ T_z \end{bmatrix} = \begin{bmatrix} f_{x1} & f_{x2} & \dots & f_{xn} \\ f_{y1} & f_{y2} & \dots & f_{yn} \\ f_{z1} & f_{z2} & \dots & f_{zn} \\ \tau_{x1} & \tau_{x2} & \dots & \tau_{xn} \\ \tau_{y1} & \tau_{y2} & \dots & \tau_{yn} \\ \tau_{z1} & \tau_{z2} & \dots & \tau_{zn} \end{bmatrix} \begin{bmatrix} i_{\text{coil}\,1} \\ i_{\text{coil}\,2} \\ \vdots \\ i_{\text{coil}\,n} \end{bmatrix}, \tag{2.14}$$

where $\boldsymbol{w}$ is a wrench vector of 3-D forces and torques on the mover which is induced from n coils with supplied current $\boldsymbol{i}$. $\mathbf{K}$ is a wrench matrix which represents the current-to-wrench conversion. The component $\boldsymbol{k}$ in each column of this matrix represents the ratio of current input from a single coil i_{coil} to each wrench output (f, τ) on the mover. Since the change of a single coil current causes wrenches to exert all degrees of freedom, the maglev system is a multiple-input multiple-output (MIMO) system and causes difficulty in levitation control.

One solution to the cross-coupling effect is using a wrench–current decoupling matrix. This decoupling matrix is the inverse of the wrench matrix $\mathbf{K}$, denoted by $\mathbf{K}^{+}$. Figure 2.11a depicts an implementation of the decoupling matrix to decouple the cross-coupling effect in the feedback control of the planar maglev system. Assume that the current amplifiers can ideally supply coil current equal to the current command the equation from the wrench command $\boldsymbol{w}_{\text{command}}$ to the actual wrench $\boldsymbol{w}_{\text{actual}}$ can be written by:

$$\boldsymbol{w}_{\text{actual}} \;=\; \mathbf{K}\;\boldsymbol{i}_{\text{coil}}\;, \tag{2.15}$$

$$\boldsymbol{w}_{\text{actual}} \;=\; \mathbf{K}\;(\mathbf{K}^{+}\;\boldsymbol{w}_{\text{command}})\;, \tag{2.16}$$

where the decoupling matrix $\mathbf{K}^{+}$ is a right inverse of $\mathbf{K}$ to fulfill $\mathbf{K}\,\mathbf{K}^{+} = \mathbf{I}$ which yields the actual wrench to be equal to the wrench command, $\boldsymbol{w}_{\text{actual}} = \boldsymbol{w}_{\text{command}}$. As a result, the MIMO maglev system is decoupled into multiple Single-Input Single-Output (SISO) systems as represented by an equivalent decoupled system diagram in Fig. 2.11b.

For the wrench matrix $\mathbf{K}$, the number of rows represents the number of degrees of freedom of the magnet mover. The number of columns represents the number of active coils. The number of coils is usually more than the number of degrees of freedom of the mover. Therefore, the wrench matrix is non-square and becomes non-invertible.

To find the decoupling matrix $\mathbf{K}^{+}$, the inverse of the wrench matrix can be solved by using the Moore-Penrose pseudoinverse. For the right inverse, the decoupling matrix $\mathbf{K}^{+}$ can be computed from the wrench matrix $\mathbf{K}$ and its transpose $\mathbf{K}^{\mathsf{T}}$ by:

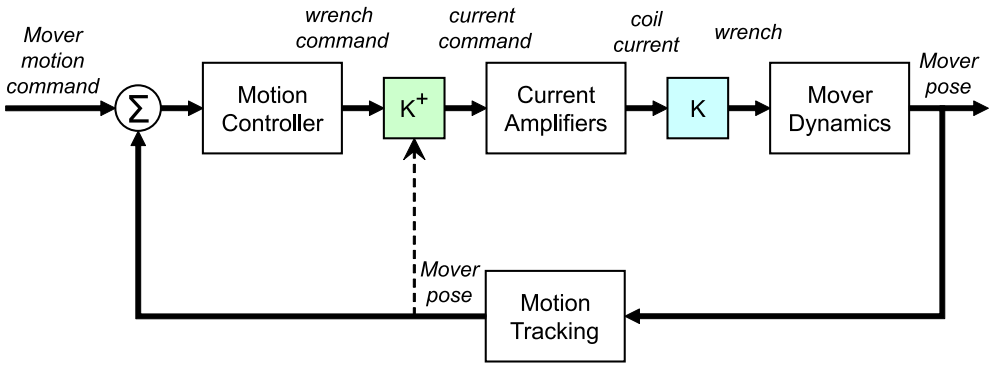
$$\mathbf{K}^{+} = \mathbf{K}^{\mathsf{T}}(\mathbf{K}\,\mathbf{K}^{\mathsf{T}})^{-1}\,. \tag{2.17}$$

Next, the levitation controllability is another issue since the mover moves across the area with various poses which can result in different controllability. In [50], the system controllability was evaluated by the condition number of the wrench matrix. The condition number represents the sensitivity of the system to the input changes or errors by:

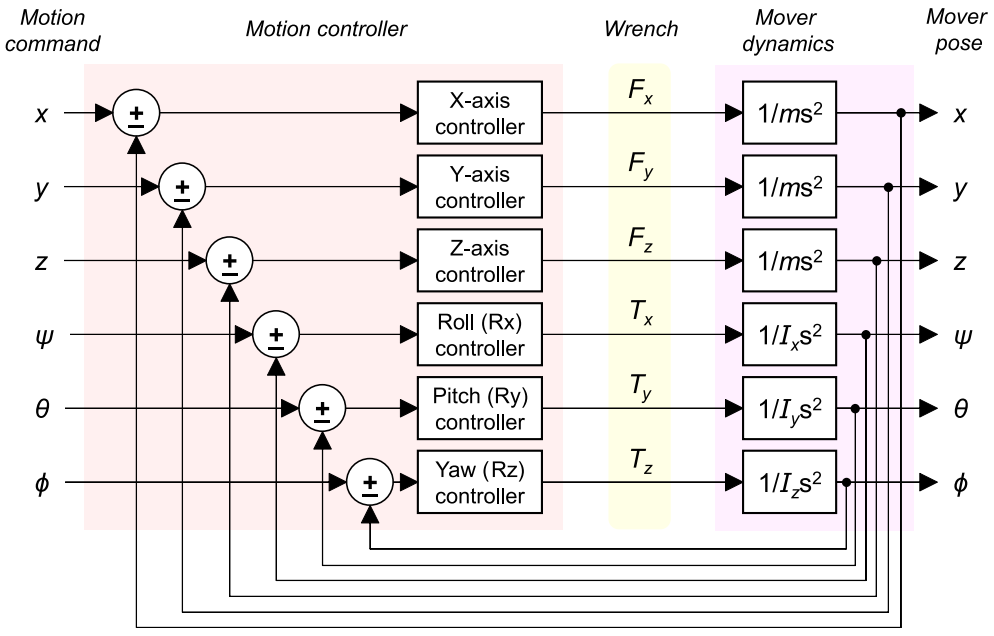
$$\text{cond}(\mathbf{K}) \;=\; \frac{\sigma_{\max}(\mathbf{K})}{\sigma_{\min}(\mathbf{K})}\;. \tag{2.18}$$

where $\sigma_{\max}(\mathbf{K})$ and $\sigma_{\min}(\mathbf{K})$ are maximal and minimal singular values of the wrench matrix. The lower condition number is well-conditioned or has better controllability. The high condition number is ill-conditioned and difficult to control. In other words, the system is sensitive to the small coil current changes or errors that can cause a large wrench output.

This section described the problem of the cross-coupling effect in the current-to-wrench conversion, which causes difficulty in magnetic levitation control. The solution to this problem using the decoupling matrix $\mathbf{K}^{+}$ is widely used by several research groups. The details of wrench computation for the $\mathbf{K}$ and $\mathbf{K}^{+}$ matrices are presented in Chapter 3. The condition number of the wrench matrix can be used to evaluate the controllability of the system. It is used in the analysis and design of the disc-magnet movers in Chapter 5.



(a)



(b)

Figure 2.11: Feedback control diagram for a planar maglev system with a decoupling matrix $\mathbf{K}^+$. **(a)** Decoupling matrix $\mathbf{K}^+$ implementation. **(b)** Equivalent decoupled system.

2.5 Preliminary Study: MagTable[1]

System Overview

At the University of Waterloo, Magnetic Levitation Table or MagTable is the very first planar maglev prototype developed at the Maglev Microrobotics Laboratory. This section presents an overview and the research works conducted on this system.

MagTable is a repulsive-type planar maglev system. The stator comprises an array of electromagnets and amplifiers. The permanent magnet movers used in this research are single-disc magnet and three-disc magnet movers. The motion or pose of the mover is captured by motion tracking cameras. Figure 2.12 represents an overview of the MagTable system in RoboHub, University of Waterloo.

Electromagnet Stator

The MagTable stator has an array of 70 square coils as shown in Fig. 2.13. The stator design process begins with the coil design. Compare to the round coil, the square coil is preferable because it provides an improvement of packing density of the magnetic field.

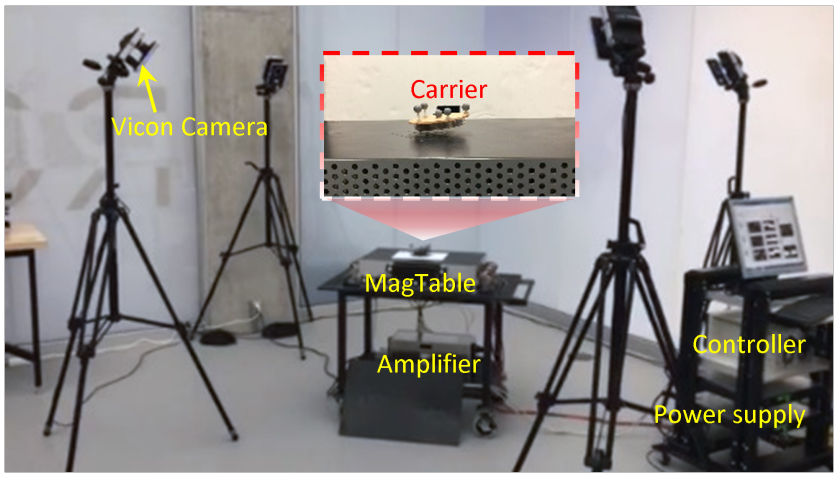


Figure 2.12: MagTable system overview.

[1]The MagTable was a collaborative work with Dr. Xiaodong Zhang and Dr. Heng Zhang, Maglev Microrobotics Laboratory, University of Waterloo. The work in this section was published in [91].



Figure 2.13: MagTable: Electromagnet array stator.

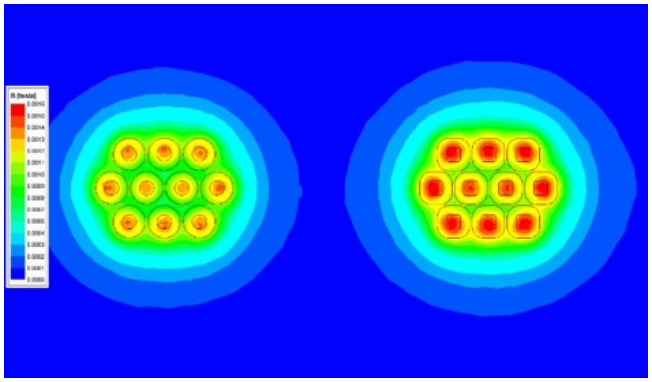


Figure 2.14: Magnetic field comparison between round **(left)** and square **(right)** coil array at 20 mm above the array.

A comparison between round and square coil array was conducted in the finite element analysis software, ANSYS Maxwell. Both array comprises 10 air-core coils which are arranged in a zigzag pattern. Both round and square coils have the same width and height. Each coil is supplied with 1 A DC current in the same direction.

The magnetic field plot at 20 mm above both arrays demonstrates a higher magnetic field density of the square coil array as shown in Fig. 2.14. By comparing the magnitude of the magnetic field in the horizontal range of 100 mm $\times$ 100 mm at the center of the array, the square coil array has an average magnetic field improvement of 18 percent.

Next, the dimensions of the square coil are design and optimized. Three main dimensions to be designed are outer width, inner width, and height. The Fabry factor and vertical force between one coil and one magnet are used. The designed coil specifications are detailed in Table 2.3. This design procedure was used to design the coil in this thesis.

Table 2.3: MagTable: Coil parameters

Parameters	Value	Unit
Outer coil width	50.00	mm
Inner coil width	22.10	mm
Height	55.60	mm
Wire gauge	18	AWG
Number of radial layer	12	layers
Total number of turns	540	layers
Resistance	1.5	Ohms
Inductance	4.8	mH

After designing the square coil, 70 coils are arranged in the stator frame with offsets for each row or zigzag pattern. This pattern provides a high packing density of the array. The coil pitch in the x direction is 54 mm and the coil pitch in the y direction is 52 mm.

Permanent Magnet Mover

Figure 2.15 represents three magnet movers used in this work: 1) single 2-inch magnet mover which has a comparable diameter with coil width, 2) single 3-inch magnet mover, and 3) three 2-inch magnet mover. Each mover equips reflective markers for motion tracking. One highlight in this research is the design of the mover with three 2-inch magnets.

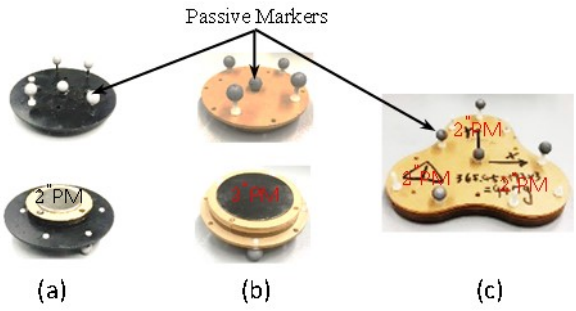
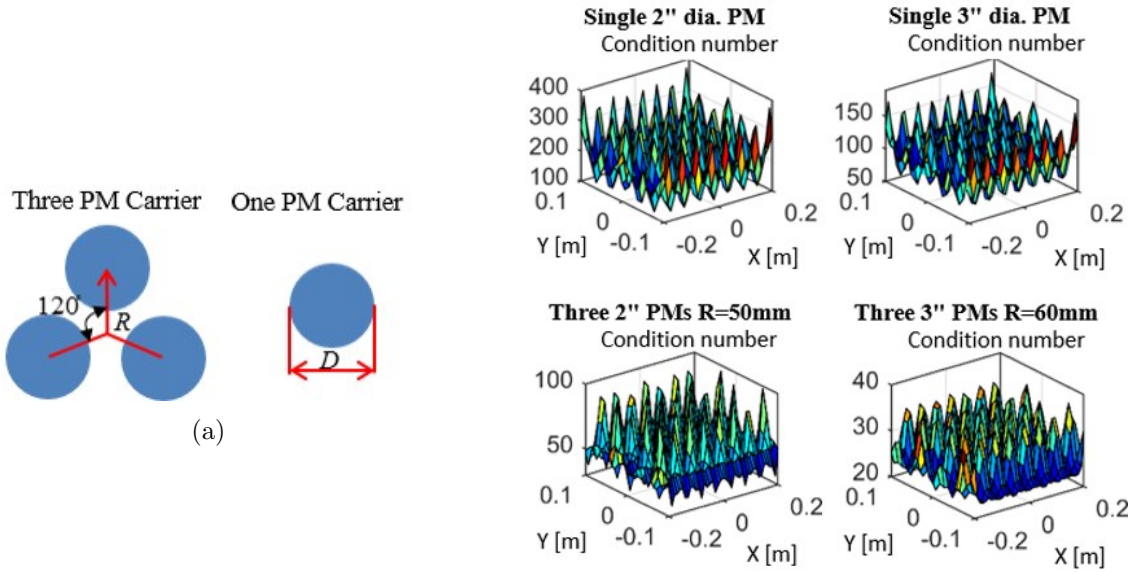


Figure 2.15: MagTable: Movers tested in the experiment.
(a) 2-inch magnet. **(b)** 3-inch magnet. **(c)** Three 2-inch magnets.



(a)

(b)

Figure 2.16: Three-disc magnet mover design: Condition number.
(a) Magnet layout. **(b)** Condition number plot.

The single-disc magnet mover can only achieve 5-DOF motion without yaw rotation due to its symmetrical shape. To achieve 6-DOF motion, a three-disc magnet mover was designed with layout optimization or optimal distance from the center of the mover to the center of the magnet R. To determine the optimal R, the condition number, max current, and energy consumption are computed from the wrench matrix with varied R over a specific area and plotted in Figures 2.16 and 2.17. A comparison between three movers is shown in Fig. 2.18. The mass properties for all mover is detailed in Table 2.4.

Table 2.4: Mass properties of three movers.

Movers	Mass (kg)	I_x (kg·m^2)	I_y (kg·m^2)	I_z (kg·m^2)
Single 2-inch PM	0.374	0.000052	0.000052	0.000096
Single 3-inch PM	0.534	0.00021	0.00021	0.00040
Three 2-inch PMs	0.945	0.00182	0.00179	0.00357

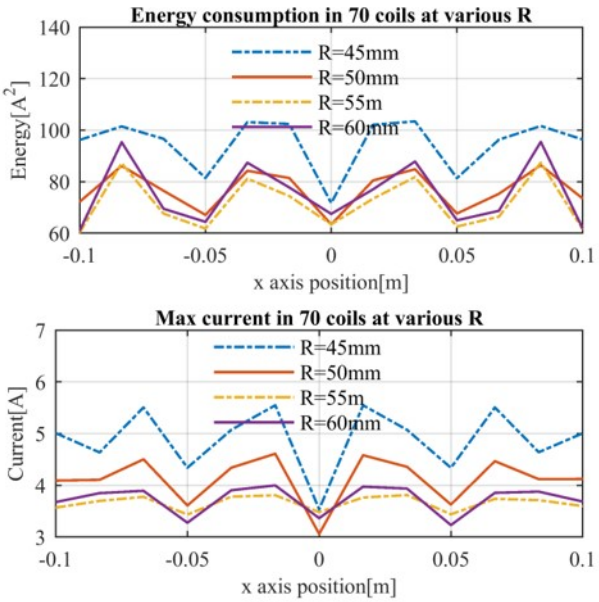


Figure 2.17: Three-disc magnet mover design: Total energy consumption and maximum current in 70 coils with various R at different levitation locations.

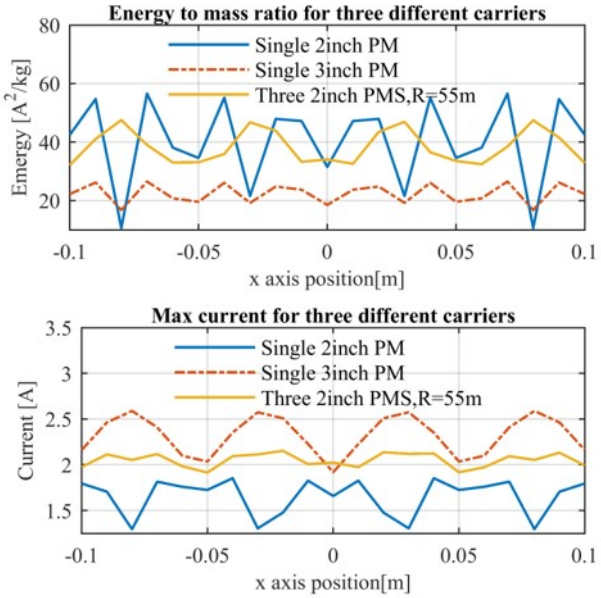


Figure 2.18: Comparison of performance among three movers: Single 2-inch magnet, Single 3-inch magnet, and Three 2-inch magnets.

System Hardware and Control

The hardware connection diagram of the MagTable system is presented in Fig. 2.19. The coil stator is installed on a portable four-wheel cart and covered by a thin aluminium sheet. Cooling fans and fins are assembled at the bottom of the coil array for heat dissipation.

Motion capture cameras were used to capture the mover pose in real time with a frame rate of 1 kHz. Position feedback using cameras has advantages over using conventional laser sensors or Hall sensors. For example, setting up cameras is simple and easily expandable by adding extra cameras for large levitation area. The captured data is sent to computer for image processing. Then, the mover pose information is transmitted to the controller.

The system controller is an industrial programmable logic controller (PLC) with a control frequency of 1 kHz. The coil current commands are computed in the PLC and then sent signals to 70 amplifiers. The amplifier has internal current control. The maximum continuous current is 5 A. All amplifiers are supplied with 36 VDC from four DC power supply units.

Next, feedback control is needed for stabilizing a repulsive levitation. For the MagTable system, the cross-coupling effect in current–wrench conversion between coil currents and 6-DOF forces and torques on the mover must be addressed. This problem can be decoupled by the wrench–current decoupling matrix. As a result, six SISO PID controllers are enough for stabilizing the levitation in each degree of freedom. The controller block diagram is shown in Fig. 2.20. A gravity compensation $\boldsymbol{T}_0$ is added to the PID controller outputs to compensate the gravity force of the mover.

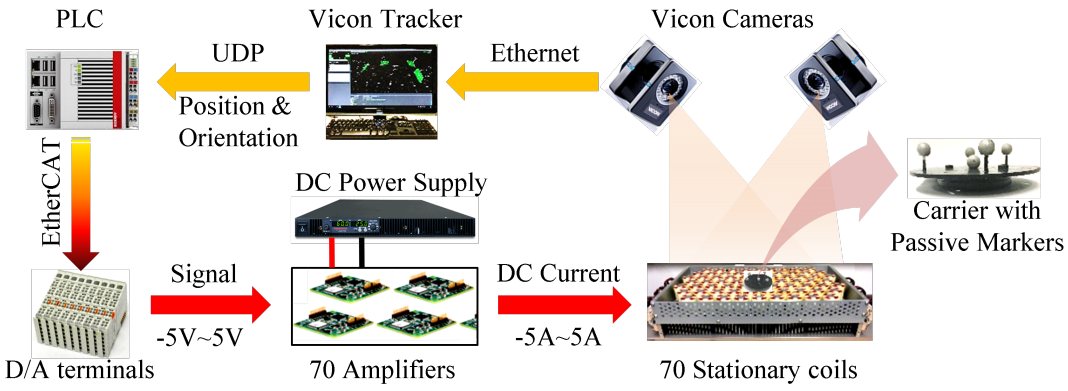


Figure 2.19: MagTable: Hardware connection diagram.

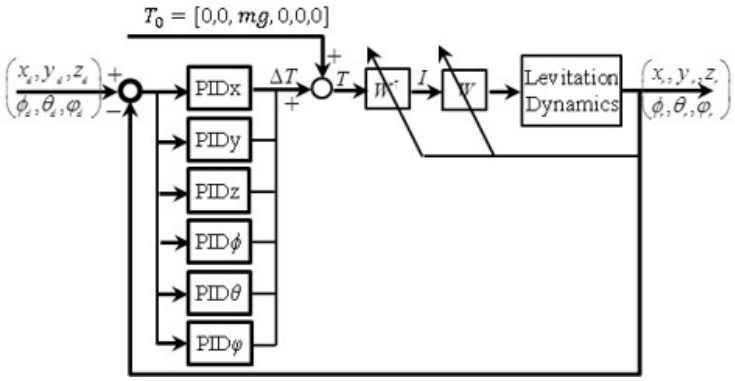


Figure 2.20: MagTable: 6-DOF motion control diagram.

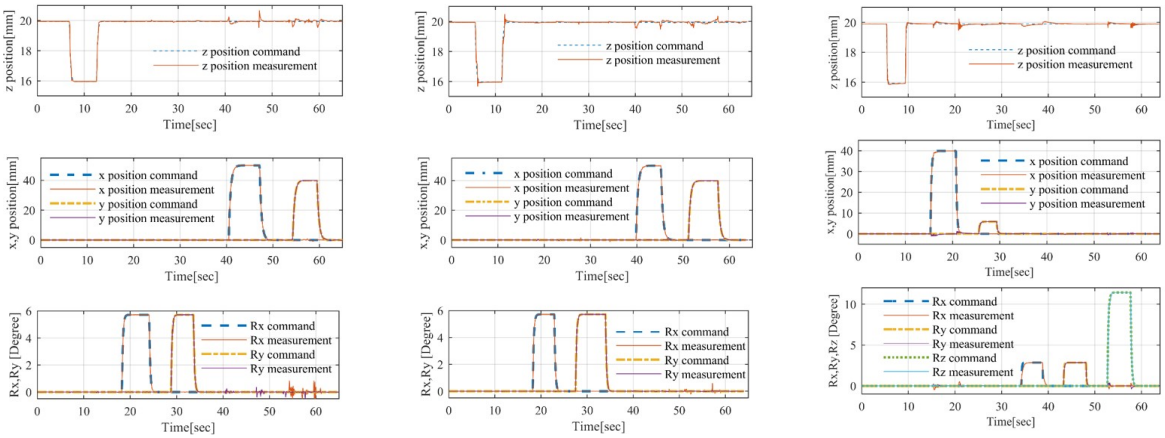
Levitation Experiments and Results

Figures 2.21a and 2.21b show the step responses of the single 2-inch and 3-inch disc magnet movers. Both movers were levitated at 20 mm above the coil array. For the single 2-inch magnet mover, the translation error is 30 μm. The rotation error is 0.027 degrees. For the single 3-inch magnet mover, the translation error is 20 μm. The rotation error is 0.016 degrees. However, the cross-coupling effect and undesired yaw rotation disturbed all 5-DOF motions, especially, in the X and Y directions.

In the third experiment, the mover with three 2-inch disc magnets was controlled to follow 6-DOF step motion commands. The results are presented in Fig. 2.21c. The maximum 3-D translation errors are less than 30 μm. The maximum rotation error is less than 0.01 degrees. Even though undesired yaw rotation was not observed, the cross-coupling effect still persisted and caused a large error in Z direction.

Next, fast motion tracking experiments were conducted with all three movers. Each mover was controlled to follow a fast-changing trajectory in the X direction from −50 mm to 50 mm. The results are presented in Fig. 2.22. The motion tracking in the X axis, Z axis, and the pitch rotation were also observed. The single 2-inch disc magnet mover started to lose stability when the speed was over 40 mm/s. The single 3-inch disc magnet mover started to lose stability at the speed of 20 mm/s. The three-disc magnet mover had better performance with less fluctuation.

Comparing with the single 3-inch disc magnet, it is evident that the single 2-inch disc magnet is less able to maintain a levitation stability when moving at high speed. The results also meet the conclusion from the condition number analysis that a smaller condition number provides better controllability.



(a) (b) (c)

Figure 2.21: MagTable experiment results: Step motion.
(a) Single 2-inch magnet. **(b)** Single 3-inch magnet. **(c)** Three 2-inch magnets.

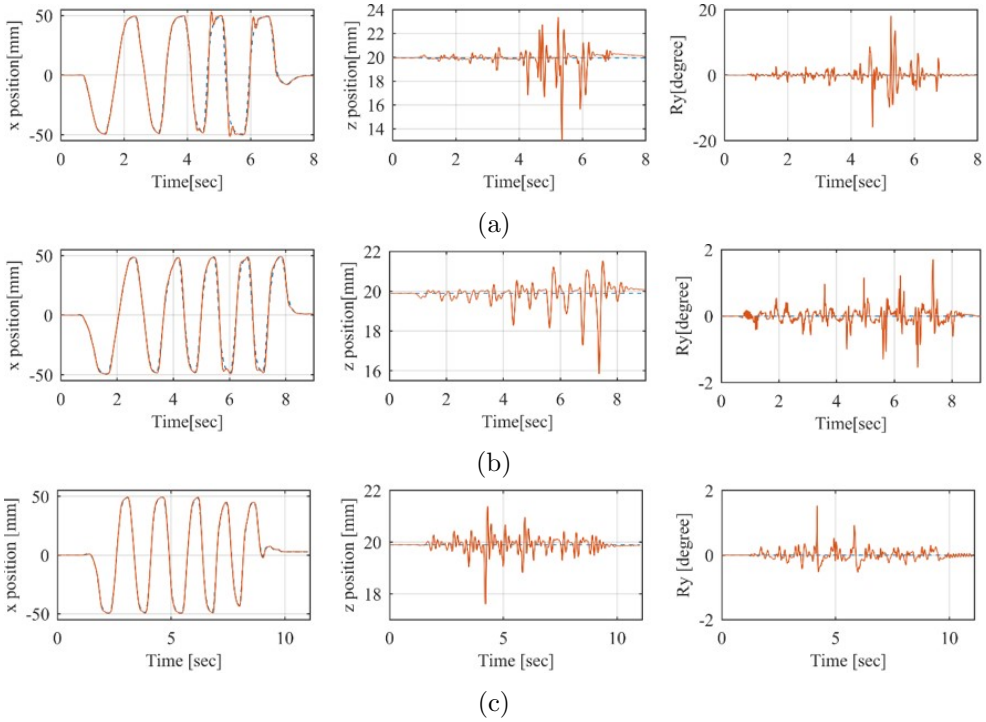


Figure 2.22: MagTable experiment results: High-speed sweep motion.
(a) Single 2-inch magnet. **(b)** Single 3-inch magnet. **(c)** Three 2-inch magnet.

2.6 Summary

In summary, there are several proposed methods and techniques to design, analysis, and control the planar maglev stages.

In terms of design, the planar maglev system consists of two parts: the stator and the mover. Most of the stators were electromagnets which are in the form of conductor wires or coil arrays. The configuration of the stator can be multi-layer conducting wires, single or multiple coils arrays. For the magnet mover, it can be 1-D, 2-D Halbach arrays, or disc magnets. The Halbach array is very popular because it can provide a strong magnetic field on one side and faces down to the stator.

For system modeling, most planar maglev systems are based on the Lorentz force law. The 3-D wrench on the mover is the reaction wrench from the coils immersed in the magnetic field generated by the permanent magnets. The wrench model is used to decouple the cross-coupling effect in levitation at any mover pose. The system controllability can be considered from the condition number of the wrench matrix. The lower condition number means better controllability of the system.

The preliminary study on the MagTable was reviewed in this chapter. The system was designed to have a stator with an array of 70 coils and disc-magnet movers. Experiment results demonstrate feasibility of the system for real-world applications and opportunities for future developments.

Part I

Modular Planar Magnetic Levitation System Design

Chapter 3

Magnetic Levitation Modeling

This chapter presents the Lorentz force-based forces and torques or wrench model in Lorentz levitation. An implementation of the model for wrench–current decoupling in the real-time control system is described. Next, multivariate linear interpolation is used to enhance the decoupling performance. A decoupling strategy for long-range planar motion with small-range lookup data is developed for efficient use of data storage.

3.1 Lorentz Levitation Model

Recall the 3-D wrench model for Lorentz levitation in Chapter 2, this section presents the wrench model between a single coil and a single magnet with solutions to two challenges. First, the magnetic nodes approach is used to compute the magnetic flux density from a disc magnet. Since the magnet mover can freely levitate in the air, the orientation of the mover is also considered. Second, the Gaussian quadrature technique is used to approximate the triple integral as discrete summations by defining Gaussian nodes and weights on the coil.

$$\boldsymbol{F} = -\iiint_{V_{coil}} \boldsymbol{J} \times \boldsymbol{B} \, \mathrm{d}V \,. \tag{3.1}$$

$$\boldsymbol{T} = -\iiint_{V_{coil}} \boldsymbol{r} \times (\boldsymbol{J} \times \boldsymbol{B}) \, \mathrm{d}V \,. \tag{3.2}$$

In general, the planar magnetic levitation system consists of three main coordinate systems defined at pre-superscript of the vectors as described follows:

$\{o\}$ *System coordinate* or *origin*: Locate at the center of coil array top surface,

$\{c\}$ *Coil coordinate*: Locate at the center of the coil top surface,

$\{m\}$ *Magnet coordinate*: Locate at the middle of permanent magnet mover.

Figure 3.1 represents an example of the planar maglev system with a single-disc magnet mover. The electromagnet array has 10 square coils arranged in a zigzag pattern with an offset. The system origin is set at the center of the coil array top surface. The disc-magnet mover is levitated above the coil array with mover center at the location $\boldsymbol{p} = [\,x,\, y,\, z\,]^{\mathsf{T}}$ with orientation $\boldsymbol{q} = [\,\phi,\, \theta,\, \psi\,]^{\mathsf{T}}$ referred to the origin. Point $\boldsymbol{x}$ represents an arbitrary point of interest in the coil. Point $\boldsymbol{x}$ in coil ci coordinate can be defined as ${}^{ci}\boldsymbol{x}$. The vector $\boldsymbol{r}$ represents the position of point $\boldsymbol{x}$ relative to the center of the magnet $\boldsymbol{r} = {}^{o}\boldsymbol{x}_{ci} - \boldsymbol{p}$.

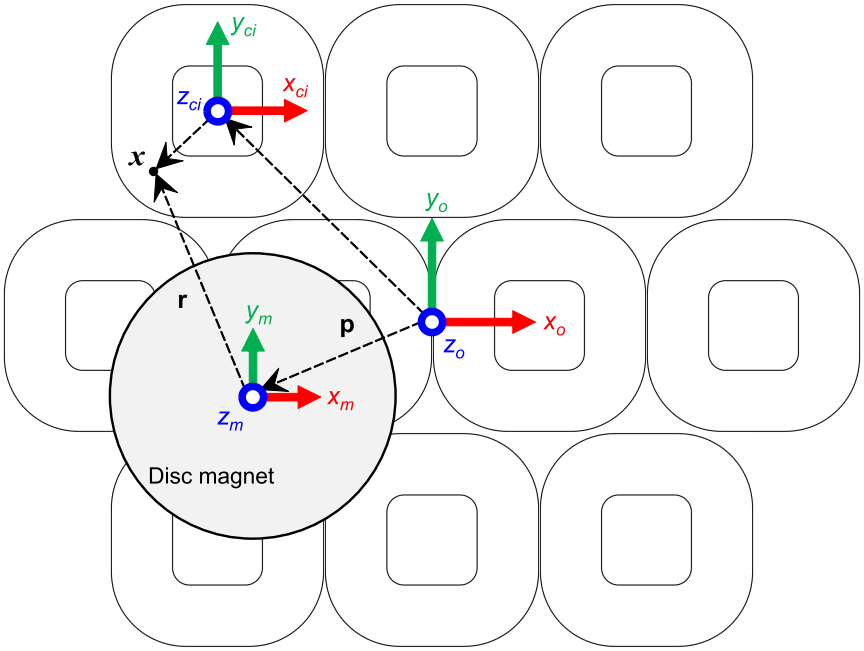


Figure 3.1: Coordinate systems in planar magnetic levitation.

3.1.1 Magnetic Flux Density Computation

By using magnetic nodes method, the magnetic flux density $\boldsymbol{B}$ at any points of interest $\boldsymbol{x}$ in the mover coordinate is denoted by ${}^{m}\boldsymbol{B} = \left[\, {}^{m}B_x, {}^{m}B_y, {}^{m}B_z \,\right]^{\mathsf{T}}$. Hence, the coil node n of coil i in system coordinate ${}^{o}\boldsymbol{x}_{ci,n}$ must be transformed into mover coordinate ${}^{m}\boldsymbol{x}_{ci,n}$ by:

$$ {}^{m}\boldsymbol{x}_{ci,n} = (\mathbf{R}_{\mathrm{xyz}})^{-1} \cdot ({}^{o}\boldsymbol{x}_{ci,n} - \boldsymbol{p}) \,. \tag{3.3} $$

The magnet orientation in 3-D has three rotation angles $\boldsymbol{q} = [\,\psi, \theta, \phi\,]^{\mathsf{T}}$ is considered in R_z(yaw, ϕ)–R_y(pitch, θ)–R_x(roll, ψ) order of rotation as presented by:

$$ \begin{aligned} \mathbf{R}_{\mathrm{xyz}} &= \mathbf{R}_{\mathrm{x}(\psi)} \cdot \mathbf{R}_{\mathrm{y}(\theta)} \cdot \mathbf{R}_{\mathrm{z}(\phi)} \\ &= \begin{bmatrix} 1 & 0 & 0 \\ 0 & \cos\psi & -\sin\psi \\ 0 & \sin\psi & \cos\psi \end{bmatrix} \cdot \begin{bmatrix} \cos\theta & 0 & \sin\theta \\ 0 & 1 & 0 \\ -\sin\theta & 0 & \cos\theta \end{bmatrix} \cdot \begin{bmatrix} \cos\phi & -\sin\phi & 0 \\ \sin\phi & \cos\phi & 0 \\ 0 & 0 & 1 \end{bmatrix} . \end{aligned} \tag{3.4} $$

The magnetic flux density from each magnetic node k (${}^{m}\boldsymbol{x}_{m,k}$) at coil node n (${}^{m}\boldsymbol{x}_{ci,n}$) can be computed by:

$$ {}^{m}B_x = \sum_{g=0}^{1} \sum_{k=1}^{M} (-1)^{(k+g)} \frac{B_r}{4\pi} \ln\left(-y_r + \sqrt{x_r^2 + y_r^2 + z_r^2} \,\right) , \tag{3.5a} $$

$$ {}^{m}B_y = \sum_{g=0}^{1} \sum_{k=1}^{M} (-1)^{(k+g)} \frac{B_r}{4\pi} \ln\left(-x_r + \sqrt{x_r^2 + y_r^2 + z_r^2} \,\right) , \tag{3.5b} $$

$$ {}^{m}B_z = \sum_{g=0}^{1} \sum_{k=1}^{M} (-1)^{(k+g)} \frac{B_r}{4\pi} \arctan\left(\frac{x_r y_r}{z_r \sqrt{x_r^2 + y_r^2 + z_r^2}} \right) , \tag{3.5c} $$

where $\left[\, x_r,\, y_r,\, z_r \,\right]^{\mathsf{T}} = {}^{m}\boldsymbol{x}_{ci,n} - {}^{m}\boldsymbol{x}_{m,k}$. The magnet bottom ($g = 0$) and top ($g = 1$) surfaces have M magnetic nodes with remanent magnetization B_r.

Finally, the magnetic field in coil coordinate can be obtained by transforming the magnetic field from magnet coordinate back to coil coordinate by:

$$ {}^{c}\boldsymbol{B} = \mathbf{R}_{\mathrm{xyz}} \cdot {}^{m}\boldsymbol{B} \,. \tag{3.6} $$

The magnetic flux density from magnet mover to any points of interest can be computed. This is further used to compute the Lorentz forces and torques on the mover from each coil immersed in the magnetic field in this chapter.

3.1.2 Magnetic Force and Torque Computation

The Gaussian quadrature technique is used to approximate the integral as the summation of the functions by [92]:

$$\int_{x_{low}}^{x_{up}} f(x)\mathrm{d}x = \frac{x_{up} - x_{low}}{2} \sum_{n=1}^{N} w_n f\left(\frac{x_{up} + x_{low}}{2} + \zeta_n \frac{x_{up} - x_{low}}{2}\right). \tag{3.7}$$

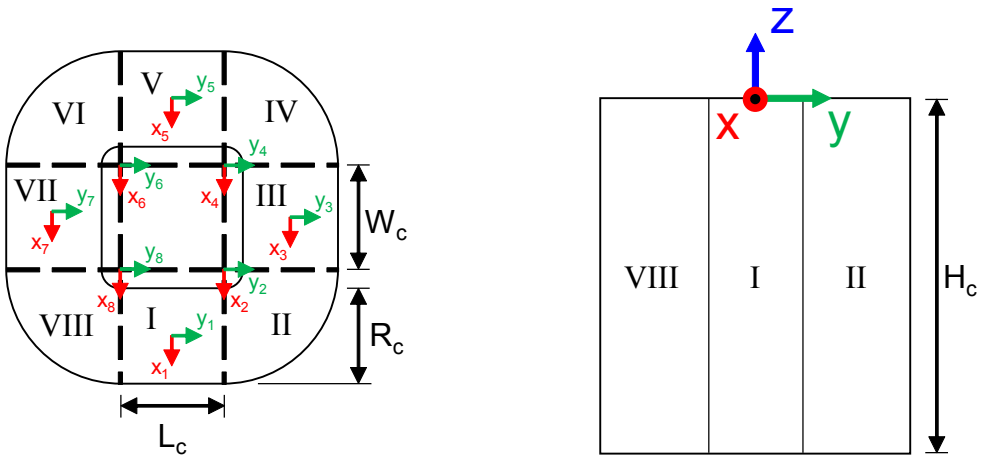
Table 3.1 provides the Gaussian node ζ_n and weight w_n for number of points $N = 1$ to 4. In this work, a rounded-corner square coil as depicted in Fig. 3.2 has rectangle section width W_c, rectangle section length L_c, corner radius R_c, and height H_c. The coil has its origin at the center of the coil top surface. Similar to [55], the coil is divided into four rectangle sections and four rounded corner sections. Each section is modeled to have Gaussian nodes $N = 4$ in all directions. There are $N^3 = 64$ nodes in each section as shown in Fig. 3.3a.

Table 3.1: Gaussian node and weight for number of points $N = 1$ to 4.

N	Nodes, ζ_n	Weights, w_n
1	0	2
2	$\pm\frac{1}{\sqrt{3}} \approx \pm 0.57735...$	1
3	0	$\frac{8}{9} \approx 0.88889...$
	$\pm\sqrt{\frac{3}{5}} \approx \pm 0.774597...$	$\frac{5}{9} \approx 0.55556...$
4	$\pm\sqrt{\frac{3}{7} - \frac{2}{7}\sqrt{\frac{6}{5}}} \approx \pm 0.339981...$	$\frac{18+\sqrt{30}}{36} \approx 0.652145...$
	$\pm\sqrt{\frac{3}{7} + \frac{2}{7}\sqrt{\frac{6}{5}}} \approx \pm 0.861136...$	$\frac{18-\sqrt{30}}{36} \approx 0.347855...$

For the current direction, by default, the positive current direction is counter-clockwise as shown in Fig. 3.3b. Hence, the magnetization points upward along +Z-axis. The current density magnitude J can be calculated by:

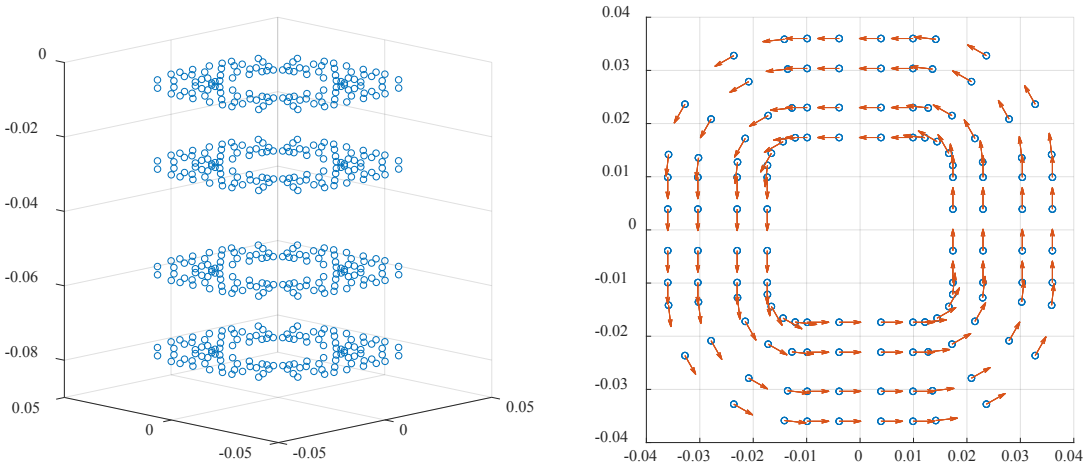
$$J = \frac{N_{coil} \cdot I}{R_c \cdot H_c}. \tag{3.8}$$



(a) Coil sections - Top view.

(b) Coil sections - Front view.

Figure 3.2: Coil sections.



(a)

(b)

Figure 3.3: Gaussian nodes on the coil. **(a)** Isometric view. **(b)** Top view with current direction.

Rectangle Section

The position ${}^{ci}\boldsymbol{x}_n$ and weight $\tilde{w}_n$ of the Gaussian nodes in the rectangle section $s = 1, 3, 5, 7$ of coil ci at position $\boldsymbol{c}_i$ can be determined by:

$$ {}^{ci}\boldsymbol{x}_n = \begin{cases} \left[\zeta_{n_1}\dfrac{R_c}{2},\ \zeta_{n_2}\dfrac{L_c}{2},\ (\zeta_{n_3}-1)\dfrac{H_c}{2}\right]^{\mathsf{T}} + \boldsymbol{c}_i & \textbf{for } s = 1, 5 \\ \left[\zeta_{n_1}\dfrac{W_c}{2},\ \zeta_{n_2}\dfrac{R_c}{2},\ (\zeta_{n_3}-1)\dfrac{H_c}{2}\right]^{\mathsf{T}} + \boldsymbol{c}_i & \textbf{for } s = 3, 7 \end{cases} \tag{3.9} $$

$$ \tilde{w}_n = \begin{cases} w_{n1}\cdot w_{n2}\cdot w_{n3}\cdot \dfrac{L_c}{2}\cdot\dfrac{R_c}{2}\cdot\dfrac{H_c}{2} & \textbf{for } s = 1, 5 \\ w_{n1}\cdot w_{n2}\cdot w_{n3}\cdot \dfrac{R_c}{2}\cdot\dfrac{W_c}{2}\cdot\dfrac{H_c}{2} & \textbf{for } s = 3, 7 \end{cases} \tag{3.10} $$

The current density vector $\boldsymbol{J}$ of each coil node in rectangle section has x or y-component depends on the coil rectangle section $s = 1, 3, 5, 7$ as expressed by:

$$ {}^{c}\boldsymbol{J}_{({}^{ci}\boldsymbol{x}_n)} = \begin{cases} J\cdot\left[\ 0\ ,\ \sin\dfrac{(3-s)\pi}{4},\ 0\ \right]^{\mathsf{T}} & \textbf{for } s = 1, 5 \\ J\cdot\left[-\cos\dfrac{(s-3)\pi}{4},\ 0\ ,\ 0\ \right]^{\mathsf{T}} & \textbf{for } s = 3, 7 \end{cases} \tag{3.11} $$

Hence, the forces and torques in the rectangle section can be computed by:

$$ \begin{aligned} {}^{c}\boldsymbol{F}_{i(\boldsymbol{p},\,\boldsymbol{q})} &= -\int_{-H_c}^{0}\int_{y_{in}}^{y_{out}}\int_{x_{in}}^{x_{out}} {}^{c}\boldsymbol{J}\times{}^{c}\boldsymbol{B}_{(\boldsymbol{p},\boldsymbol{q})}\,\mathrm{d}x\,\mathrm{d}y\,\mathrm{d}z \\ &= -\sum_{n=1}^{N^3}\tilde{w}_n\cdot{}^{c}\boldsymbol{J}_{({}^{ci}\boldsymbol{x}_n)}\times{}^{c}\boldsymbol{B}_{(\boldsymbol{p},\boldsymbol{q},{}^{ci}\boldsymbol{x}_n)}\,. \end{aligned} \tag{3.12} $$

$$ \begin{aligned} {}^{c}\boldsymbol{T}_{i(\boldsymbol{p},\,\boldsymbol{q})} &= -\int_{-H_c}^{0}\int_{y_{in}}^{y_{out}}\int_{x_{in}}^{x_{out}} \boldsymbol{r}_{(\boldsymbol{p})}\times\left({}^{c}\boldsymbol{J}\times{}^{c}\boldsymbol{B}_{(\boldsymbol{p},\boldsymbol{q})}\right)\mathrm{d}x\,\mathrm{d}y\,\mathrm{d}z \\ &= -\sum_{n=1}^{N^3}\tilde{w}_n\cdot\boldsymbol{r}_{(\boldsymbol{p},{}^{ci}\boldsymbol{x}_n)}\times\left({}^{c}\boldsymbol{J}_{({}^{ci}\boldsymbol{x}_n)}\times{}^{c}\boldsymbol{B}_{(\boldsymbol{p},\boldsymbol{q},{}^{ci}\boldsymbol{x}_n)}\right). \end{aligned} \tag{3.13} $$

Rounded Corner Section

The position ${}^{ci}\boldsymbol{x}_n$ and weight $\tilde{w}_n$ of the Gaussian nodes in the rounded corner section $s = 2, 4, 6, 8$ of coil ci at position $\boldsymbol{c}_i$ can be determined by:

$$ {}^{ci}\boldsymbol{x}_n = \begin{bmatrix} \left(R_{in} + (1+\zeta_{n_1})\dfrac{R_c}{2}\right) \cdot \cos\dfrac{(\zeta_{n_2} - 1 + s)\pi}{4} \\ \left(R_{in} + (1+\zeta_{n_1})\dfrac{R_c}{2}\right) \cdot \sin\dfrac{(\zeta_{n_2} - 1 + s)\pi}{4} \\ (\zeta_{n_3} - 1)\dfrac{H_c}{2} \end{bmatrix} + \boldsymbol{c}_i \,. \tag{3.14} $$

$$ \tilde{w}_n = w_{n1} \cdot w_{n2} \cdot w_{n3} \cdot \frac{R_c}{2} \cdot \frac{\pi}{4} \cdot \frac{H_c}{2} \,. \tag{3.15} $$

The current density vector $\boldsymbol{J}$ of each coil node in rounded corner section has x and y-component depends on the coil rounded corner section $s = 2, 4, 6, 8$ expressed by:

$$ {}^{c}\boldsymbol{J}_{({}^{ci}\boldsymbol{x}_n)} = \begin{bmatrix} J \cdot -\sin\left(\dfrac{\pi}{4}(\zeta_{n_2} - 1) + \dfrac{s \cdot \pi}{4}\right) \\ J \cdot \cos\left(\dfrac{\pi}{4}(\zeta_{n_2} - 1) + \dfrac{s \cdot \pi}{4}\right) \\ 0 \end{bmatrix} . \tag{3.16} $$

Hence, the forces and torques in the rounded corner section can be computed by:

$$ \begin{aligned} {}^{c}\boldsymbol{F}_{i(\boldsymbol{p},\,\boldsymbol{q})} &= -\int_{-H_c}^{0} \int_{\frac{i-2}{4}\pi}^{\frac{i}{4}\pi} \int_{R_{in}}^{R_{out}} {}^{c}\boldsymbol{J} \times {}^{c}\boldsymbol{B}_{(\boldsymbol{p},\boldsymbol{q})} \cdot \rho \,\mathrm{d}x \,\mathrm{d}y \,\mathrm{d}z \\ &= -\sum_{n=1}^{N^3} \tilde{w}_n \frac{R_c}{2}(1+\zeta_{n_1}) \cdot {}^{c}\boldsymbol{J}_{({}^{ci}\boldsymbol{x}_n)} \times {}^{c}\boldsymbol{B}_{(\boldsymbol{p},\boldsymbol{q},{}^{ci}\boldsymbol{x}_n)} \,. \end{aligned} \tag{3.17} $$

$$ \begin{aligned} {}^{c}\boldsymbol{T}_{i(\boldsymbol{p},\,\boldsymbol{q})} &= -\int_{-H_c}^{0} \int_{\frac{i-2}{4}\pi}^{\frac{i}{4}\pi} \int_{R_{in}}^{R_{out}} \boldsymbol{r}_{(\boldsymbol{p})} \times \left({}^{c}\boldsymbol{J} \times {}^{c}\boldsymbol{B}_{(\boldsymbol{p},\boldsymbol{q})}\right) \cdot \rho \,\mathrm{d}x \,\mathrm{d}y \,\mathrm{d}z \\ &= -\sum_{n=1}^{N^3} \tilde{w}_n \frac{R_c}{2}(1+\zeta_{n_1}) \cdot \boldsymbol{r}_{(\boldsymbol{p},{}^{ci}\boldsymbol{x}_n)} \times \left({}^{c}\boldsymbol{J}_{({}^{ci}\boldsymbol{x}_n)} \times {}^{c}\boldsymbol{B}_{(\boldsymbol{p},\boldsymbol{q},{}^{ci}\boldsymbol{x}_n)}\right) . \end{aligned} \tag{3.18} $$

This section proposed the magnetic flux density and wrench equations were developed as follows:

- Magnetic flux density $\boldsymbol{B}$ equations by magnetic nodes: Eq. (3.5).
- Force $\boldsymbol{F}$ equations in rectangle section: Eq. (3.12), and corner section: Eq. (3.17).
- Torque $\boldsymbol{T}$ equations in rectangle section: Eq. (3.13), and corner section: Eq. (3.18).

By substituting magnetic flux density equations into force and torque equations, the wrench equations between a single coil and a single magnet can be computed by:

$$\boldsymbol{F} = -\sum_{s=1}^{8}\sum_{n=1}^{N^3}\sum_{g=0}^{1}\sum_{k=1}^{M} w_g\, \boldsymbol{J} \times (\mathbf{R}_{\text{xyz}} \cdot \boldsymbol{B})\,. \tag{3.19}$$

$$\boldsymbol{T} = -\sum_{s=1}^{8}\sum_{n=1}^{N^3}\sum_{g=0}^{1}\sum_{k=1}^{M} w_g\, \boldsymbol{r} \times (\boldsymbol{J} \times (\mathbf{R}_{\text{xyz}} \cdot \boldsymbol{B}))\,. \tag{3.20}$$

where the moment arm $\boldsymbol{r}$ is the vector from the center of the magnet $\boldsymbol{p}$ to the coil node n in system coordinate ${}^{o}\boldsymbol{x}_{ci,n}$ expressed by:

$$\boldsymbol{r}_{(\boldsymbol{p},\boldsymbol{x}_{ci,n})} = {}^{o}\boldsymbol{x}_{ci,n} - \boldsymbol{p}\,. \tag{3.21}$$

The force and torque or wrench model obtained in this section is further used for the wrench–current decoupling. A validation of this wrench model is conducted in the next section by comparing the results with measurement and simulation.

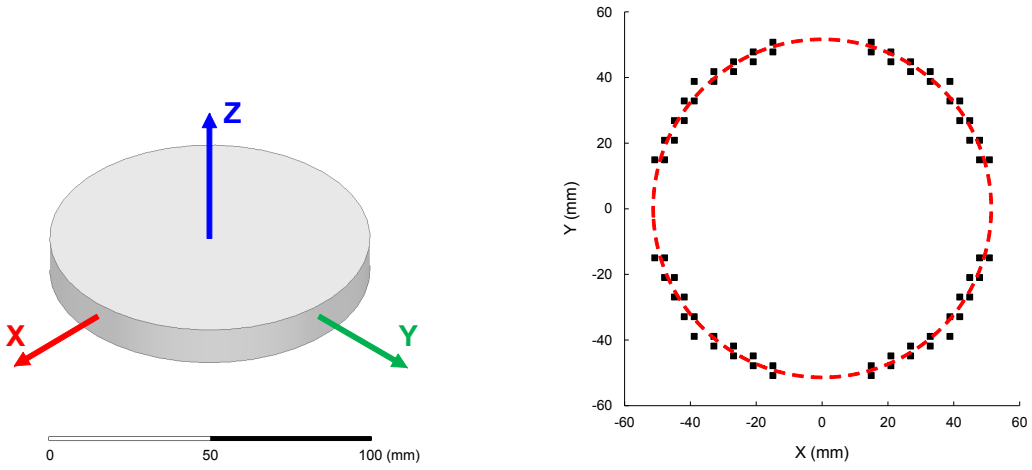
3.1.3 Model Validation

Magnetic Flux Density

To validate the calculation method for non-cubic magnet, the disc-shaped Neodymium magnet (NdFeB) grade N50 with specifications in Table 3.2 was selected. Figure 3.4 depicts the disc magnet model and its magnetic nodes representation for one layer. The magnetic nodes are first set at four corners in each quadrant. Then, the adjacent nodes are moving along X or Y axis which fit the circumference until it reaches the maximum radius in each axis. Each node has $B_{r\,max}$ to represent the magnetization of the magnet.

Table 3.2: Permanent disc magnet specifications

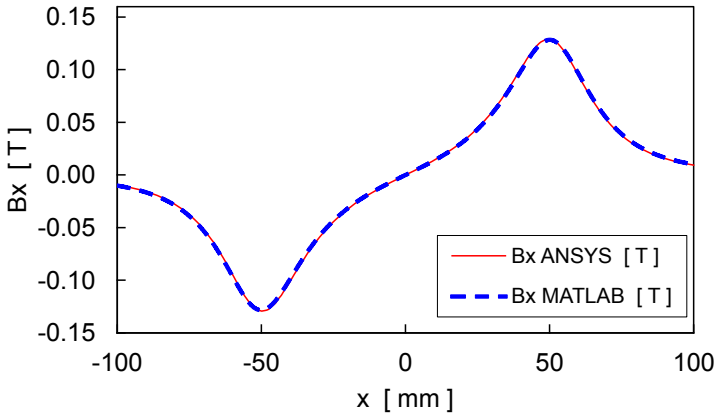
Description	**Value**	**Unit**
Diameter	101.60	mm
Thickness	12.70	mm
$B_{r\,max}$	1.45	Tesla



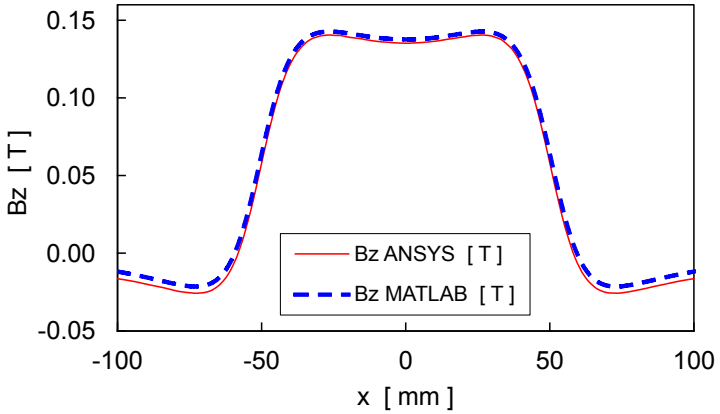
(a) Disc-shaped magnet model

(b) Magnetic node representation

Figure 3.4: Disc-shaped permanent magnet model in ANSYS and magnetic node representation



(a) B_x component



(b) B_z component

Figure 3.5: Magnetic field comparison above disc-shaped permanent magnet along X-axis at z = 20 mm

The validation of the magnetic field calculation using the magnetic nodes model is considered from comparison with the simulation results as shown in Fig. 3.5. As observed from the figure, the results from ANSYS and MATLAB are well matched for both B_x and B_z. The comparison results verified that the developed analytical model is valid.

Forces and Torques

This section further provides the validation of magnetic forces and torques between a single disc magnet and a single coil. The force and torque data were obtained from measurement, simulation, and computation using the proposed model.

For measurement[1], the system setup is shown in Fig. 3.6a. The 4-inch disc magnet is mounted on the fixture with an F/T sensor at the bottom to measure 3-D forces and torques. The F/T sensor (Gamma SI-65-5, ATI) has specifications as detailed in Table 3.3. The system origin is at the center of the magnet for coil position reference.

A square coil is mounted on an inclined aluminum bar. The coil can move along the Y axis with varied height. The coil current is 5 A. The coil position is measured by cameras. The measurement data is recorded along the Y axis. The curve fitting for coil position data is used to estimate the moving path in simulation and computation.

For the simulation in ANSYS, the system is modeled to be the same as the measurement setup as shown in Fig. 3.6b. The parametric simulation parameters are detailed in Table 3.4 (see Appendix A.3). The path is estimated from the previous step. The coil moves along the Y axis from -100 mm to 100 mm with a 5 mm step. The x and z positions are the function of the y position. The forces and torques are evaluated at the sensor coordinate.

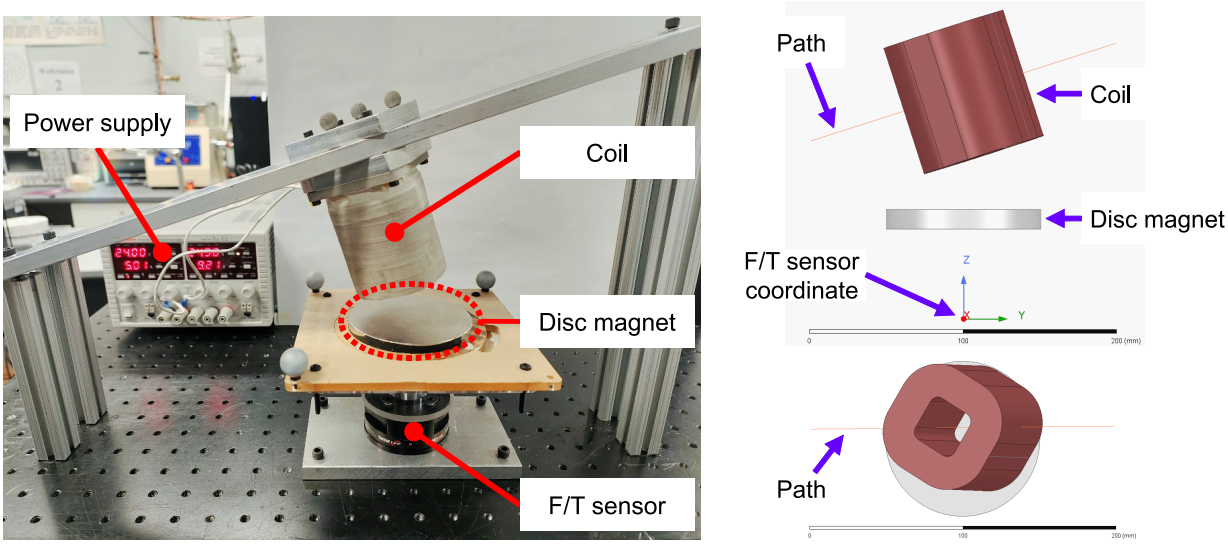
For force and torque computation, the wrench model is implemented in MATLAB to compute 5-DOF forces and torques at the sensor. The path is the same as the simulation but with a 1 mm step along the Y axis. However, the path must be transformed from the magnet coordinate to the global coordinate on the coil top surface before the computation.

The comparison of 5-DOF forces and torques between the three datasets is shown in Fig. 3.7. All data have similar trend with different errors. For F_y, F_z, and T_x, the proposed wrench model provides good result with small error. The larger error can be found in F_x and its cross product T_y, especially from -50 mm to -100 mm.

Table 3.3: Force and torque sensor specifications.

F/T	**Sensing ranges**		**Resolution**	
F_x, F_y	65	N	1/80	N
F_z	200	N	1/40	N
T_x, T_y, T_z	5	N·m	10/13333	N·m

[1]The force and torque measurement was a collaborative work with Zhenchuan Xu and Yang Wang, Maglev microrobotics laboratory, University of Waterloo.



(a) (b)

Figure 3.6: Force and torque measurement setup and simulation model.
(a) Measurement setup. **(b)** ANSYS simulation model (front and top views).

Table 3.4: Force and torque measurement and simulation parameters.

Parameters	**Value**	**Unit**
Path range		
X axis (x)	$-0.0105\,y - 7.3772$	mm
Y axis (y)	$[\,-100.0, 100.0\,]$	mm
Z axis (z)	$0.3202\,y + 83.4794$	mm
Roll angle	17.8440	degrees
Pitch angle	-0.6679	degrees
Yaw angle	-31.0465	degrees
Experiment setup		
Magnet to sensor distance	65.35	mm

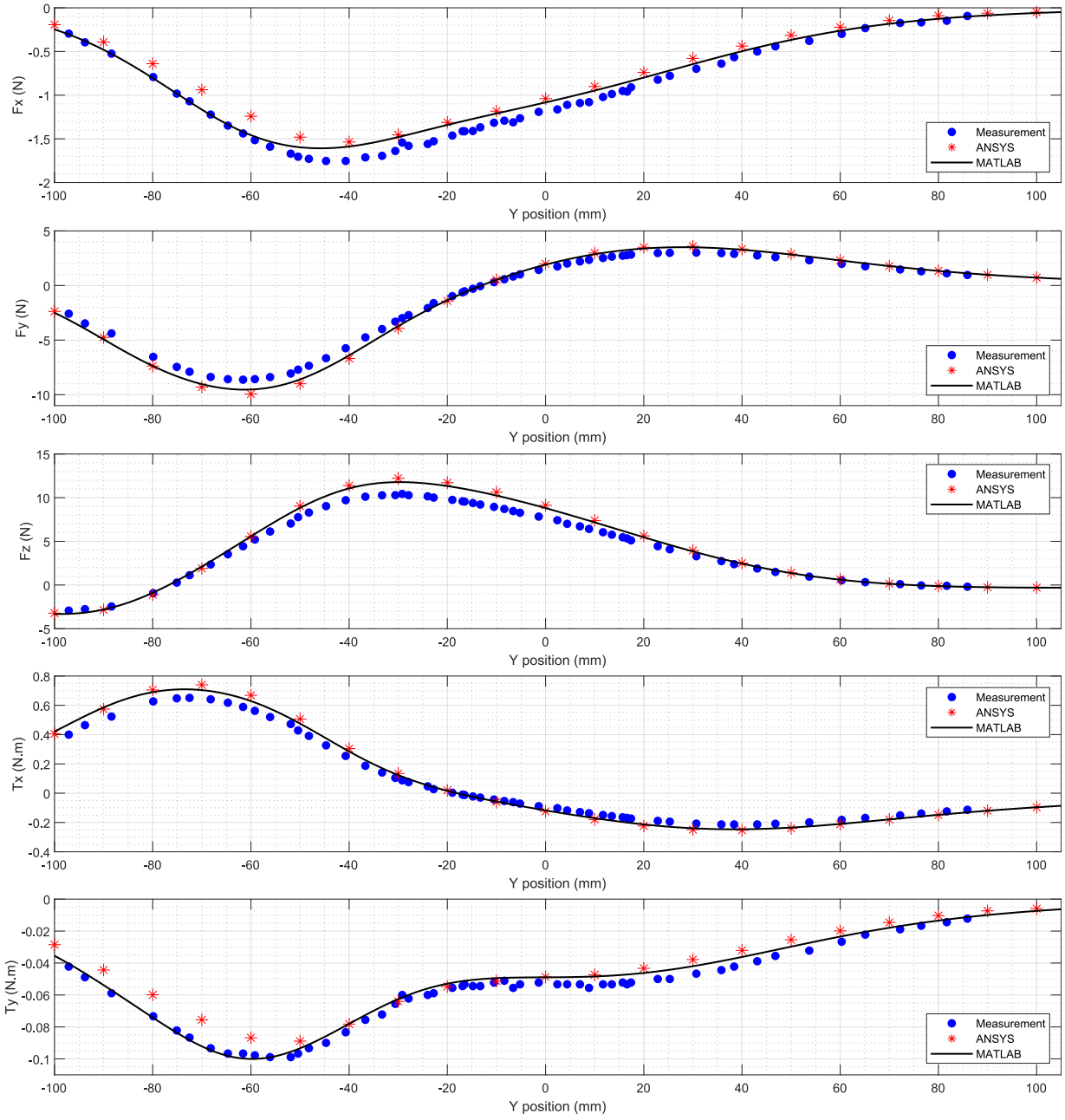


Figure 3.7: Forces and torques comparison.

3.2 Model Implementation for Real-Time Wrench–Current Decoupling

From Lorentz levitation model developed in the previous section, this section presents an implementation of the model for wrench–current decoupling in the real-time control system as reviewed Chapter 2.

3.2.1 Wrench–Current Decoupling

The purpose of this section is to develop a decoupling solution to the cross-coupling effect in the planar maglev system. With the cross-coupling effect, each degree of freedom of the mover cannot be controlled separately and becomes Multiple-Input Multiple-Output (MIMO) system. This effect causes difficulty in control.

The decoupling solution intends to decouple the MIMO system into multiple Single-Input Single-Output (SISO) systems. Since the controller outputs are desired wrench or forces and torques on the mover $\boldsymbol{w}_{desire}$, the coil currents $\boldsymbol{i}$ must be computed and assigned to all active coils. In this work, the wrench–current decoupling matrix $\mathbf{K}^{+}$ was used to determine the coil currents as expressed by:

$$\begin{aligned} \boldsymbol{w}_{actual} &= \mathbf{K}\,\boldsymbol{i} \\ &= \mathbf{K}\,(\mathbf{K}^{+}\,\boldsymbol{w}_{desire})\,. \end{aligned} \tag{3.22}$$

To realize the actual wrench $\boldsymbol{w}_{actual} = \boldsymbol{w}_{desired}$, the decoupling matrix $\mathbf{K}^{+}$ must be a right inverse to fulfill the condition $\mathbf{K}\,\mathbf{K}^{+} = \mathbf{I}$. Therefore, the decoupling matrix is an inverse of the wrench matrix $\mathbf{K}$. The wrench matrix $\mathbf{K}$ represents the relationship between the wrench and the coil currents. Usually, the number of active coils is more than the mover degrees-of-freedom. Hence, the wrench matrix is a non-square matrix.

For a non-square matrix, the inverse of the wrench matrix can be obtained by using the Moore-Penrose pseudoinverse. Since the $\mathbf{K}^{+}$ is a right inverse, the pseudoinverse can be computed by:

$$\mathbf{K}^{+} = \mathbf{K}^{\mathsf{T}}(\mathbf{K}\,\mathbf{K}^{\mathsf{T}})^{-1}. \tag{3.23}$$

In this work, both $\mathbf{K}$ and $\mathbf{K}^{+}$ matrices were used for the design, analysis, simulation, and control of the planar maglev system, Maglev Floor, and its prototypes.

3.2.2 Lookup Table Method

For real-time decoupling, the decoupling matrix $\mathbf{K}^{+}$ must be obtained within the control sampling time of 1 ms. The wrench matrix $\mathbf{K}$ requires parallel computation to compute Equations (3.19) and (3.20) which is not suitable for an existing controller. As a result, it is difficult to implement this model in the real-time control system.

In this work, a lookup table method is used to retrieve the decoupling matrix from pre-computed wrench matrices stored in data memory. An advantage of this method is a slight increase in computation time in real-time control. On the other hand, the memory used to store the data is directly proportional to the number of data steps.

The lookup table is constructed in row number order. The sequence of the lookup pose is Yaw (ϕ)-Pitch (θ)-Roll (ψ)-Z-Y-X, respectively. The pose value varies from minimum values to maximum values with increment steps for each degree of freedom (DOF). The data was then saved in CSV format for analysis and in binary format for real-time control.

For lookup index, the first and last row numbers of the desired data are computed by:

$$\begin{aligned}\text{first row number } &= 1 + (tx_i - 1) \cdot w_{tx} + (ty_i - 1) \cdot w_{ty} + (tz_i - 1) \cdot w_{tz} \\ &\quad + (rx_i - 1) \cdot w_{rx} + (ry_i - 1) \cdot w_{ry} + (rz_i - 1) \cdot w_{rz}\,, \end{aligned} \tag{3.24}$$

$$\text{last row number } = \text{first row number} + (\text{DOF} - 1)\,, \tag{3.25}$$

where $(tx_i, ty_i, tz_i, rx_i, ry_i, rz_i)$ are closest data index number for each DOF. The weight w is a multiplication of number of data steps N and number of DOF as shown in Table 3.5.

This section presents the wrench–current decoupling solution in real-time control using the lookup table method. The detail of the lookup data range for both 5-DOF and 6-DOF motions are described in experiments.

Table 3.5: Lookup first row index weight for each DOF.

DOF	**5-DOF weight**	**6-DOF weight**
X	$w_{tx} = N_{ty} \cdot N_{tz} \cdot N_{rx} \cdot N_{ry} \cdot 5$	$w_{tx} = N_{ty} \cdot N_{tz} \cdot N_{rx} \cdot N_{ry} \cdot N_{rz} \cdot 6$
Y	$w_{ty} = N_{tz} \cdot N_{rx} \cdot N_{ry} \cdot 5$	$w_{ty} = N_{tz} \cdot N_{rx} \cdot N_{ry} \cdot N_{rz} \cdot 6$
Z	$w_{tz} = N_{rx} \cdot N_{ry} \cdot 5$	$w_{tz} = N_{rx} \cdot N_{ry} \cdot N_{rz} \cdot 6$
Roll (ψ)	$w_{rx} = N_{ry} \cdot 5$	$w_{rx} = N_{ry} \cdot N_{rz} \cdot 6$
Pitch (θ)	$w_{ry} = 5$	$w_{ry} = N_{rz} \cdot 6$
Yaw (ϕ)	N/A	$w_{rz} = 6$

3.3 Wrench–Current Decoupling Enhancement Using Multivariate Linear Interpolation

By using the lookup table method, the wrench–current decoupling matrix is computed from the nearest wrench matrix. Even though this method has an advantage in real-time computation efficiency, the lookup table method has a problem with its discrete data.

The decoupling effectiveness at the no-data poses can deteriorate because of the error from the nearest wrench matrix which is acquired for decoupling matrix computation. When the mover has the pose in the middle of two states in any DOF, the selected data can abruptly switch between two data due to the motion feedback noise and cause inconsistent errors. As a result, the overall controller performance is degraded and the system may become unstable.

Therefore, an implementation of estimation techniques to estimate the wrench matrix at the no-data poses can enhance the levitation performance. In this work, a multivariate linear interpolation was selected. With interpolated data, the discrete lookup data become continuous to solve the switching data problem. This method can simply deploy and it is feasible for a control system with limited computational resources.

The multivariate linear interpolation for the 6-DOF wrench matrix can be formulated as follows. Suppose that the 6-DOF mover pose at (x_0, y_0, z_0, ψ_0, θ_0, ϕ_0), which are between the state pairs, (x_1, x_2), (y_1, y_2), (z_1, z_2), (ψ_1, ψ_2), (θ_1, θ_2), and (ϕ_1, ϕ_2), respectively. The a_x, a_y, a_z, a_ψ, a_θ, and a_ϕ represent the weighting parameters for the multivariate linear interpolation of x, y, z, ψ, θ, and ϕ states of the mover pose, respectively. The weighting parameters a_s can be calculated by:

$$a_s = \frac{s_0 - s_2}{s_1 - s_2} \qquad \text{with } s_1 \leq s_0 \leq s_2 \tag{3.26}$$

where s can be x, y, z, ψ, θ, or ϕ state of the mover pose. Once the weighting parameters are obtained, the general results of the interpolated 6-DOF wrench matrix can be found for any desired states as expressed by:

$$\mathbf{K}_0 = \sum_{i=1}^{2}\sum_{j=1}^{2}\sum_{k=1}^{2}\sum_{l=1}^{2}\sum_{m=1}^{2}\sum_{n=1}^{2}\left\{ \prod_{s=x_i}^{\phi_n} a_s \cdot \mathbf{K}_{(x_i,y_j,z_k,\psi_l,\theta_m,\phi_n)} \right\}. \tag{3.27}$$

An implementation of Eq. (3.27) to estimate $\mathcal{N}$ states of the d-DOF wrench matrix $\mathbf{K}$ is detailed in Table 3.6. The coil array has N_{coil} coils.

Table 3.6: Multivariate linear interpolation.

Algorithm 1 Multivariate linear interpolation

Require: A pre-computed lookup table
INPUT The sensor mover pose d-DOF (x_0, y_0, z_0, ψ_0, θ_0, ϕ_0) only work with the states needed
OUTPUT The interpolated results $\mathbf{K}_0$
STATE Initialization $\mathbf{K}_0 = \text{zeros}(d, N_{coil})$, and number of states to be interpolated $\mathcal{N}$
STATE Calculate the weights $a_{s^1} = \dfrac{s_0 - s_2}{s_1 - s_2}$ and $a_{s^2} = 1 - a_{s^1}$
WHILE $i \leq 2^{\mathcal{N}}$
  STATE lookup $\mathbf{K}_i$
  STATE find the $\prod a_s$ product
  STATE $\mathbf{K}_0 = \mathbf{K}_0 + \prod a_s \cdot \mathbf{K}_i$
  STATE $i = i + 1$
ENDWHILE

For a single-disc magnet mover, the maximum controllable degree of freedom is limited to 5-DOF without yaw rotation. To apply 5-DOF linear interpolation, the required number of wrench matrices is $\mathcal{N}_{\text{5-DOF}} = 2^5 = 32$ matrices. For a multiple-disc magnet mover, the maximum controllable degree of freedom is 6-DOF. To apply 6-DOF linear interpolation, the required number of wrench matrices is $\mathcal{N}_{\text{6-DOF}} = 2^6 = 64$ matrices. Once the estimated wrench matrix $\mathbf{K}_0$ at the given mover pose is obtained, the estimated wrench–current decoupling matrix $\mathbf{K}_0^+$ can be computed by using Moore-Penrose pseudoinverse as described in the previous section.

This section provides the solution to enhance the decoupling performance using multivariate linear interpolation. This method can approximate the wrench–current decoupling matrix at no-data pose from neighbor decoupling matrices in lookup data. An evaluation of this solution will be conducted in both 5-DOF and 6-DOF levitation experiments.

3.4 Wrench–Current Decoupling Strategy for Long-Range Planar Motion

The problem of the lookup table method with discrete lookup data was solved by the multivariate linear interpolation to estimate the wrench–current decoupling matrix in the previous section. However, another remaining limitation of the lookup table method is the limited range of data which limits the levitation range.

Since the memory used to store the lookup table data is directly proportional to the number of pose combinations, the larger range of levitation requires a larger size of the lookup table. Therefore, a strategy to achieve long-range levitation with a small-range lookup table is needed for the efficient use of data memory.

In this work, the decoupling strategy for long-range levitation using short-range lookup data is developed for the Proto-MagFloor system. The number of active coils for levitation is 16 coils arranged in a 4-by-4 array. The lookup data is pre-computed within the minimum planar range of the quarter coil area in the 1st quadrant of the coil array. Overall, the proposed strategy has 4 steps as described below:

STEP 1: Active coil array selection

Figure 3.8a depicts the concept of active coil array selection. The cross marks (+) represent the center of 4-by-4 active coils. The active coil array can be determined by the mover location. The 16 coils highlighted in green are selected active coils for this mover pose since the center of this array is the nearest center to the mover.

For Proto-MagFloor system, the centers ($\boldsymbol{x}_{grid}$, $\boldsymbol{y}_{grid}$) of all possible 4-by-4 active coil array in millimeter unit are:

$$\boldsymbol{x}_{grid} = [\ -152.4, -76.2,\ \ 0.0,\ \ \ 76.2,\ \ \ 152.4\ ]\ , \tag{3.28a}$$

$$\boldsymbol{y}_{grid} = [\ \ \ 152.4,\ \ \ 76.2,\ \ 0.0, -76.2, -152.4\ ]\ . \tag{3.28b}$$

The nearest active coil array center to the mover position (x_m, y_m) can be determined by finding the coil center index ($\text{index}_x, \text{index}_y$) which provides minimum distance from:

$$\text{index}_x = \min\Big\{ \|\boldsymbol{x}_{grid} - x_m\| \Big\}\ , \tag{3.29a}$$

$$\text{index}_y = \min\Big\{ \|\boldsymbol{y}_{grid} - y_m\| \Big\}\ . \tag{3.29b}$$

Once the active coil array center coordinate was determined from ($\boldsymbol{x}_{grid}$, $\boldsymbol{y}_{grid}$) by the center index, all 16 active coils of the 4-by-4 coil array can be obtained, for example, the highlighted coils in Fig. 3.8a.

STEP 2: Pose transformation to the first quadrant (Q1)

From step 1, the relative mover pose ($\boldsymbol{p}$, $\boldsymbol{q}$) to the relative quadrant (Qn) of the active coil array can be computed. Figure 3.8b represents the mover is in the third quadrant (Q3) of the array. The relative mover pose to the coil array center is shown in Fig. 3.8c.

Since the lookup data is only pre-computed for Q1, the equivalent pose ($\boldsymbol{p}_{Q1}$, $\boldsymbol{q}_{Q1}$) of the mover from other quadrants is transformed to Q1 by:

$$\begin{bmatrix} \boldsymbol{p}_{Q1} \\ \boldsymbol{q}_{Q1} \end{bmatrix} = \begin{bmatrix} \boldsymbol{\Omega}_{Qn\to1} & \mathbf{0}_{3\times3} \\ \mathbf{0}_{3\times3} & \boldsymbol{\Omega}_{Qn\to1} \end{bmatrix} \cdot \begin{bmatrix} \boldsymbol{p} \\ \boldsymbol{q} \end{bmatrix}, \tag{3.30}$$

$$\boldsymbol{\Omega}_{Q2\to1} = \begin{bmatrix} 0 & 1 & 0 \\ -1 & 0 & 0 \\ 0 & 0 & 1 \end{bmatrix}, \ \boldsymbol{\Omega}_{Q3\to1} = \begin{bmatrix} -1 & 0 & 0 \\ 0 & -1 & 0 \\ 0 & 0 & 1 \end{bmatrix}, \ \boldsymbol{\Omega}_{Q4\to1} = \begin{bmatrix} 0 & -1 & 0 \\ 1 & 0 & 0 \\ 0 & 0 & 1 \end{bmatrix}, \tag{3.31}$$

where $\boldsymbol{\Omega}_{Qn\to1}$ is relationship of between x, y, and z-components of other quadrant to the first quadrant. $\mathbf{0}_{3\times3}$ is 3-by-3 zero matrix.

STEP 3: Lookup and interpolation for the wrench matrix

The lookup index can be computed by equivalent pose in the first quadrant ($\boldsymbol{p}_{Q1}$, $\boldsymbol{q}_{Q1}$), and looked up for the wrench matrix from the data table $\mathbf{K}_{Q1}$. An implementation of multivariate linear interpolation can be used to estimate the wrench matrix.

If multivariate linear interpolation is used, this step first computes all lookup indices and searches for all related states. Then, the estimated wrench matrix is computed as described in the previous section.

STEP 4: Wrench matrix transformation to the original quadrant (Qn)

Finally, the wrench matrix in the first quadrant $\mathbf{K}_{Q1}$ is transformed back to the original quadrant. The wrench matrix in the original quadrant $\mathbf{K}_{Qn}$ can be obtained by mapping the coil number or column number of the wrench matrix in Q1 to Qn and transform x, y, and z-components of the wrench matrix by:

$$\mathbf{K}_{Qn} = \begin{bmatrix} \boldsymbol{\Omega}_{Qn\to1}^{\mathsf{T}} & \mathbf{0}_{3\times3} \\ \mathbf{0}_{3\times3} & \boldsymbol{\Omega}_{Qn\to1}^{\mathsf{T}} \end{bmatrix} \cdot \mathbf{K}_{Q1}(:, \boldsymbol{c}_{Qn}), \tag{3.32}$$

The columns of $\mathbf{K}_{Q1}$ are swapped by the column order for each original quadrant $\boldsymbol{c}_{Qn}$. The column order $\boldsymbol{c}_{Qn}$ is obtained by rotating the coil number matrix by $Qn \cdot 90$ degrees counter-clockwise and flattening the rotated matrix by row-major order as expressed by:

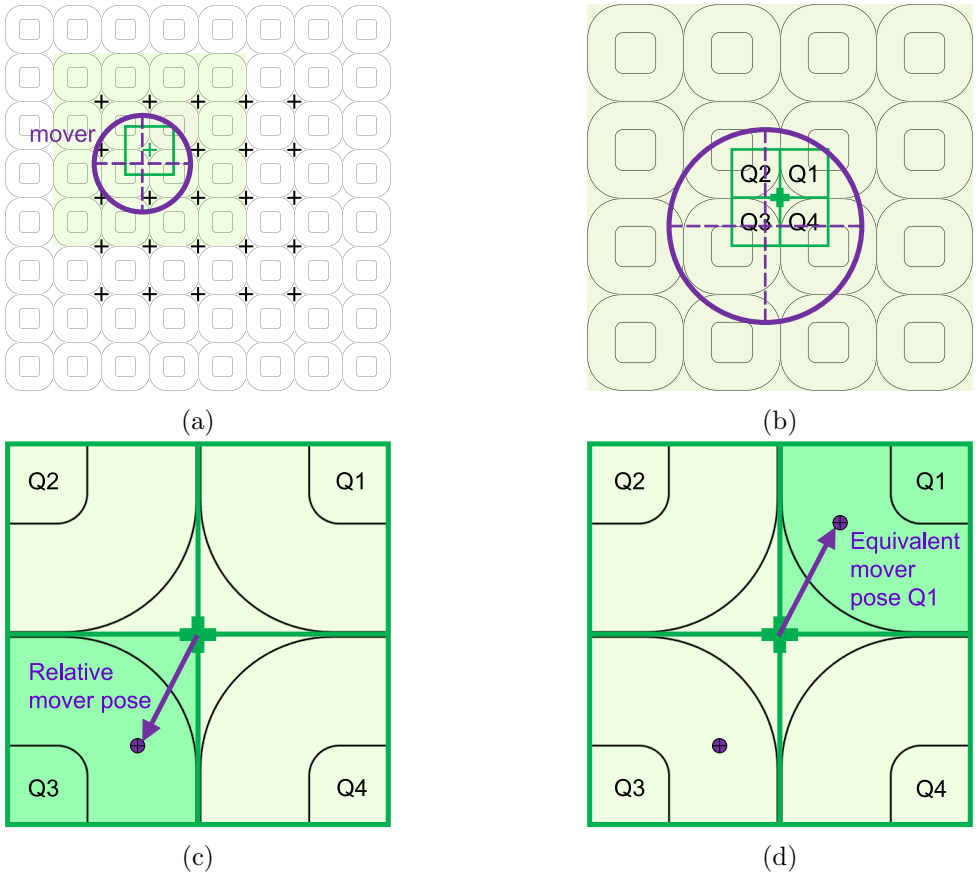


Figure 3.8: Wrench–current decoupling strategy for long-range planar motion. **(a)** Find 4×4 active coils. **(b)** Find relative mover quadrant. **(c)** Find relative mover pose. **(d)** Find equivalent mover pose in Q1.

$$\boldsymbol{c}_{Qn} = \text{flatten}\left\{ \text{rotate}_{(-Qn\cdot 90^\circ)}\left(\begin{bmatrix} 1 & 2 & 3 & 4 \\ 5 & 6 & 7 & 8 \\ 9 & 10 & 11 & 12 \\ 13 & 14 & 15 & 16 \end{bmatrix} \right) \right\} \tag{3.33}$$

Once the estimated wrench matrix $\mathbf{K}_{Qn}$ is obtained, the estimated wrench–current decoupling matrix $\mathbf{K}_{Qn}^{+}$ can be computed by using Moore-Penrose pseudoinverse.

This section described the wrench–current decoupling strategy for the long-range planar motion of the planar maglev system using short-range lookup data. This method is further evaluated on the planar maglev system in long-range levitation experiments.

3.5 Summary

This chapter presented the magnetic levitation models of the Lorentz levitation system. Solutions to two computation challenges in magnetic flux density and the triple integral over the coil volume were presented. For magnetic flux density, the disc magnet was modeled using the magnetic nodes approach. Then, the volume integral was approximated into summations by the Gaussian quadrature technique.

For model implementation in real-time control, the lookup method is used to determine the decoupling matrix from pre-computed wrench matrices in data memory. Since lookup data is discrete, the levitation performance can deteriorate at no-data poses. Hence, multivariate linear interpolation is used to estimate the decoupling matrix.

For long-range motion, the decoupling strategy using short-range lookup data was proposed. The lookup data has the range of quarter coil area. The active coil set is selected from the mover location. Then, the wrench–current decoupling matrix is estimated from lookup data and relative mover pose.

Chapter 4

Planar Coil Array Stator

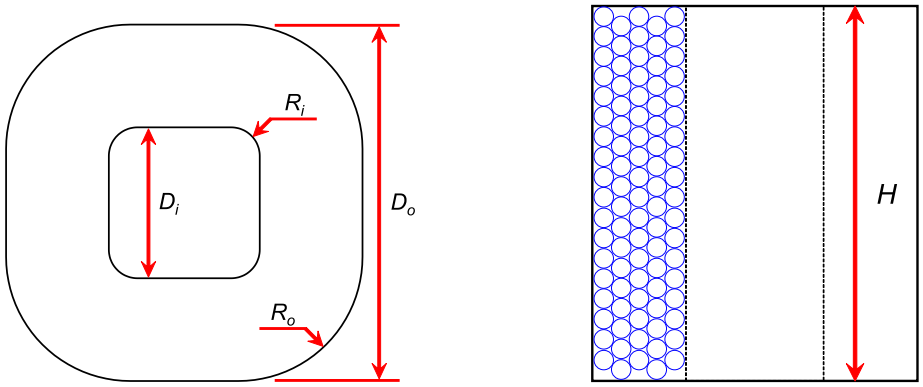
This chapter presents the design of the planar coil array stator. From the conceptual design, the process begins with the design of a square coil, coil array arrangement, and support structure. Two planar maglev prototypes, namely, the 10-coil testbed and MaglevFloor Prototype (Proto-MagFloor) are designed and built for pilot testing purposes. Next, the design of the Magnetic Levitation Floor (MaglevFloor) is detailed.

4.1 Electromagnets[1]

A comparison between square and cylindrical coils with comparable size in [91] indicated that an average magnetic flux density generated by an array of square coils was stronger than cylindrical coils. Hence, a square coil is preferable. To reduce the influence of magnetic hysteresis on the wrench model, the coil has an air core instead of ferromagnetic materials such as an iron core.

Figure 4.1 presents the top and side views of the round-corner square coil with inner radius R_i and outer radius R_o. There were three key dimensions to be designed in this work, the inner width D_i, the outer width D_o, and the height H. The coil was designed with the objective of this research to propose a compact and portable design of the planar maglev system. First, the inner width was obtained from the width of the coil bobbin spool. The bobbin spool was made of a 31.75 mm (1-1/4-inch) aluminum square tube welded on a 76.2 mm (3-inch) aluminum square base flange. The advantages of using the

[1]The design of electromagnets is collaborative work with Dr. Xiaodong Zhang, Maglev Microrobotics Laboratory, University of Waterloo. The work in this section was published in [93].



(a) (b)

Figure 4.1: Round-corner square coil with key dimensions. **(a)** Top view. **(b)** Side view.

hollow aluminum bobbin are a good machinability, an efficient heat dissipation from the coil, and a slight influence on the magnetic field generated by the coil.

Next, the outer width was determined by the thickness of the winding. The winding was assumed to be evenly distributed with the orthocyclic winding pattern as shown in Fig. 4.1b, which ideally provides an optimal fill factor of 90.7% [82]. An insulated magnet wire gauge of 16 AWG with a diameter d of 1.31 mm was used to make the coils with a maximum current of 7 A. The winding thickness can be calculated from the magnet wire diameter and the number of radial layers but must not exceed the width of the bobbin base flange. By considering a 10% tolerance from the material dimension and winding process, the number of radial layers of 16 was selected. As a result, the total outer width of the coil was approximately 75 mm.

Since the inner and outer widths of the coil were decided, the height of the coil was designed to achieve optimal energy efficiency and levitation effort. In terms of energy use, the Fabry factor was used in this work. This factor considers the coil geometry to evaluate the efficiency in generating a magnetic field. Even though the factor was derived from the cylindrical coil, it was adopted in this initial design since the square coil in this work had a large corner radius which resembled a cylindrical coil. The Fabry factor G of the uniform current-density coil was expressed in [81] as

$$G_{(\alpha,\beta)} = \frac{1}{5}\sqrt{\frac{2\pi\beta}{\alpha^2-1}}\ln\left(\frac{\alpha+\sqrt{\alpha^2+\beta^2}}{1+\sqrt{1+\beta^2}}\right), \tag{4.1}$$

where $\alpha = D_o/D_i$ and $\beta = H/D_i$. From the designed outer and inner widths, the ratio

of the coil's outer-inner width was $\alpha = 2.36$. The remaining variable β depended on the height of the coil. With the designed α value, the best G value this design could achieve was 0.175, where $\beta = 1.59$. Therefore, the optimal coil height from the Fabry factor was 50.48 mm, which was equivalent to 35 vertical winding turns or 50.435 mm.

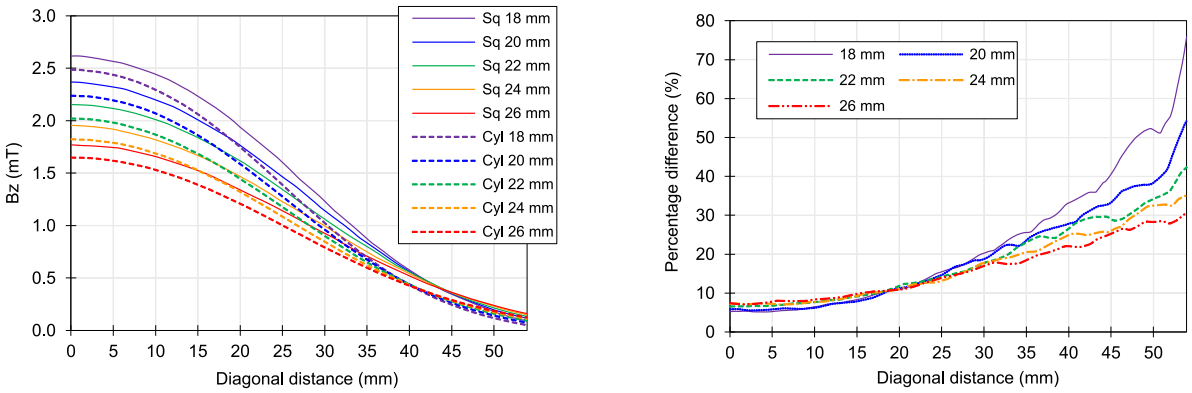
Simulations of a square and a cylindrical coil with coil parameters in Table 4.1 were conducted using finite element analysis software ANSYS Maxwell (see Appendix A.1). Both coils were comparable in size with the designed inner-outer widths and optimal height from the Fabry factor. The comparison of the z-component of the magnetic flux density B_z between the two coils is shown in Fig. 4.2a. The magnetic flux density is observed along the diagonal distance from center to corner at different levels from 18 mm to 26 mm above the coil top surface. The square coil could generate a stronger magnetic flux density than the cylindrical coil, especially at the corner, with higher percentage differences as shown in Fig. 4.2b. With an average difference of 18%, the height of the square coil was determined to attain at least 82% of the best achievable G value ($G \geq 0.144$). Accordingly, the range of β was $0.60 \leq \beta \leq 4.22$, and the range of the coil height was 19.05 mm $\leq H \leq$ 133.98 mm.

Another factor to be considered for the coil height optimization is the levitation effort. The vertical force was mainly considered in this design. To consider the Fabry factor and the vertical force together, the maximum height must be determined since the force continues to increase with the increment of the coil height or the number of vertical winding turns. With the optimal height and the range of the coil height from the previous step, the coil height was preferred to be higher than the optimal height to provide more force. Therefore, the range of coil height was increased from 50.48 mm to 133.98 mm. In other words, the range of the number of vertical winding turns was increased from 35 turns to 90 turns with an increment of 5 turns.

Table 4.1: Simulation (I): Magnetic flux density comparison between square and cylindrical coils.

Parameters		**Value**	**Unit**
Outer width	D_o	75.00	mm
Inner width	D_i	31.75	mm
Outer radius *	R_o	27.625	mm
Inner radius *	R_i	6.00	mm
Height	H	50.435	mm
Number of turns	N	560	turns

* For square coil.



(a) (b)

Figure 4.2: Magnetic flux density comparison between cylindrical and square coils along the diagonal distance from center to corner at different heights. **(a)** Magnetic flux density z-component B_z. **(b)** Percentage differences.

The parametric simulation of the force between a square coil and a single disc magnet was conducted in ANSYS Maxwell with the parameters in Table 4.2 (see Appendix A.2). The simulation model consisted of a disc magnet grade N50, a 101.60 mm (4-inch) diameter $\times$ 12.70 mm (1/2-inch) thickness, suspended with a 20 mm gap above the center of the square coil. The coil had inner and outer widths as designed. The coil height was a function of the number of vertical winding turns N_{vert}. The coil was supplied with a current of 1 A. Ideally, only the z-component of the force on the magnet can be observed whereas other force components are zero.

The normalized values of the Fabry factor and the vertical force are plotted in Fig. 4.3. From the plot, the optimal number of vertical winding turns was close to 60 turns or an estimated height of 86.50 mm. Hence, the number of vertical winding turns of 60 turns was selected. All designed parameters of the square coil are summarized in Table 4.3. An actual coil is shown in Fig. 4.4. The coil is wrapped with a fiberglass cloth tape. The top surface is covered by epoxy to prevent winding loosening.

Table 4.2: Simulation (II): Parametric simulation of the force between a square coil and a single-disc magnet.

Parameters		Value	Unit
Square coil			
Outer width	D_o	75.00	mm
Inner width	D_i	31.75	mm
Outer radius	R_o	27.625	mm
Inner radius	R_i	6.00	mm
Magnet wire diameter	d	1.31	mm
Vertical winding turns	N_{vert}	30 – 90	turns
Height	H	$d\,(N_{vert}) + 10\%$	mm
Disc magnet: 4-inch dia. × 1/2-inch thick NdFeB N50			
Diameter		101.6	mm
Thickness		12.7	mm
Remanence	B_r	1.45	T

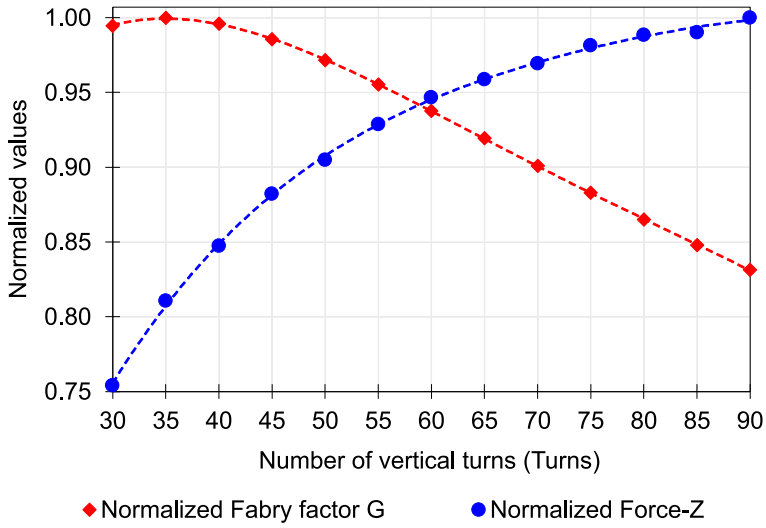


Figure 4.3: Normalized Fabry factor (red ♦) and normalized z-component of the force (blue ●) on a 4-inch diameter × 1/2-inch thickness disc magnet grade N50 with a 20 mm gap above the center of a square coil with different numbers of vertical turns.

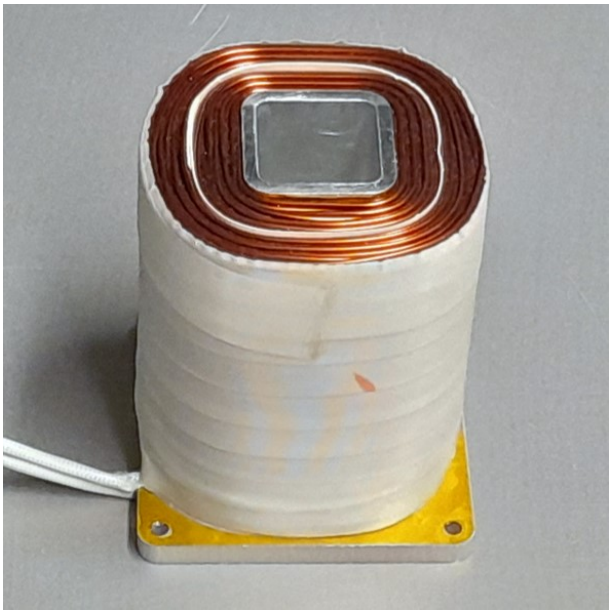


Figure 4.4: Actual square coil.

Table 4.3: Coil parameters

Parameters		**Value**	**Unit**
Outer coil width	D_o	75.00	mm
Inner coil width	D_i	31.75	mm
Height	H	86.50	mm
Wire gauge		16	AWG
Number of radial layer		16	layers
Number of vertical turns		60	turns
Total number of turns	N	960	layers
Resistance		2.6	Ohms
Inductance		17	mH
Weight		2.0	kg

4.2 Maglev System Prototype: 10-Coil Testbed[2]

Stator array configuration

After the square coil was designed, the arrangement of the planar coil array was considered. With a disc magnet mover, only five degrees of freedom can be controlled except for rotation about the vertical axis or yaw motion. The minimum number of coils to control the levitation of a single disc magnet is five as shown in [47]. For the planar maglev system, the surrounding coils were added to form the planar coil array. The planar coil array stator in this design initially had 9 coils arranged in a 3 by 3 array or straight configuration. The coil pitch or distance from center to center of the coil along the x and y axes was 76.2 mm (3 inches) to maximize the packing density of the array.

Two array configurations, namely straight and zigzag, were analyzed in this work. Both arrays had nine coils arranged with configuration parameters as detailed in Table 4.4 (see Appendix A.4). The zigzag array had a 38.1 mm (1-1/2-inch) offset for the middle row. The plots of the magnetic flux density at 20 mm above the two arrays are shown in Fig. 4.5. The significant difference between these two configurations can be observed at the corner between coils. The zigzag array could provide a better uniform magnetic flux density within the array than the straight array. In this work, the zigzag configuration was selected. An additional coil was added to the right side of the middle row for array symmetry.

Compact planar maglev system structure

Figure 4.6 represents an overview of the proposed compact planar maglev prototype with system specifications in Table 4.5. The overall dimensions of the planar stator module were 320 mm wide, 410 mm long, and 290 mm high, with a total weight of 36 kg. The top level was an array of ten coils arranged in the zigzag configuration as designed. The prototype was covered and surrounded by acrylic sheets for mechanical and electrical safety.

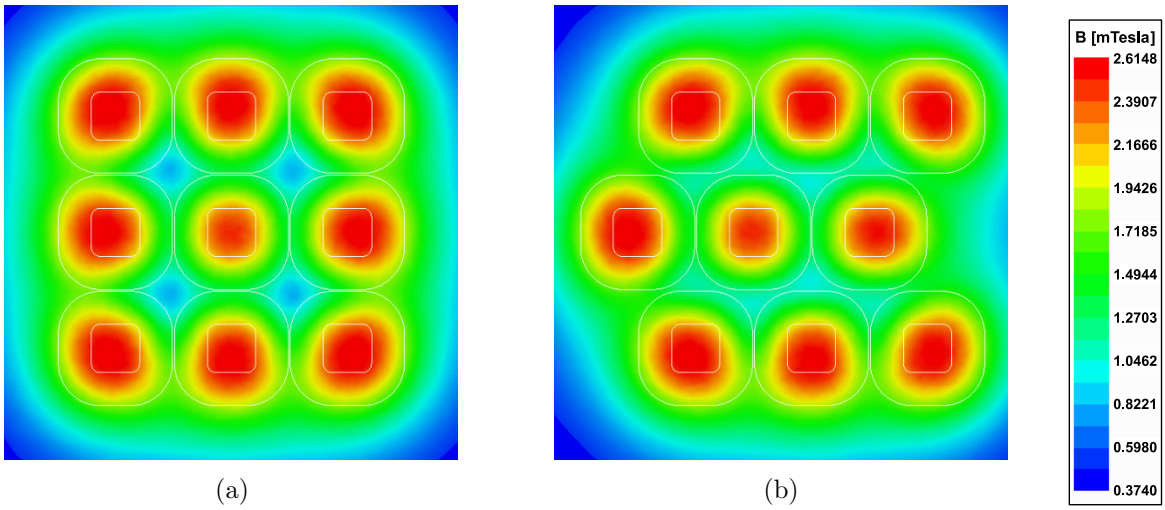
The bottom level had two current amplifier boards. Each amplifier board had five current amplifier units to control five coils individually. The current amplifier (AZB20A8, ADVANCED Motion Controls) received the ± 10 V analog current command signal from the controller with a supply voltage of 36 VDC.

[2]The design of the 10-Coil Testbed is collaborative work with Dr. Xiaodong Zhang, Maglev Microrobotics Laboratory, University of Waterloo. The work in this section was published in [93].

Table 4.4: Square coil array configuration parameters.

Parameters		Value	Unit
Square coil			
Outer width	D_o	75.00	mm
Inner width	D_i	31.75	mm
Outer radius	R_o	27.625	mm
Inner radius	R_i	6.00	mm
Height	H	86.50	mm
Number of turns	N	960.00	turns
Array configuration			
Coil pitch x (center-to-center)		76.20	mm
Coil pitch y (center-to-center)		76.20	mm
Row offset *		38.10	mm

* For zigzag configuration.



(a) (b)

Figure 4.5: Magnetic flux density on the area of 300 mm × 300 mm at 20 mm above the 9-coil array with **(a)** straight configuration, **(b)** zigzag configuration.

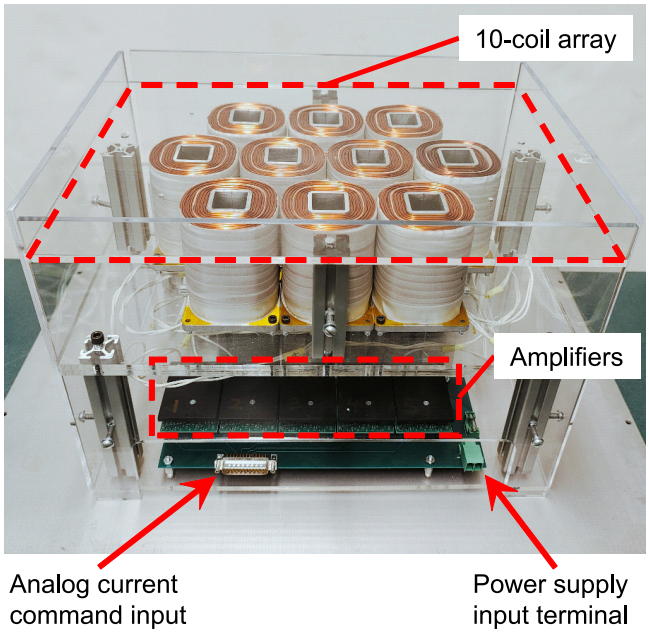


Figure 4.6: Compact planar maglev prototype structure.

Table 4.5: Compact planar maglev system specifications.

Parameters	Value	Unit
Overall dimensions and weight		
Width	320.00	mm
Length	410.00	mm
Height	290.00	mm
Weight	36.00	kg
Current amplifier unit		
Analog command signal	±10.00	V
DC supply voltage	36.00	V
Disc magnet: 4-inch dia. × 1/2-inch thick NdFeB N50		
Diameter	101.6	mm
Thickness	12.7	mm
Weight	900	g

4.3 Magnetic Levitation Floor and Prototype (Proto-MagFloor)

4.3.1 Conceptual Design

The Magnetic Levitation Floor (Maglev Floor or MagFloor) research was conducted by a research team from the Maglev Microrobotics Laboratory, at the University of Waterloo. The system is installed in the pit in the RoboHub.

The RoboHub pit has as-built dimensions of 2.0 m-width $\times$ 3.0 m-height $\times$ 1.0 m-depth as shown in Fig. 4.7. Due to the large size of the platform, most of the custom-made parts were mainly designed to be compatible with standard materials and components for budget efficiency.

For the heating, ventilation, and air conditioning (HVAC) system, fan coil cooling unit is provided at the bottom of the pit with the size of 4000 cubic feet per minute. There are four inlet and outlet ducts on both long sides. Air ducts are needed to deliver the cooling air from the bottom to the upper level.

Since the planar maglev system is installed on the hydraulic lift (capacity of 12000 lbs or 5.4 tons approx.), the system must provide enough space to access the bottom of the pit for maintenance. Therefore, a space of 30 cm is provided on both short sides for maintenance. As a result, the remaining area for the planar stator is 1.8 m by 2.4 m (6 ft by 8 ft).

For the conceptual design of the planar electromagnet array stator, the planar stator unit is intended to have a modular structure. Each unit is an integrated module which has coil array, electrical distribution system, and amplifiers. This design aims to provide system flexibility to expand or arranged in the desired area.

For the available pit area in a rectangular shape, the whole area is divided into eight sections. Each section has an area of 0.6 m by 0.9 m (2 ft by 3 ft). With the designed square coil in the previous section, the total number of coils in the section area is 96.

4.3.2 Coil Module

Instead of a square-shaped tile like the commercial products in the review, the coil module was designed to have a row-shaped frame. Each coil module has eight coils. For the coil module frame material, aluminum was selected since it does not affect the magnetic field generated by the coil array.

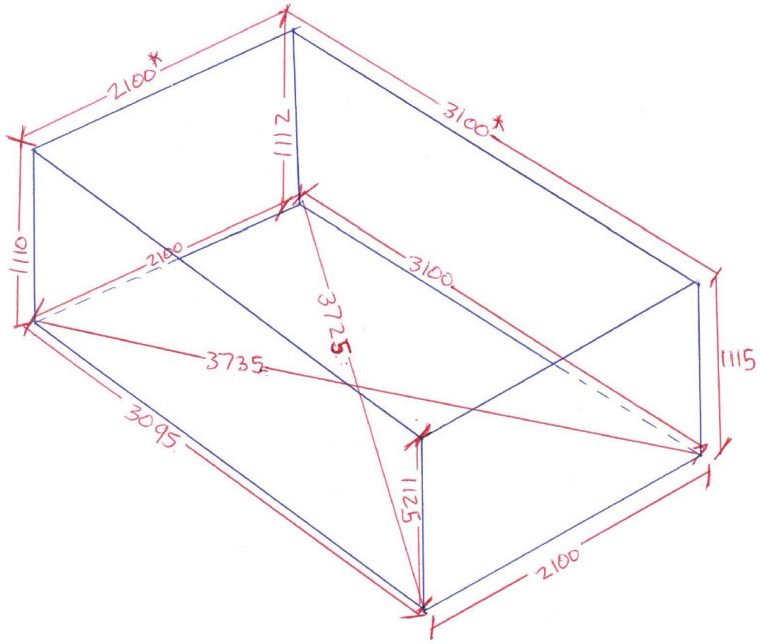


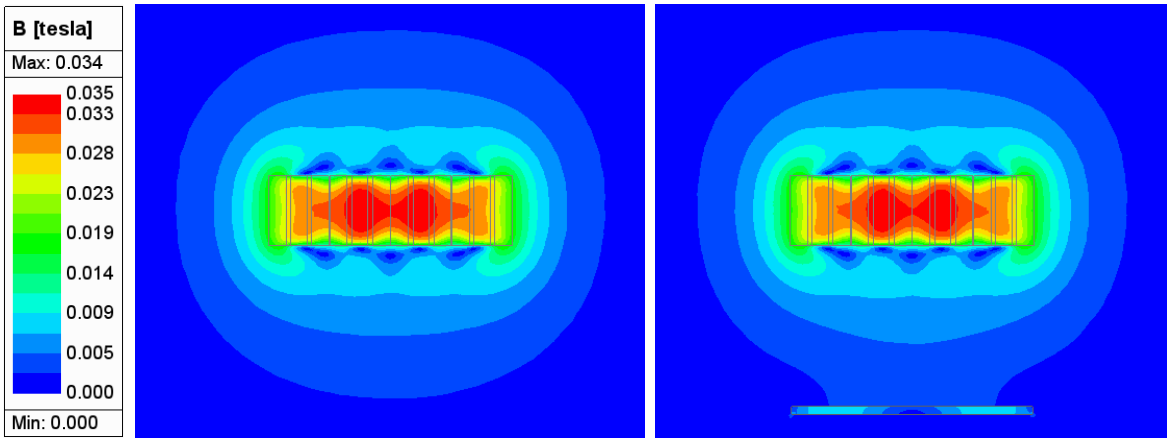
Figure 4.7: Waterloo RoboHub pit as-built with dimensions in millimeters.

However, the coil modules are installed on the steel support frame. Therefore, the height of the aluminum module frame must be optimized to minimize magnetic field interference by hysteresis from the steel support frame.

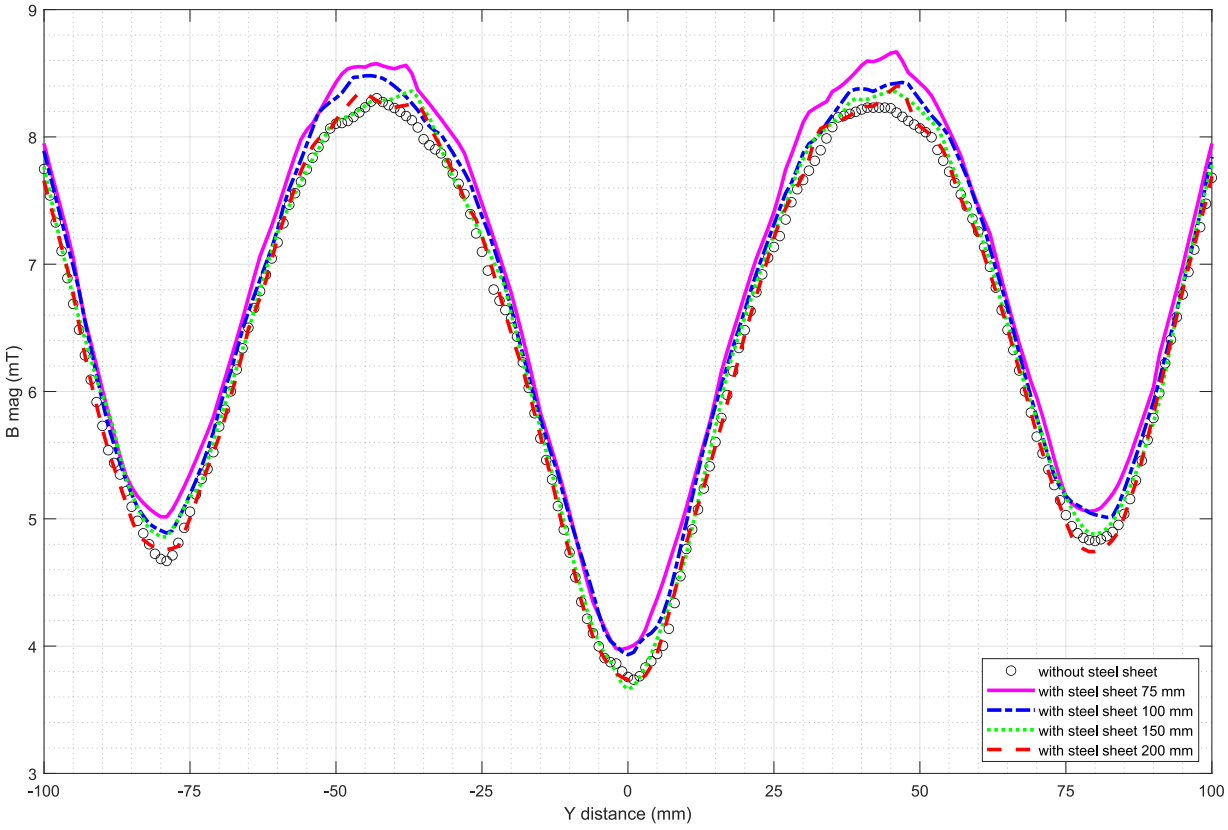
The simulation was conducted in the finite element analysis software, ANSYS Maxwell. To evaluate the interference of the steel table to the magnetic field generated by the coil, the model has a 4-by-4 coil array of the square coil which was designed in the previous section. A 10-mm thickness steel sheet was placed under the coil array at different distances.

The parametric simulation was conducted by varying the gap between the coil array and a steel sheet from 75 mm to 200 mm (see Appendix A.5). All coils were supplied with a 7 A current. A comparison of the magnetic field distribution between the array of 16 coils without/with the steel sheet at 200 mm under the coil array is shown in Fig. 4.8a.

The plot in Fig. 4.8b represents the magnetic flux density plot without/with the steel sheet at 75, 100, 150, and 200 mm under the coil array. By varying the gap between the coil array and the steel sheet, the closer gap results in stronger magnetic flux density. With a 75 mm gap, the maximum magnetic flux density difference compared to the result without the steel sheet is 8% approximately.



(a)



(b)

Figure 4.8: Magnetic field at 20 mm above the 4-by-4 coil array. **(a)** ANSYS simulation with and without steel sheet. **(b)** Magnetic field line plot from −100 mm to 100 mm along Y-axis.

From the simulation result, the magnitude of the magnetic flux density at 200 mm is similar to the result without the steel sheet. Therefore, the height of 200 mm (8 inches) for the coil module frame is selected. The design of the coil module is shown in Fig. 4.9.

The actual coil module is shown in Fig. 4.10. The weight of the module is 20 kg. Eight square coils are mounted on the top of the frame. The wires from each coil are routed to connect with the power connector at the bottom. Some coils are equipped with thermocouple type K to measure inside temperature and all outputs are connected to the panel. All coil modules were tested by supplying the same amount of current and checking the magnetic pole generated by each coil.

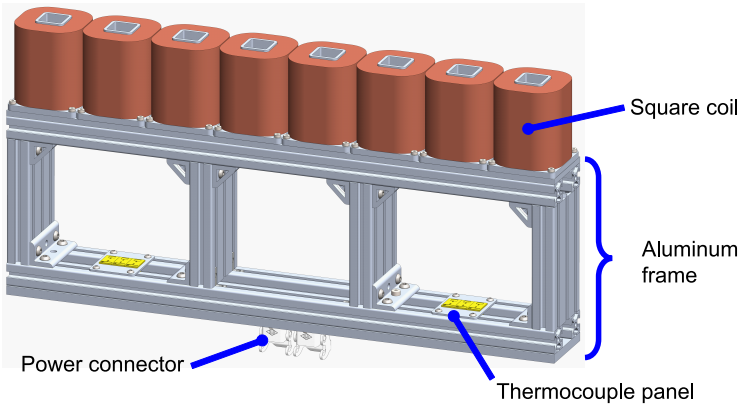


Figure 4.9: CAD model of the coil module.

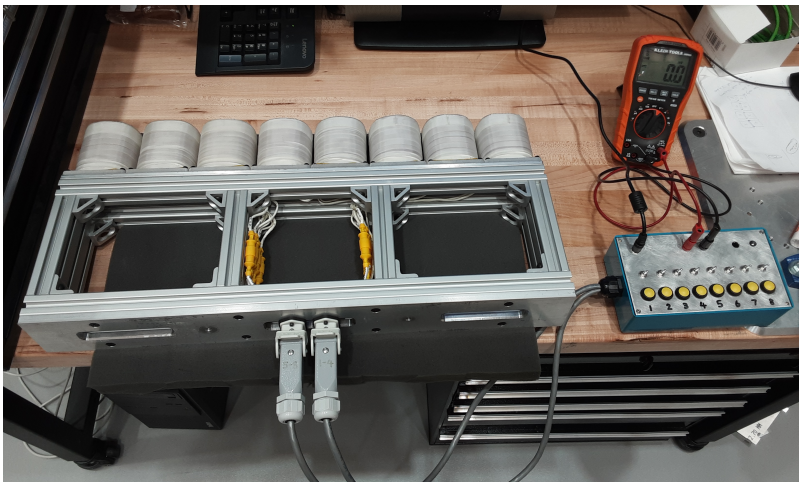


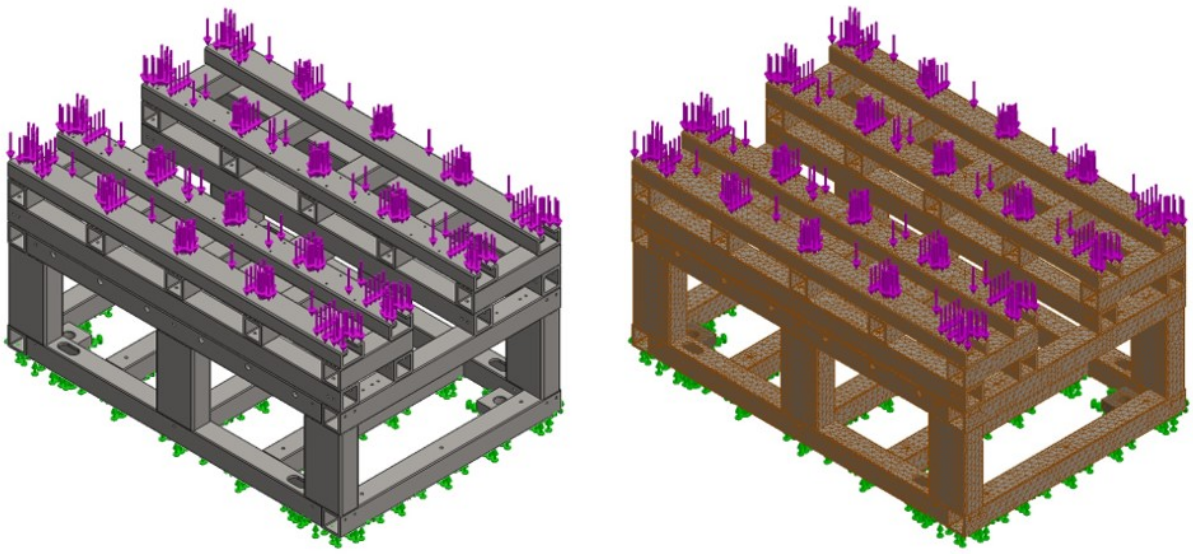
Figure 4.10: Actual coil module.

4.3.3 Modular Planar Stator Unit

After designing the coil module, the next component to be designed is the steel table. Since the total number of square coils per section area is 96 and each coil module has 8 coils, the steel table must hold the weight of 12 coil modules or 2400 N. The table also has an electrical distribution system and current amplifier installed inside the table.

The steel table consists of two parts: the welded frame and the level adjustment mechanism. The welded frame is the base of the modular planar stator unit. The electrical power distribution and amplifiers are installed inside this frame. The level adjustment mechanism can provide 3-D adjustment to align and level the coil array of this unit with other units.

To evaluate the strength of the designed table, the vertical force of 7200 N was applied on the top mounting of the table (see Appendix A.6). The force is evenly distributed on all four mounting bars. Figure 4.11 represent the simulation model setup in SolidWorks and the model mesh. The simulation results of von Mises stress and displacement or elongation are presented in Fig. 4.12. The designed table has the highest stress on three bars of the welded frame and the largest elongation at the middle of the table on two mounting bars.



(a) (b)

Figure 4.11: Stress analysis setup. **(a)** Vertical force 7200 N. **(b)** Model mesh.

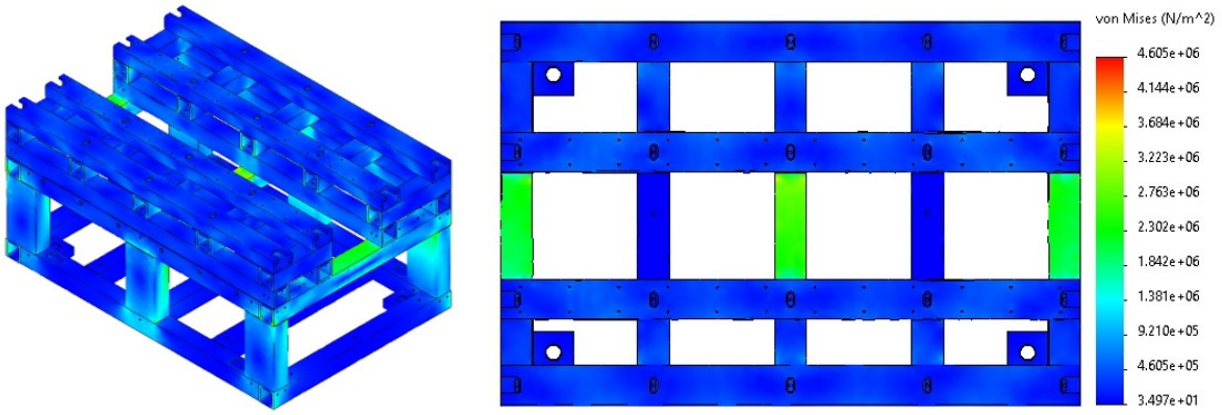


Figure 4.12: Stress analysis result: von Mises stress.

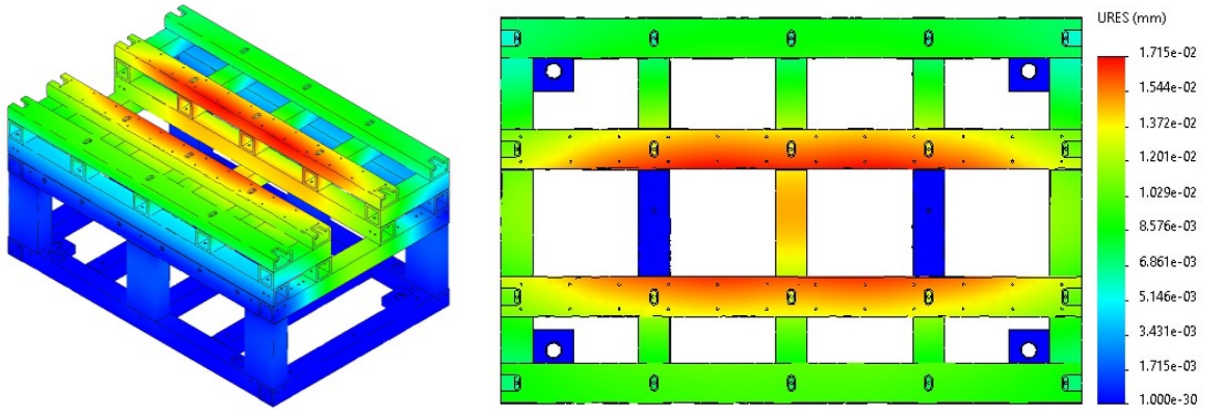


Figure 4.13: Stress analysis result: displacement.

4.3.4 Maglev System Prototype: Maglev Floor Prototype (Proto-MagFloor)

An overall design of the proposed system stator is represented in Fig. 4.14. The stator consists of an array of coil modules and a support structure.

The coil array comprises eight coil modules. Each coil module has eight square coils mounted on a module frame in rows with a 76.2 mm (3 inches) spacing between the centers of the coils as shown in Fig. 4.9. The air core square coils are made from 16 AWG insulated copper wire wound on a hollow aluminum bobbin.

The coil module frame is made from aluminum to reduce magnetic field absorption and hold the weight of eight coils. The square coils are wired to the power receptacle at the bottom of the module frame. By installing eight coil modules, the 64 electromagnets are arranged in an 8×8 square matrix array with a total horizontal levitation area of 600 mm $\times$ 600 mm, approximately.

The steel support structure contains two levels. The upper-level frame is for coil module mounting with level adjustment mechanisms, while the lower level is a rigid frame with a built-in amplifier module. The amplifier module has 32 amplifier units mounted on a copper plate installed in the support structure with insulated connections.

The amplifier unit with custom firmware is selected to power two coils independently. The amplifier units are supplied with 80 VDC for input supply and 24 VDC for logic supply. The amplifier output to the coil has a maximum of 80 VDC with a maximum current of 9 A for each coil. The details of internal current controller tuning were reported by Curtis [94]. EtherCAT is a protocol that provides high-speed communication and reduces wiring complexity between the controller and amplifiers in the system.

Figure 4.15 represents the system integration of the motion tracking system, modular maglev system, and control hardware. With the modular design of the electromagnet stator, the stator can be flexibly extended to fit in the desired area. The motion tracking system using cameras provides a large tracking area. The EtherCAT communication protocol reduces the wiring complexity between the controller and amplifiers. These features of the proposed system design enhance the flexibility of industrial applications.

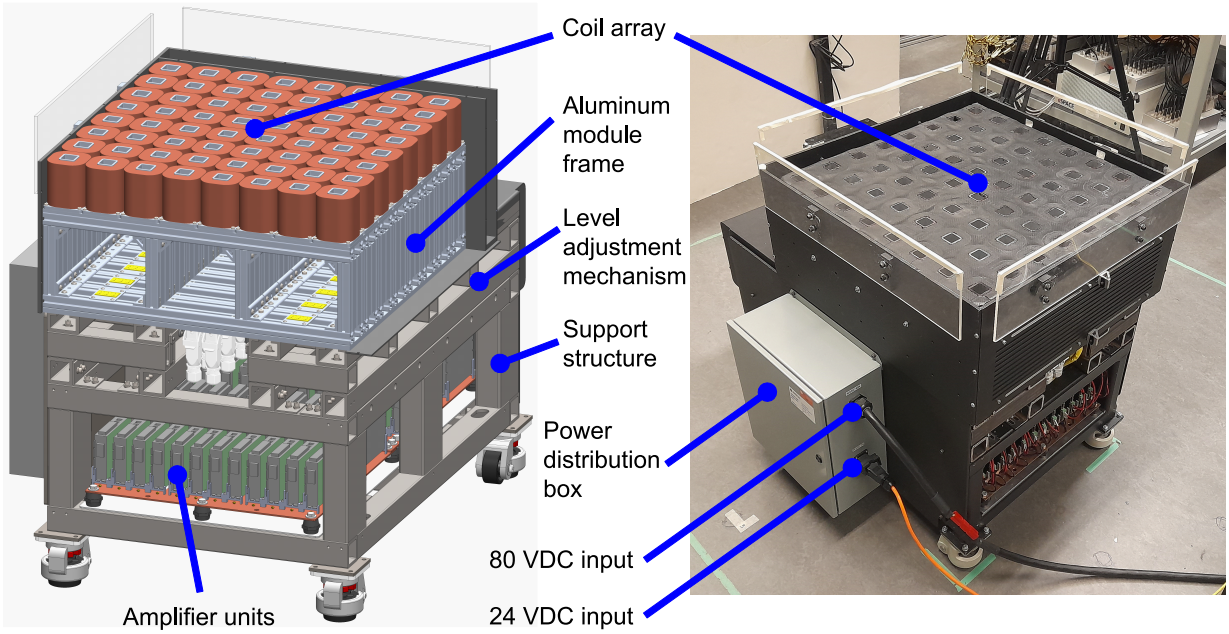


Figure 4.14: Maglev Floor Prototype (Proto-MagFloor). **(left)** CAD design. **(right)** Actual system.

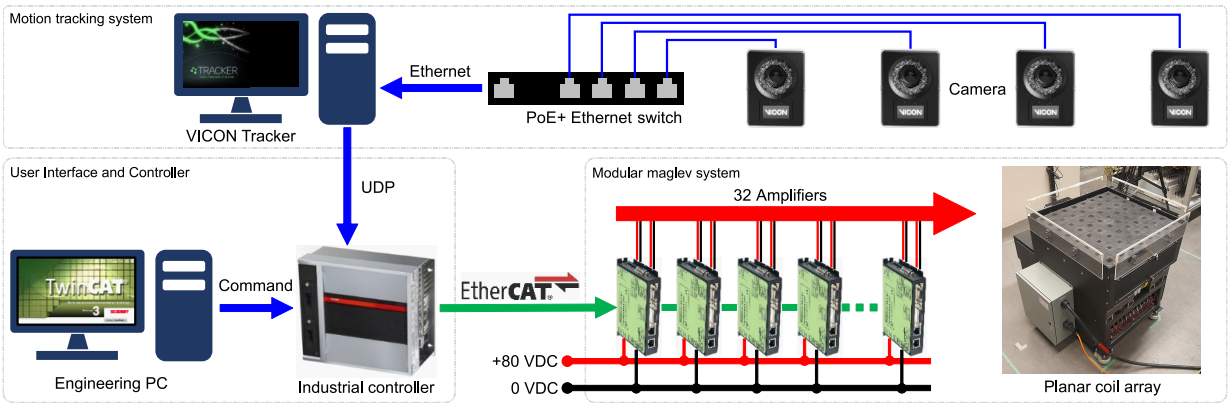


Figure 4.15: Proto-MagFloor: System diagram

4.3.5 Magnetic Levitation Floor

An overall design of the Magnetic Levitation Floor system is represented in Fig. 4.16 and the actual system in Fig. 4.17.

The stator comprises eight modular planar stator units. Each unit has 12 coil modules. Each coil module has eight square coils mounted on a module frame in rows with a 76.2 mm (3 inches) spacing between the centers of the coils as shown in Fig. 4.9. The air core square coils are made from 16 AWG insulated copper wire wound on a hollow aluminum bobbin.

The coil module frame is made from aluminum to reduce magnetic field absorption and hold the weight of eight coils. The square coils are wired to the power receptacle at the bottom of the module frame. By installing 12 coil modules, the 96 electromagnets are arranged in an 8×12 array with a total horizontal levitation area of 600 mm $\times$ 900 mm, approximately.

The steel support structure contains two levels. The upper-level frame is for coil module mounting with level adjustment mechanisms, while the lower level is a rigid frame with a built-in amplifier module. Each stator unit has 48 amplifier units mounted on a copper plate installed in the support structure with insulated connections.

The amplifier unit with custom firmware is selected to power two coils independently. The amplifier units are supplied with 80 VDC for input supply and 24 VDC for logic supply. The amplifier output to the coil has a maximum of 80 VDC with a maximum current of 9 A. For Maglev Floor system, there are four 5 kW power supply units (PSU) to supply 80 VDC electrical power to amplifiers and four 750 W PSUs for 2 VDC logic supply. Each PSU pair supplies electrical power to two stator units.

EtherCAT is a protocol that provides high-speed communication and reduces wiring complexity between the controller and amplifiers in the system. However, the EtherCAT communication of the Maglev Floor system differs from the Proto-MagFloor prototype because the command from the controller to 384 amplifiers is larger than the data package limitation of the EtherCAT and randomly causes data loss in communication. Hence, the amplifiers are separated into two groups. Each group connects to its dedicated EtherCAT.

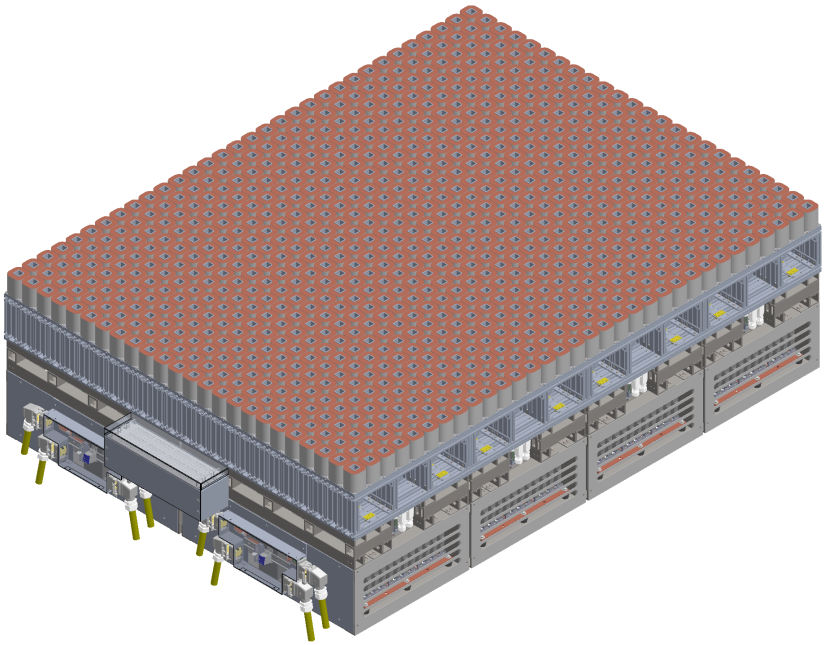


Figure 4.16: Magnetic Levitation Floor (Maglev Floor, MagFloor): CAD design

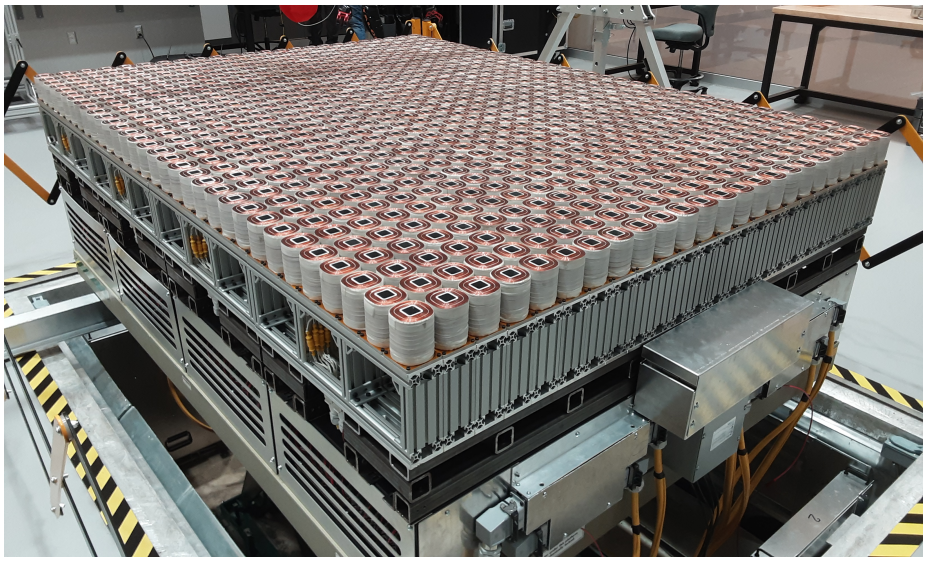


Figure 4.17: RoboHub Maglev Floor: Actual system

4.4 Summary

This chapter presents the development of three planar maglev systems in this research: 10-Coil Testbed, Maglev Floor Prototype (Proto-MagFloor), and Magnetic levitation floor (MaglevFloor). The design process begins with the square coil design. The dimensions of the coil are designed and optimized using the Fabry factor and the vertical force.

For the 10-coil Testbed, a comparison between two coil arrays: straight and zigzag configurations demonstrated the magnetic field distribution over the area. As a result, a zigzag configuration was selected and the compact system was built with 10 coils.

For the Proto-MagFloor, this prototype is the main testing unit for this research before implementation on the Maglev Floor system in RoboHub. This system only has eight coil modules, instead of 12 coil modules, arranged in an array of 8-by-8 with a straight configuration.

For the Magnetic Levitation Floor, the system has eight planar maglev units installed on a hydraulic lift in the pit in RoboHub. An internal electrical system is similar to the Proto-MagFloor system. With modular design, this system has the capacity to enhance modern smart manufacturing.

Chapter 5

Disc-Magnet Mover

This chapter presents an analysis and design of permanent magnet movers using disc magnets. Magnet movers range from a single disc magnet with a 5-DOF motion to multiple disc magnets with a 6-DOF motion. For the wrench matrix used for analyses in this chapter, the force components are in N unit and the torque components are in N·cm unit.

5.1 Single-Disc Magnet Mover

For a single-disc magnet mover, Neodymium disc magnet grade N52 with three different diameters: 2-inch, 3-inch, and 4-inch, were selected to be analyzed in this work. All disc magnets have the same thickness of 12.70 mm (1/2 inches).

In this section, the wrench matrices for each magnet on the area of 38 mm $\times$ 38 mm of the 4-by-4 square coil array as designed in the previous chapter with a 20 mm levitation gap (26.35 mm) are computed. The condition number of the wrench matrices represents the controllability of the magnet as reviewed in Chapter 2.

The condition number plots of three magnets are presented in Fig. 5.1. The maximum, minimum, and average values are shown in Table 5.1. The analysis results indicate that the poses with a lower condition number have better controllability when the magnet has a comparable or larger diameter compared to the coil width.

Figure 5.2 represents the 4-inch magnet mover with a 101.60 mm diameter $\times$ 12.70 mm thickness (4 inches $\times$ 1/2 inches) Neodymium disc magnet grade N50. The magnet is mounted to the acrylic frame equipped with reflective markers on the top with different heights for motion tracking. The total weight of the mover is approximately 900 g.

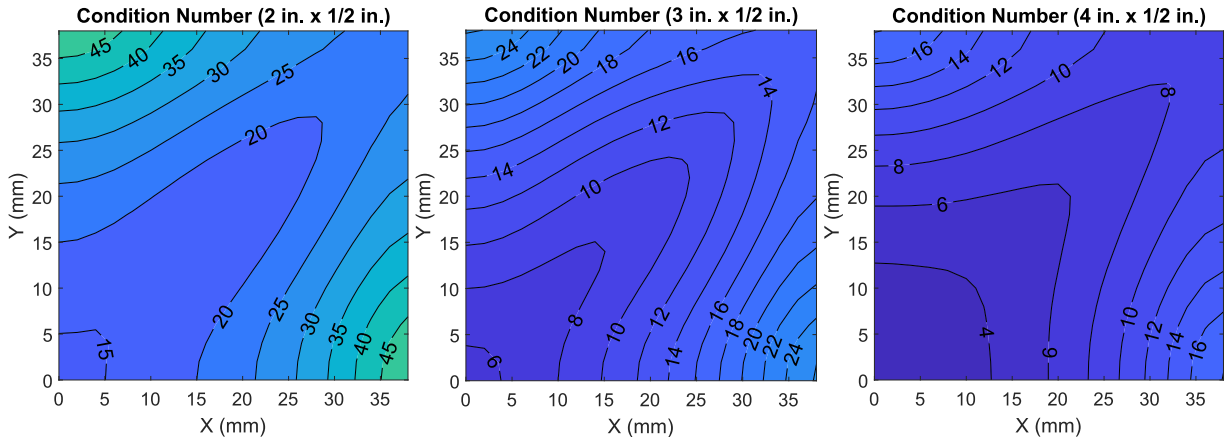


Figure 5.1: Condition number plot of wrench matrices between 2-inch, 3-inch, and 4-inch diameter and 1/2-inch thickness disc magnets grade N52 and 3-inch square coil with 20 mm levitation gap.

Table 5.1: Condition number comparison between 2-inch, 3-inch, and 4-inch Neodymium disc magnets grade N52 with 20 mm levitation gap.

Magnet size (Diameter × Thickness)	Condition Number		
	Max	Min	Average
2 in. × 1/2 in.	49.32	13.84	26.36
3 in. × 1/2 in.	26.20	5.36	14.49
4 in. × 1/2 in.	18.07	2.26	8.81

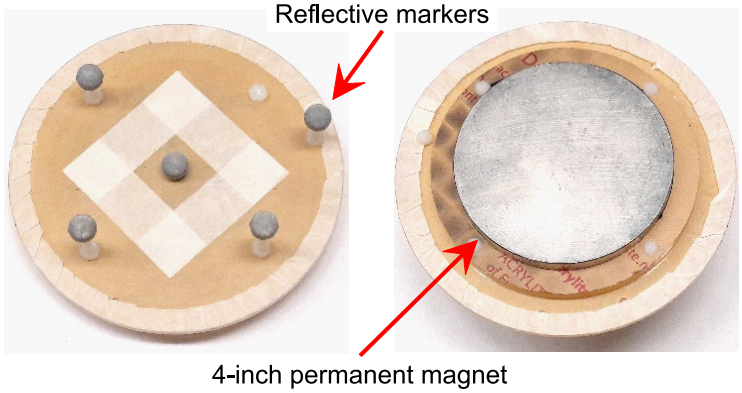


Figure 5.2: Single 4-inch disc magnet mover

5.2 Multiple-Disc Magnet Mover

For a multiple-disc magnet mover, for safety, four 2-inch diameter $\times$ 1/2-inch thickness Neodymium disc magnet grade N52 are selected to build a mover. Then, the layout of the disc magnets must be analyzed and optimized.

For layout optimization, the maximum size of the mover is limited to 200 mm which is based on typical mover size from commercial products. The magnet layout distance R as shown in Fig. 5.3 is optimized in this work. The range of R is from 40 mm to 95 mm.

Similar to a single-disc magnet, three indices: condition number, maximum current, and total power consumption, are used. The wrench–current matrices for each magnet on the area of 38 mm $\times$ 38 mm of the 4-by-4 square coil array as designed in the previous chapter with a 20 mm levitation gap (26.35 mm) are computed. For maximum current and total power consumption, the vertical force of 15 N is used for computation.

Figures 5.4 to 5.6 represent the plots of condition number, maximum current, and total power consumption map respectively. The max-min-average values from each plot are compared in Fig. 5.7. Since most of the maximum current plot except $R = 40$ mm in Fig. 5.5 is larger than the current limit of 9 A, the magnet layout with $R = 40$ mm is selected. This design also provides a low condition number and total power consumption compared to other R.

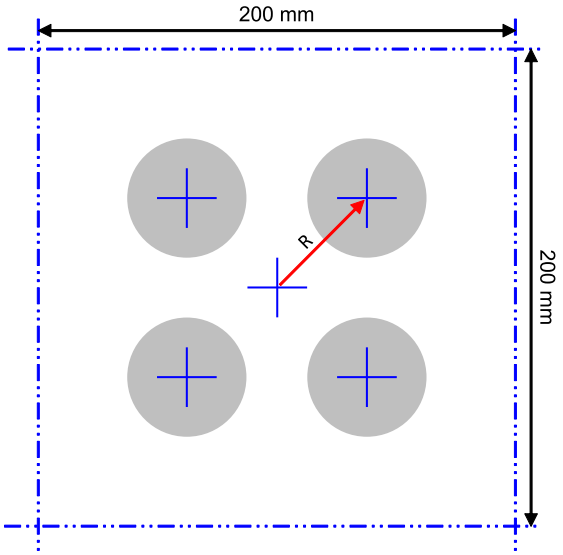


Figure 5.3: Four-disc magnet layout

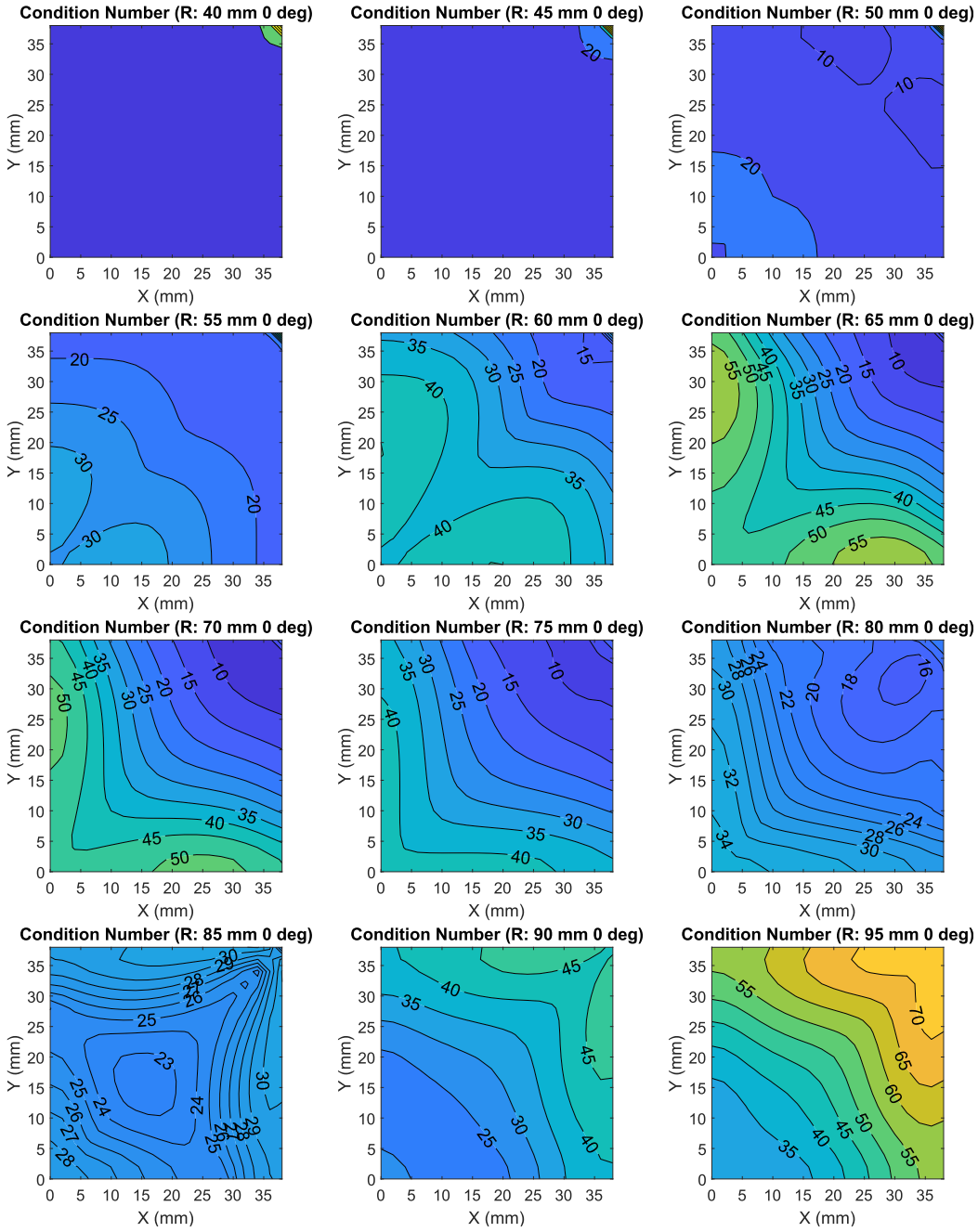


Figure 5.4: Four disc magnet analysis: Condition number map at 20 mm gap with various R.

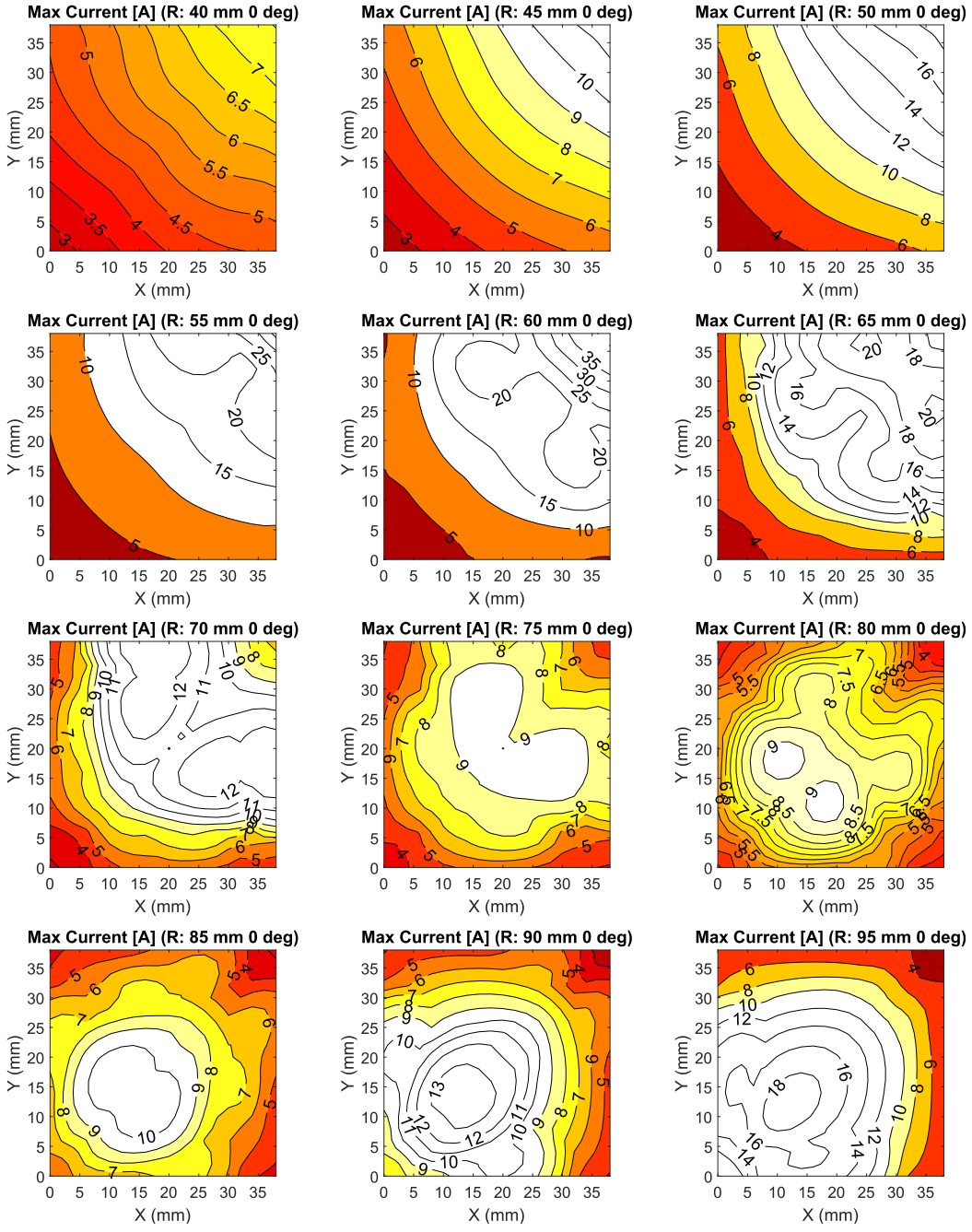


Figure 5.5: Four disc magnet analysis: Max current map at 20 mm gap with various R and vertical force 15 N.

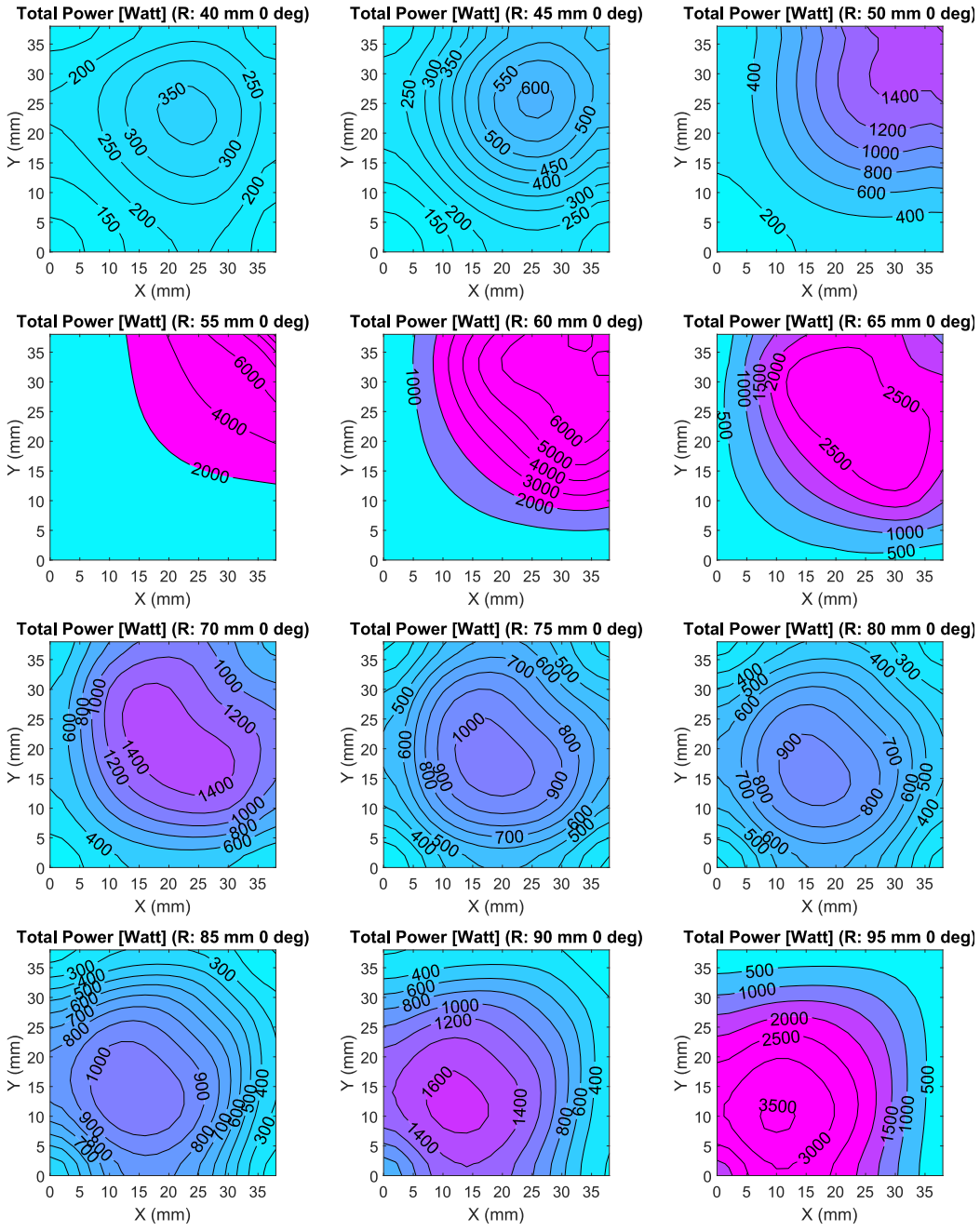


Figure 5.6: Four disc magnet analysis: Total power consumption map at 20 mm gap with various R and vertical force 15 N.

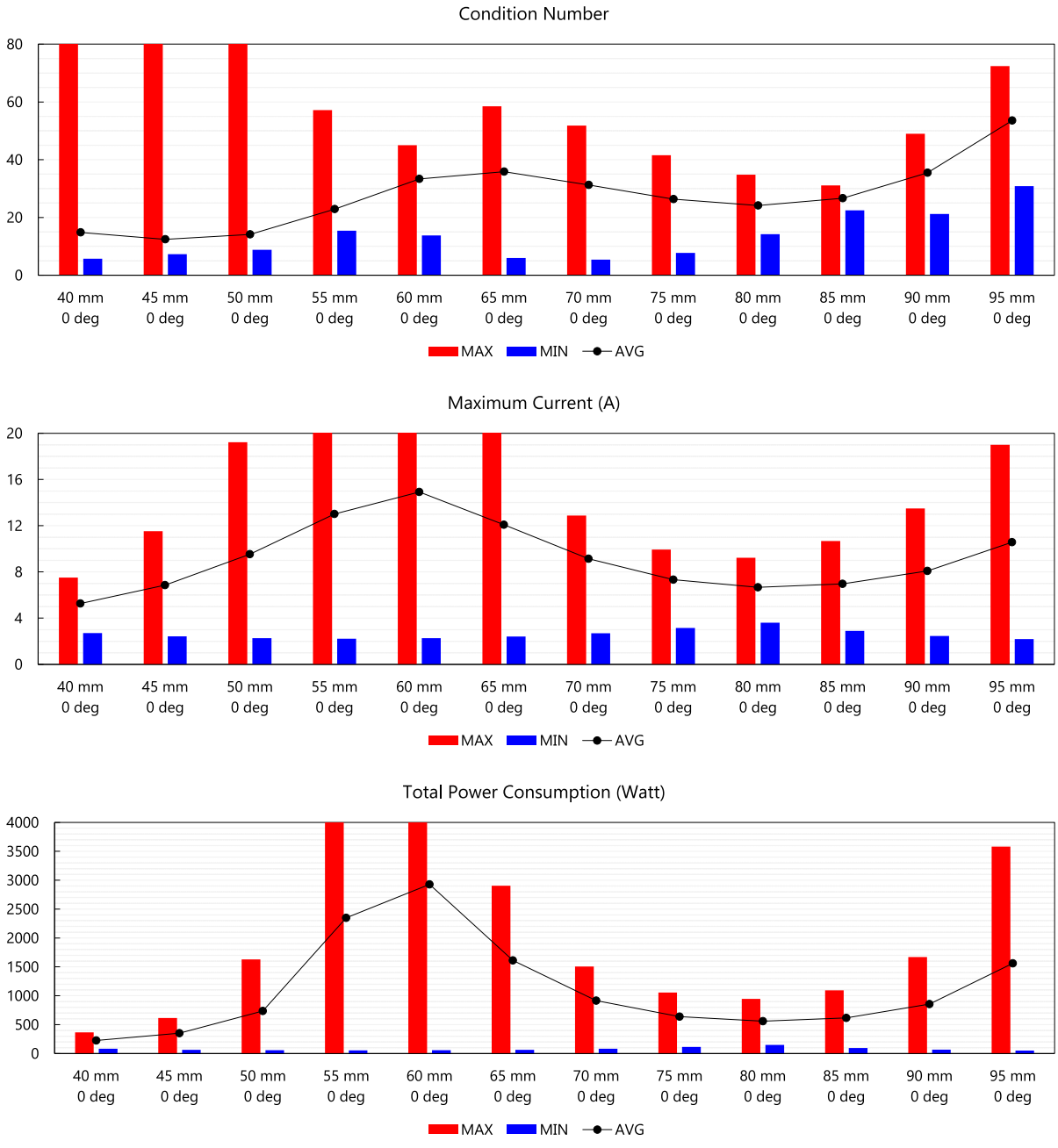


Figure 5.7: Four disc magnet analysis: Overall analyzed maximum-minimum-average values at 20 mm gap with various R and vertical force 15 N.

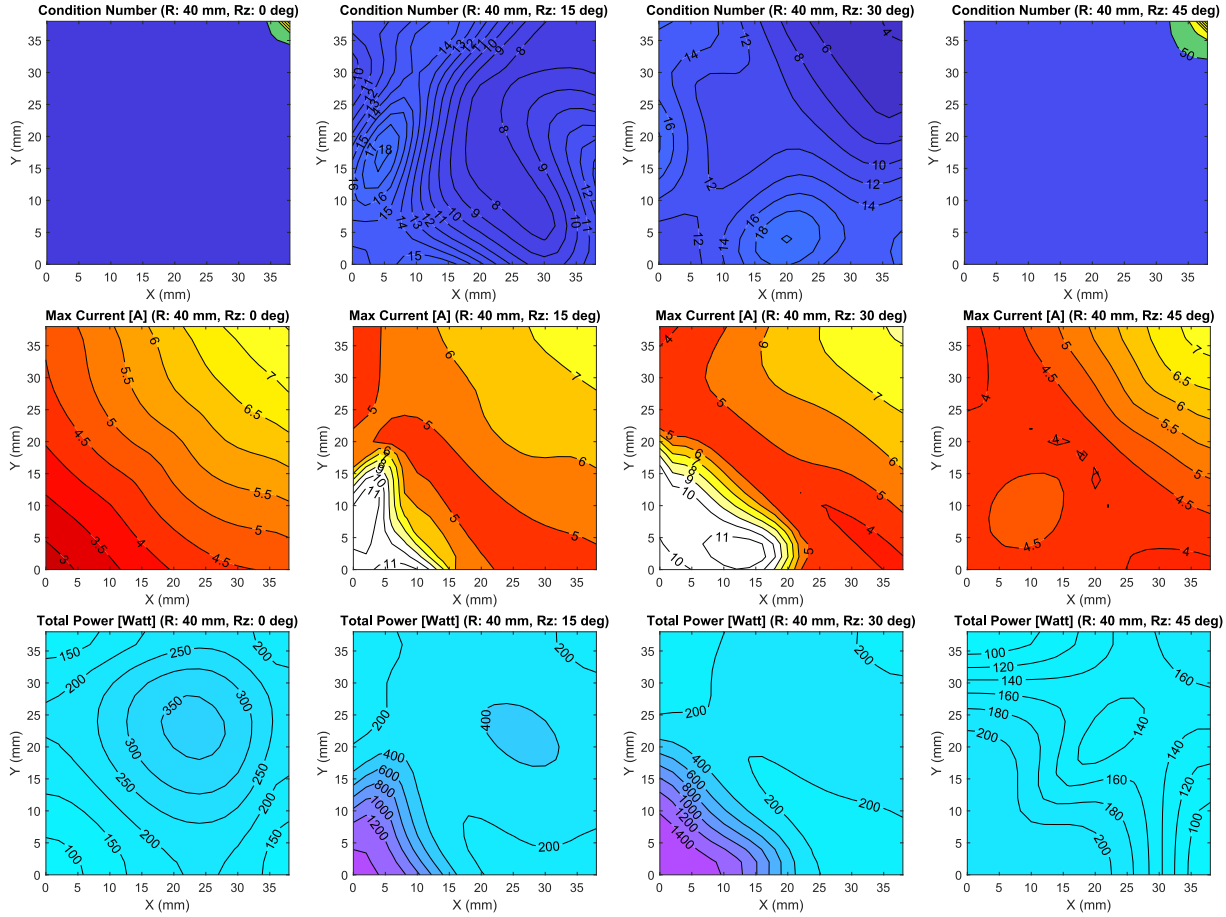


Figure 5.8: Four disc magnet analysis: Condition number, maximum current, and total power consumption map at 20 mm gap and vertical force 15 N with $R = 40$ mm and various yaw angles.

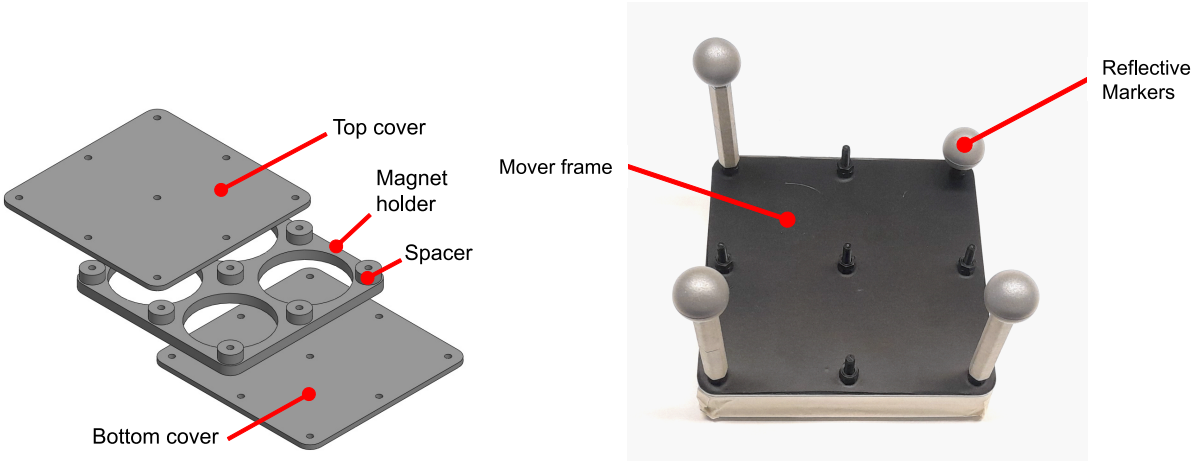
Since the multiple-disc magnet mover can have yaw motion, an analysis of the mover with various yaw angles was conducted. The wrench matrices on the same area were computed. The mover has 20 mm gap above the array. It has different yaw angles from 0 degree to 45 degrees with an increment step of 15 degrees. The vertical force is 15 N. Then, the condition number, maximum current, and total power consumption maps can be obtained as shown in Fig. 5.8.

First, the plots of 0- and 45-degree yaw angles are similar. A high condition number can be observed at the top-right corner of the plot. This corner represents the center of the coil in the first quadrant. Accordingly, the maximum current required in this region is high at 7 A. The maximum total power consumption is 350 W.

A critical problem can be found in the plots of 15- and 30-degree yaw angles. The system requires a very high current at the lower-left corner of the map which is the center of the 4-by-4 coil array. These required current values are larger than the maximum supplied current of 9 A for each coil. The condition number values in this central region of the array are larger than the coil-center region which still requires a high current of 7 A. The total power consumption values are extremely high up to 1.4 kW.

Overall, these analyses represent the correlation between condition number, maximum current, and power consumption. With static levitation and load settings, the system already requires high current in some regions. Moreover, mover motions need more force and torque. This may result in higher current which will be saturated by current limit and affect levitation stability. Hence, the levitation should consider efficient location, especially the yaw rotation.

Figures 5.9a and 5.9b depicts the CAD designed and actual four-disc magnet mover. The mover frame is made from acrylic. The reflective markers are used for motion tracking. Three markers are mounted on the standoffs at the same height for coordinate setup in motion tracking software. An additional marker is mounted at the different height to avoid redundancy in mover pose detection. The mover weight is 990 g.



(a) (b)

Figure 5.9: Four-disc magnet mover. **(a)** CAD model. **(b)** Actual mover.

Table 5.2: Mass properties of the designed movers.

Movers	Mass (kg)	I_x (kg·m^2)	I_y (kg·m^2)	I_z (kg·m^2)
Single 4-inch PM	0.90	0.0006	0.0006	0.0012
Four 2-inch PM	0.99	0.0012	0.0012	0.0024

5.3 Summary

This chapter presented the design and analysis of the disc-magnet mover. For a single-disc magnet, 2-inch, 3-inch, and 4-inch diameter disc magnets with the same thickness were evaluated. From condition number analysis, the condition number tends to be lower when the disc magnet has larger diameters compared to the coil width. Hence, a 4-inch disc magnet was selected. The mover can only be controlled for 5-DOF without yaw rotation.

Next, the mover with multiple-disc magnets was designed to achieve 6-DOF motion. The mover comprises four 2-inch disc magnets. For magnet layout optimization, condition number, maximum current, and total power consumption were used in this analysis. From analysis, the magnet layout with $R = 40$ mm was selected. Further analysis with different yaw rotations indicates that the mover consumes high current when levitates with a yaw angle at the center of the 4-by-4 coil array. Both movers equip reflective markers for motion tracking. The mass properties of both movers are summarized in Table 5.2.

Part II

System Implementation

Chapter 6

Implementation on 10-Coil Testbed[1]

This chapter presents the implementation and levitation experiment results on the planar maglev prototype, 10-coil Testbed, with a single 4-inch magnet mover. First, a decoupling problem with discrete lookup data is evaluated. Then, the 2-DOF linear interpolation is implemented to solve the problem. Next, the levitation experiments within the lookup data are conducted in both translation and rotation.

6.1 10-Coil Testbed System Setup

6.1.1 System Setup

Figure 6.1 represents the overall setup of the proposed planar maglev system with the motion tracking system and controller. The motion tracking system has four cameras (VICON Vantage V5) to detect the reflective markers on the mover. Then, the data is transmitted over the Ethernet to the software to compute the mover position and orientation. With proper calibration, the motion tracking system can provide position and orientation data with ± 10 μm and ± 0.2 mrad resolution with an update frequency of 1 kHz to the controller via UDP protocol. With the same sampling frequency of 1 kHz, the controller (NI PXI-8820) operates with the implemented control algorithms as described in the previous section to determine the coil currents. The analog current command outputs are sent out through two analog output modules to the current amplifiers in the planar maglev system.

[1]Implementation on the 10-Coil Testbed is collaborative work with Yang Wang, Maglev Microrobotics Laboratory, University of Waterloo. The work in this chapter was published in [93].

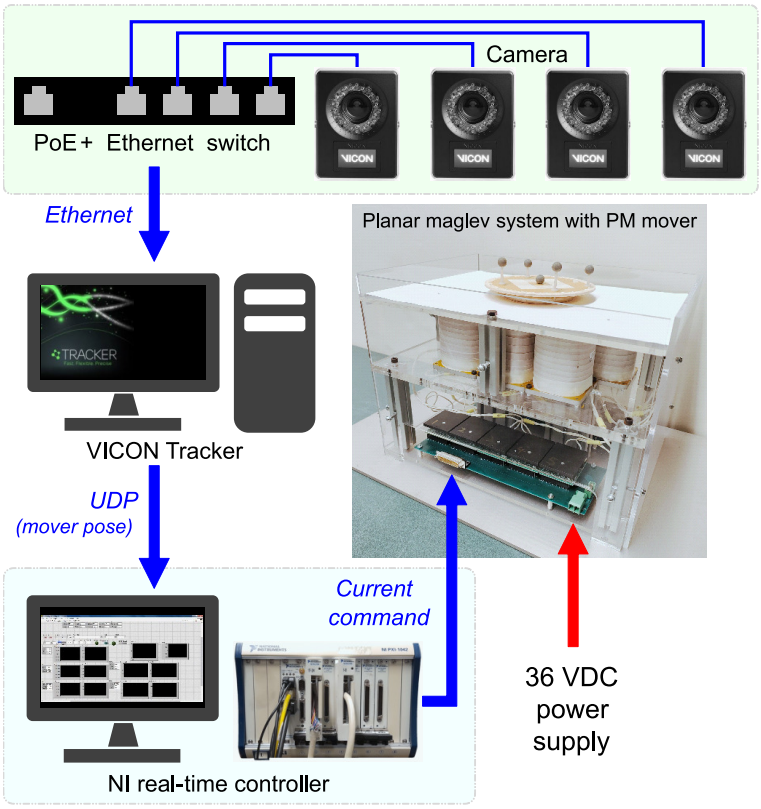


Figure 6.1: 10-Coil Testbed: Overall system setup.

6.1.2 Lookup Table

Since the wrench-current decoupling matrix is a function of the mover pose, the real-time solution of this matrix must be computed for every control sampling. However, with the numerical computation solution to the Lorentz forces and torque, this method cannot be implemented in real-time control. Hence, in this work, the decoupling matrices within a specific range of motion were pre-computed and stored in the lookup table.

To keep the size of the lookup table reasonable while providing sufficient information for the operational space, the 5-D table with a 1 mm grid on both x and y axes from -10 mm to 10 mm, 1 mm grid on z axis from 18 mm to 26 mm, and 5 degrees grid on both ψ and θ axes from -10 degrees to 10 degrees are created. The closest matrix to the mover pose will be returned while searching the lookup table during runtime. This lookup table approach helps with reducing the computation cost by sacrificing the controller memory. Only a

Table 6.1: 10-Coil Testbed: 5-DOF lookup data range for a single-disc magnet mover.

DOF	Min value	Increment	Max value
Translation (mm)			
X	−10.0	1.0	10.0
Y	−10.0	1.0	10.0
Z	18.0	1.0	26.0
Rotation (deg)			
Roll ψ	−10.0	5.0	10.0
Pitch θ	−10.0	5.0	10.0

finite number of mover poses are stored. Therefore, it is inevitable to use the lookup result when the mover location is out of the lookup data. By applying the multi-dimensional linear interpolation approach, the decoupling matrix can be estimated for the desired pose instead of using the nearest data.

6.1.3 Multivariate Linear Interpolation

To enhance the decoupling performance, a multivariate linear interpolation was implemented in this experiment to solve the data switching problem. For a single-disc magnet mover, the maximum controllable degree of freedom is 5-DOF.

The 5-DOF linear interpolation can be formulated by determining the related indices from the mover pose: (x_0, y_0, z_0, ψ_0, θ_0). The decoupling matrices are looked up using 5 state pairs (x_1, x_2), (y_1, y_2), (z_1, z_2), (ψ_1, ψ_2), and (θ_1, θ_2). For 5-DOF linear interpolation, there are 32 matrices to be searched for estimation.

However, only a 2-DOF linear interpolation was implemented with two combinations of x–y and ψ–θ axes separately due to controller constraints.

6.1.4 Control System

An overall 5-DOF control diagram is illustrated in Fig. 6.2. By using the decoupling matrix $\mathbf{K}^+$, the cross-coupling effect can be decoupled and 5-DOF PID control can be applied to control each degree of freedom separately. The pre-computed decoupling matrices are stored in the lookup table. The matrix can be looked up by using the moving pose obtained from the motion tracking system. An additional gravity compensator is used to compensate the mover weight in a vertical motion.

The tuned PID parameters for the proposed system are shown in Table 6.2. It is worth noting that the PID parameters are different on x and y axes. Similarly, the parameters are different on ψ and θ axes. Due to the zigzag configuration of the ten coils we used for our experiments, asymmetry coil control effort along horizontal axes is expected. Therefore, the tuned parameters are different on axes. The units of the PID gains are selected as SI units. For rotations, due to the difficulty of the system to generate large torques, the gains are in relatively small quantities with SI units.

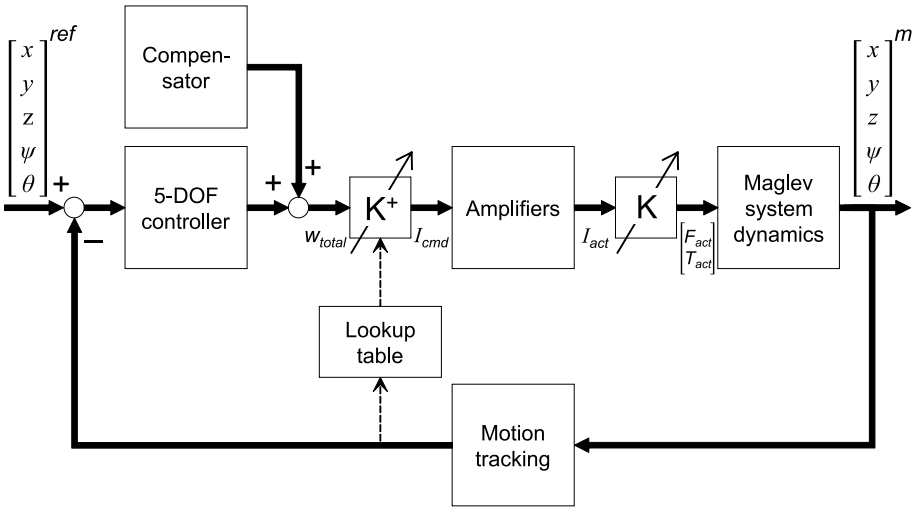


Figure 6.2: 10-Coil Testbed: 5-DOF PID control diagram

Table 6.2: 10-Coil Testbed: 5-DOF PID controller parameters.

DOF	PID controller					
	P gain		I gain		D gain	
X	1500	N/m	6500	N/m·s	55	N·s/m
Y	600	N/m	3000	N/m·s	36	N·s/m
Z	900	N/m	5000	N/m·s	40	N·s/m
Roll	1	N·m/rad	3.33	N·m/rad·s	0.06	N·m·s/rad
Pitch	1.5	N·m/rad	5	N·m/rad·s	0.09	N·m·s/rad

6.2 Experiment Results on 10-Coil Testbed

6.2.1 Linear Interpolation Performance Verification

The PID parameters in Table 6.2 have been used to verify the performance improvement between with and without the linear interpolations, on both combinations of x - y and ψ - θ axes. In Fig. 6.3, the ψ - θ axes linear interpolation is able to eliminate the sharp oscillation effect when switching wrench matrices in the lookup table. Because the grid size of the lookup table on ψ - θ axes is 5 degrees, larger error gaps are expected at the switching location.

On x - y axes, step response at the wrench matrix switching location shows that constant oscillations exist. There are smaller oscillations on the x axis than on the y axis, due to the coil layout configurations. The x - y axes linear interpolation is able to reduce the additional source of oscillations caused by the uncontrollable yaw rotation effect on x - y oscillations and x - y step responses, as shown in Fig. 6.4 and Fig. 6.5.

To smooth out the overall errors, applying linear interpolation is one of the approaches to achieving so. The results show that the control performances are improved with no further tuning needed.

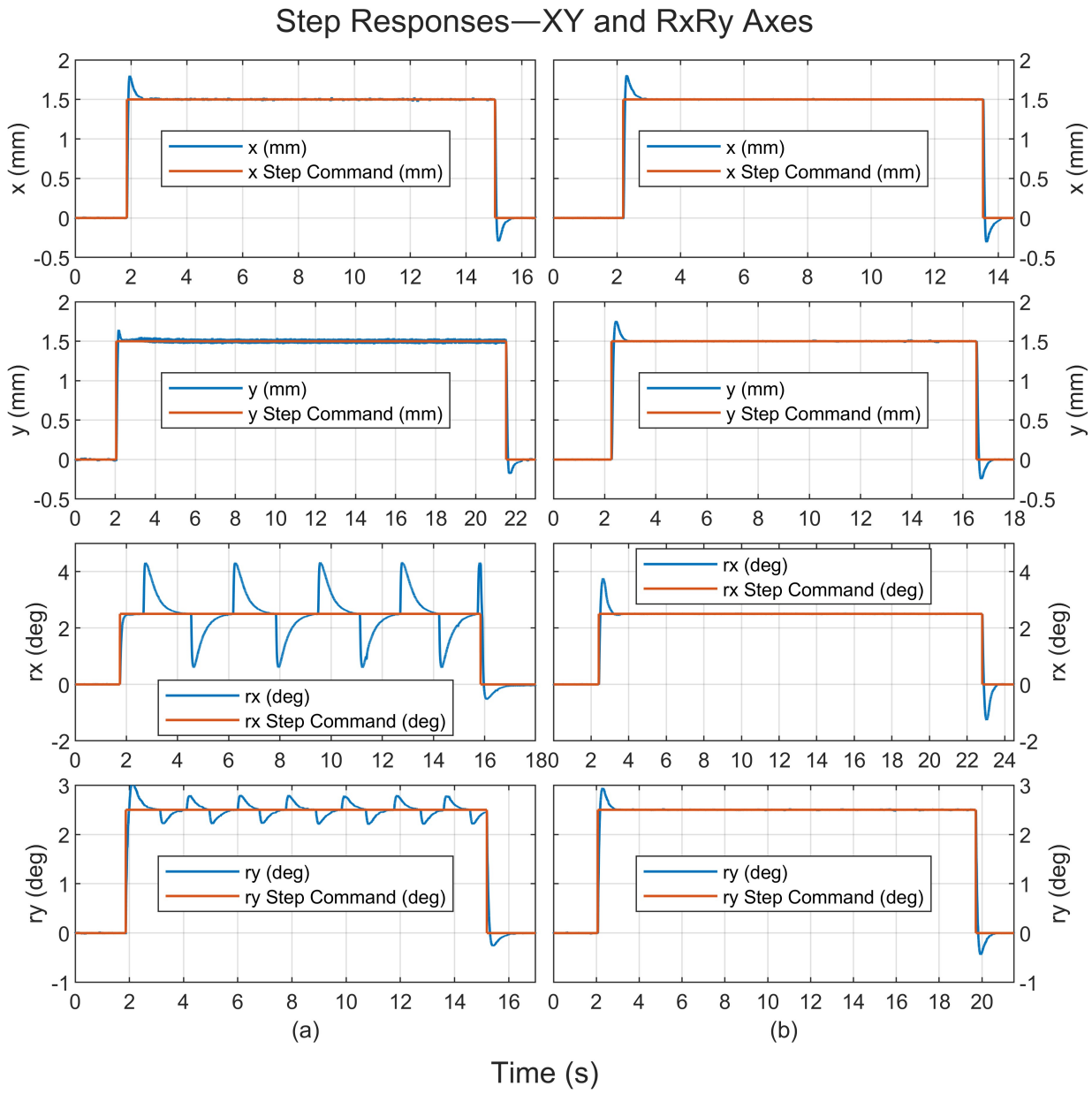


Figure 6.3: x–y and ψ–θ axes interpolation results: **(a)** step responses without linear interpolations. **(b)** step responses with 2-D linear interpolations.

6.2.2 Step and Microstep Responses

First, the mover is controlled to move with a step motion of 1 mm in x and y axes, and 2 mm in the z axis for translation. For rotation, the mover is rotated with a 1-degree step for both roll and pitch motion. The step response results of all five motions are plotted in Fig. 6.4. The characteristics of the step response are detailed in Table 6.3.

Next, the precision motion performance of all five motions, x, y, z, ψ, and θ, is shown in Fig. 6.5. The proposed planar maglev system can be controlled with the precise step of 10 μm in x, y, and z axes; and 0.5 mrad in roll ψ and pitch θ. An unexpected spike can be observed in some motion results. The precise step performances are almost limited by the sensor resolutions. These performances indicate that the system is capable of precise controls on all axes.

Table 6.3: 10-Coil Testbed: 5-DOF step response characteristics.

DOF	Characteristics		
	T_{rise} (ms)	Overshoot (%)	T_{settle} (ms)
X	38	20	460
Y	62	16.4	515
Z	46	19	554
Roll	57	50	1023
Pitch	75	17.2	695

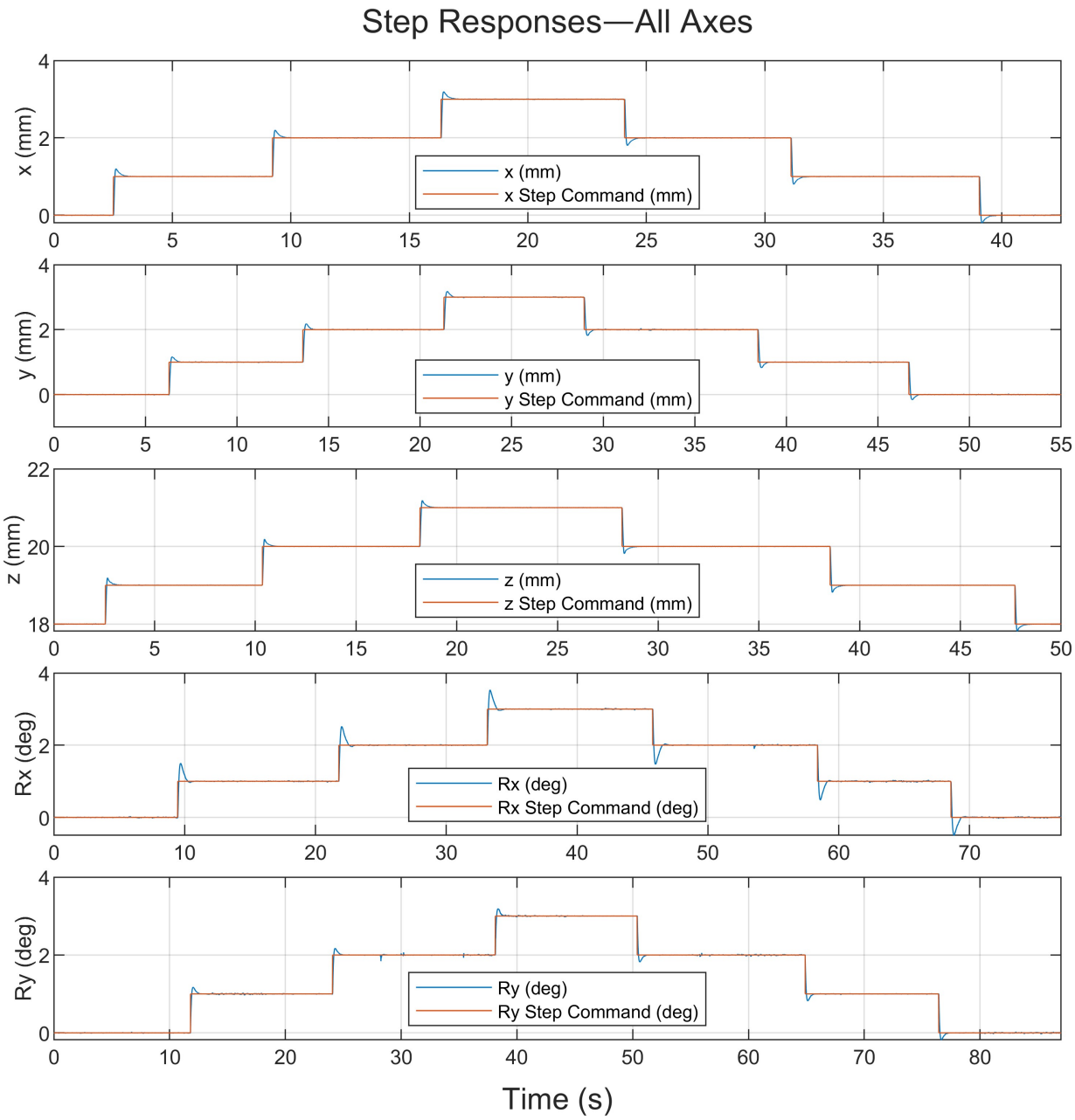


Figure 6.4: All axes step responses.

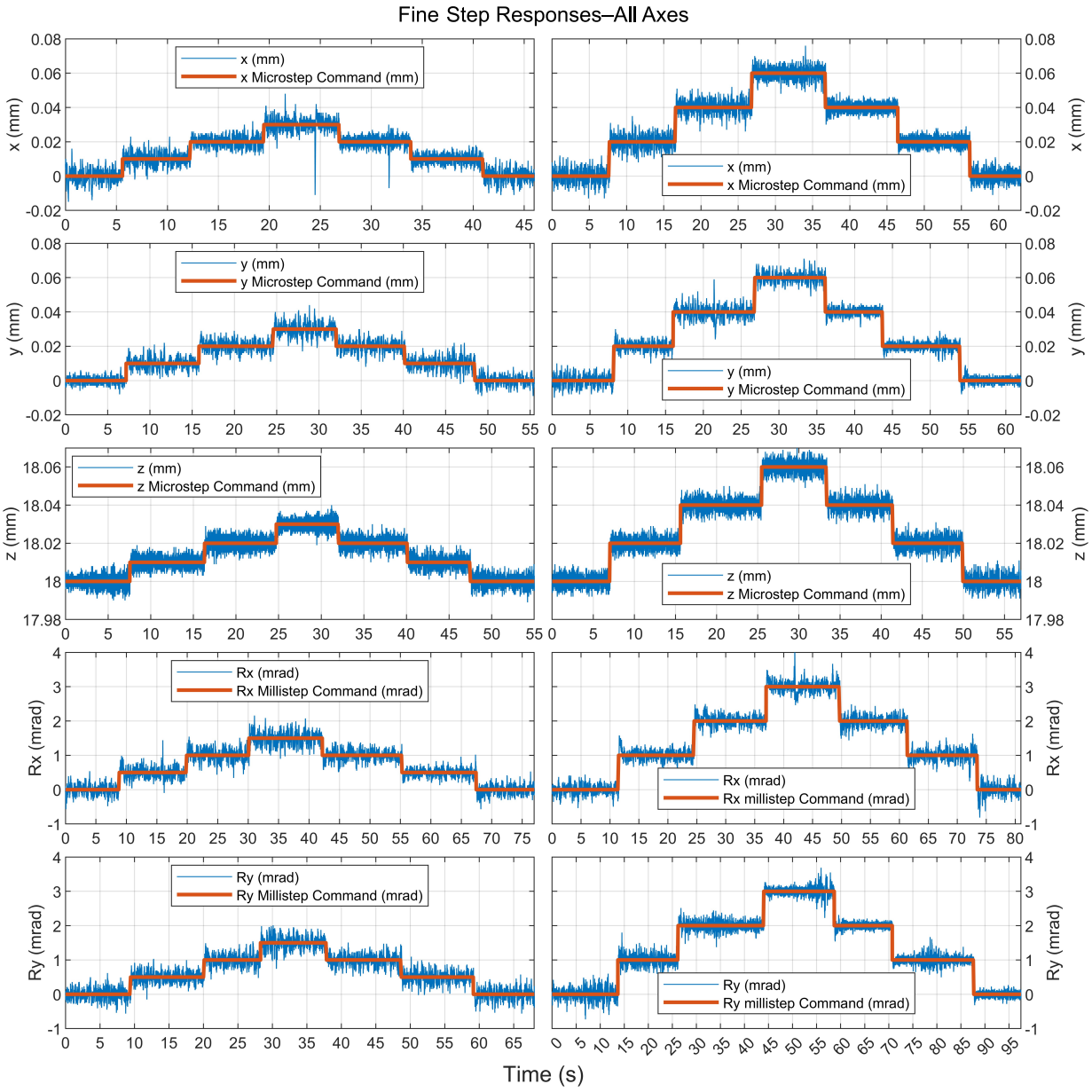


Figure 6.5: All axes fine step responses.

6.2.3 Full-Range Trajectory Tracking

To demonstrate the full-range motion of the proposed system, two experiments have been conducted. One is focused on translational trajectory tracking. The other is focused on the rotational ramp command following.

For trajectory tracking in translation, the motion range is defined to be equal to the lookup table data range, which ranges from -10 mm to 10 mm on both x and y axes, and 18 mm to 26 mm on the z axis. Figure 6.7 represents the full-range motion in the lookup region and the motions of each axis are shown in Fig. 6.8. Note that the ramp commands are applied on the x and y axes where the z axis is a step command. Therefore, the large overshoot along the z axis can be observed.

For rotation motion, to avoid the mover colliding with the base surface at a maximum rotation angle, the mover must be levitated at 26 mm. The results of full range rotation with the ramp command are shown in Fig. 6.9. The mover is rotated with roll ψ for ± 10 degrees. Then, the mover continued to rotate with the same rotation range for pitch θ. Figure 6.6 represents the mover was levitated at 26 mm and rotated with pitch angle θ of 10 degrees. The results were recorded at the same time scale. Each column used different vertical scales to fit with the motion results.

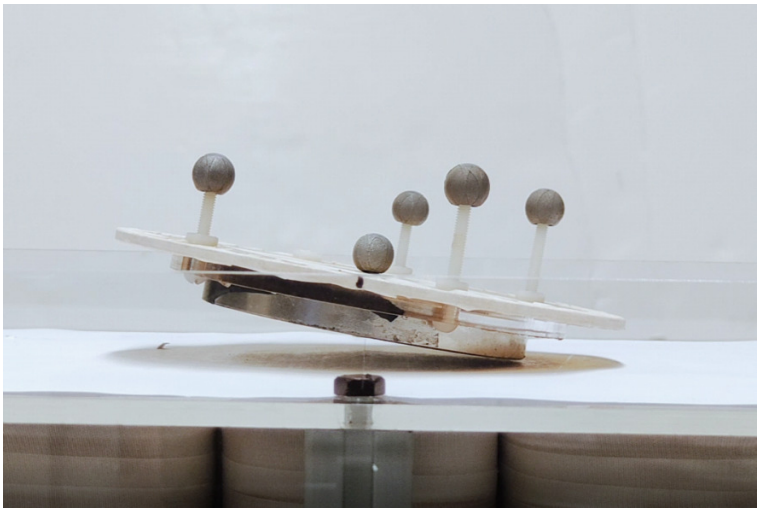


Figure 6.6: The disc magnet mover levitated at 26 mm and rotated with pitch angle of 10 degrees.

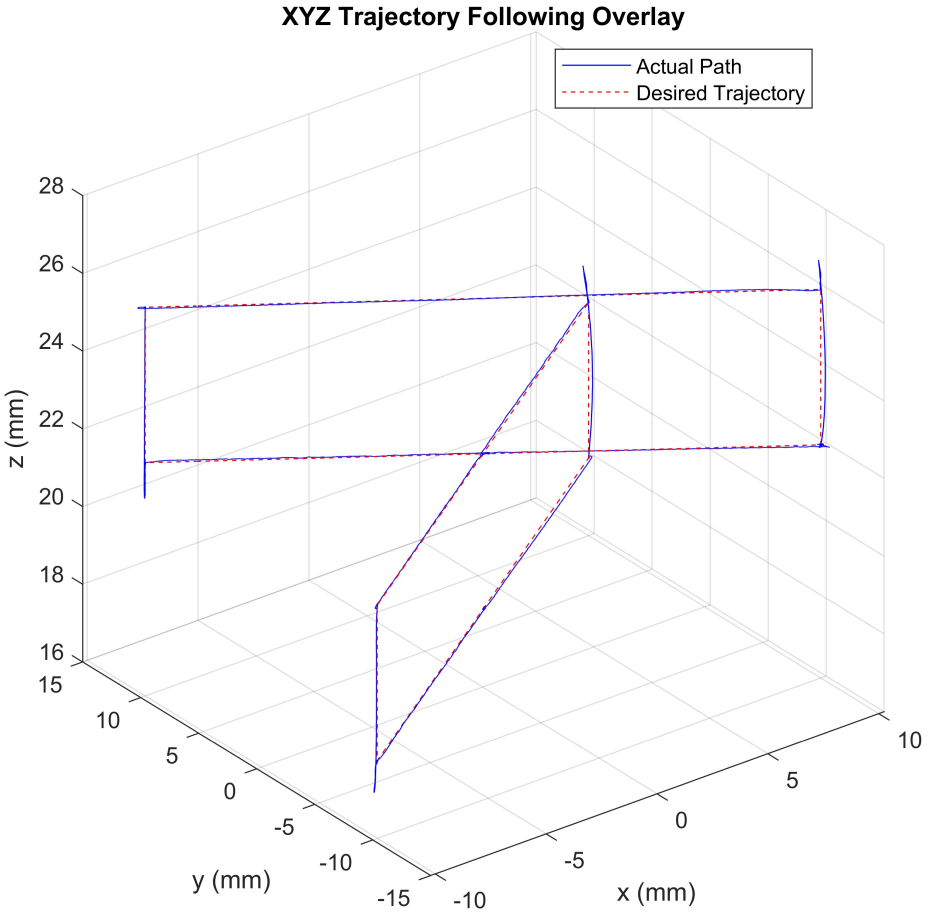


Figure 6.7: Full-range trajectory following.

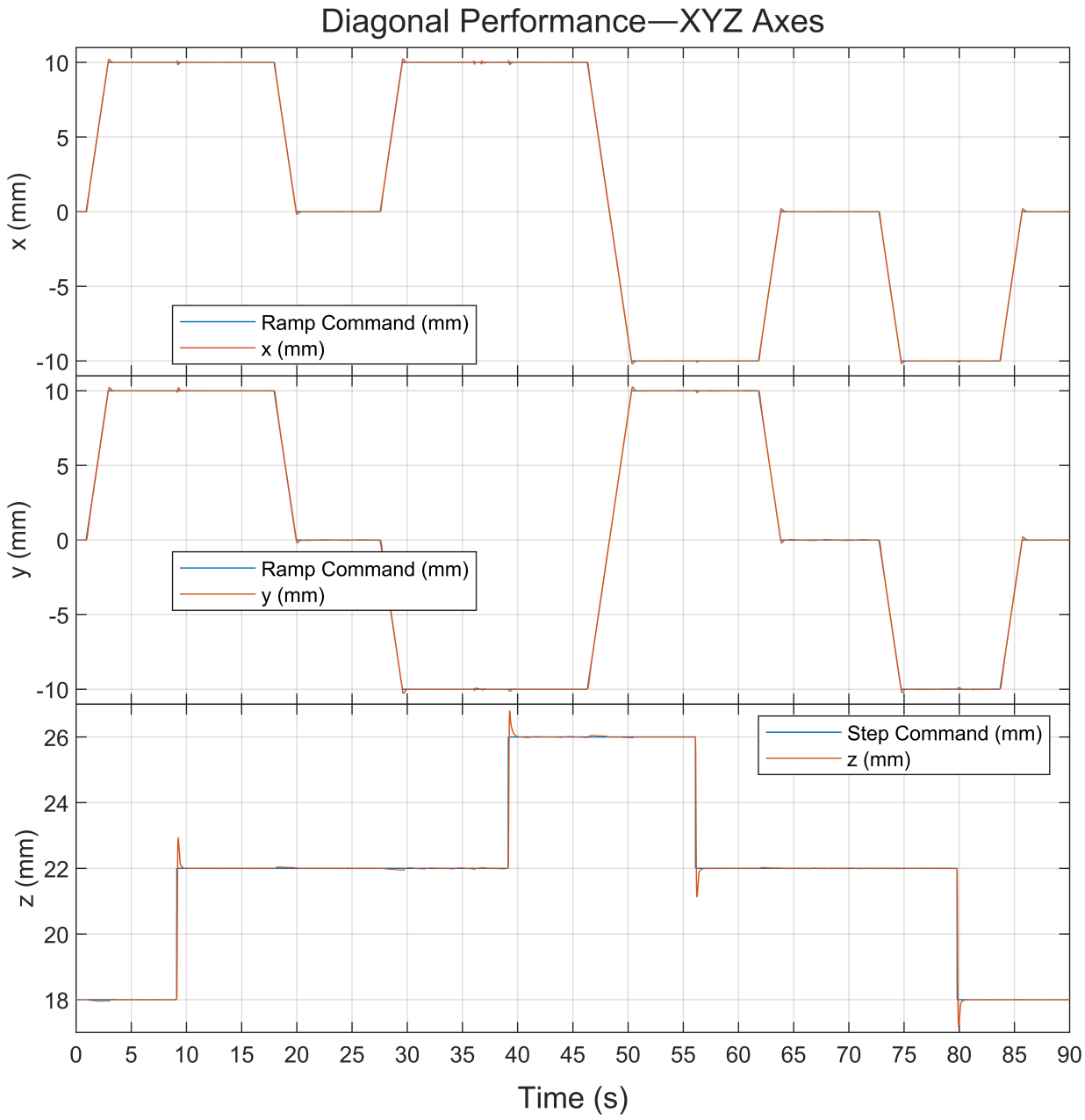


Figure 6.8: Full-range trajectory following performance.

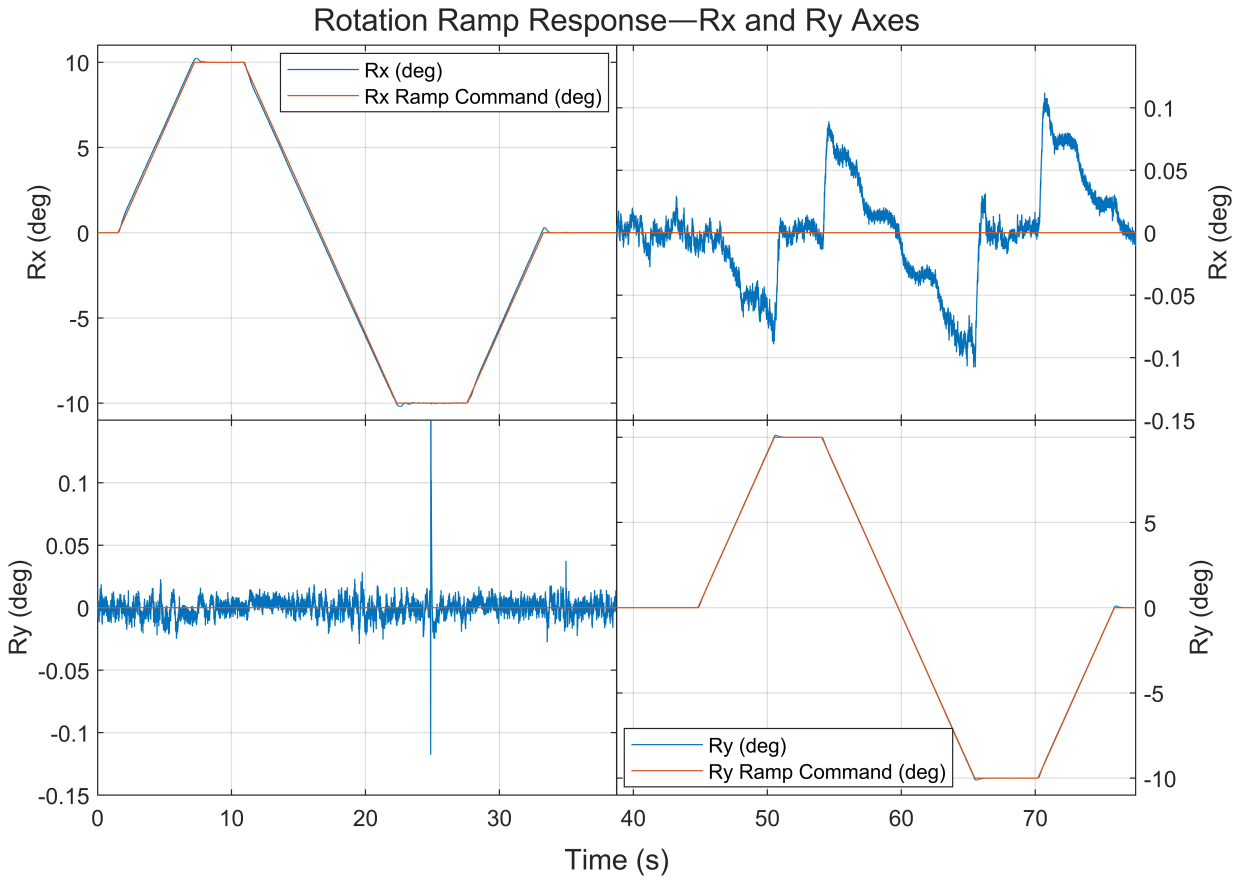


Figure 6.9: ψ–θ axes ramp responses.

6.3 Summary

This chapter presents implementation and levitation experiments on the planar maglev prototype, 10-Coil Testbed, with a single 4-inch disc magnet mover. By using the lookup table method, the decoupling performance when the mover is levitated at the middle of the lookup data, especially roll and pitch rotations. With the implementation of multivariate linear interpolation, the decoupling effectiveness was significantly enhanced to solve the data switching problem. However, only 2-DOF linear interpolation can be applied due to the limitation of the control hardware. The system can move with fine steps which can attain minimum achievable accuracy limited by the motion tracking sensor resolution. The levitation results demonstrated the levitate performance within the lookup data range.

Chapter 7

Implementation on Magnetic Levitation Floor Prototype

This chapter presents the implementation and levitation experiment results on the planar maglev prototype, Proto-MagFloor, with a single 4-inch disc magnet mover and a multiple-disc magnet mover. First, a decoupling problem with discrete lookup data is solved by the 5-DOF and 6-DOF linear interpolation. Next, the long-range levitation experiments are conducted in both translation and rotation.

7.1 Magnetic Levitation Floor Prototype (Proto-MagFloor) System Setup

7.1.1 System Setup

Figure 7.1 represents the overall setup of the Proto-MagFloor system with the motion tracking system. The motion tracking system has four cameras (VICON Vantage V5) to detect the reflective markers on the mover. Then, the data is transmitted over the Ethernet to the software to compute the mover position and orientation. With proper calibration, the motion tracking system can provide position and orientation data with ± 10 μm and ± 0.2 mrad resolution with an update frequency of 1 kHz to the controller via UDP protocol. With the same sampling frequency of 1 kHz, the controller operates with the implemented control algorithms to determine the coil currents. The current command outputs are sent out to the current amplifiers via EtherCAT communication.



Figure 7.1: Proto-MagFloor: System setup.

7.1.2 Lookup Table

The lookup table data range for single-disc magnet mover and multiple-disc magnet mover are detailed in Tables 7.1 and 7.2, respectively.

For translation, the XY data ranges for both movers are the same from 0 mm to 40 mm with an increment of 2 mm for both axes. This data range is the minimum planar range as proposed in the long-range planar levitation strategy. For levitation height, the single-disc magnet mover has a higher range than the multiple-disc magnet mover. The maximum height of the single-disc magnet mover is 36.35 mm or 30 mm air gap levitation. The maximum height of the multiple-disc magnet mover is 30 mm or 15 mm air gap levitation.

For rotation, both roll and pitch rotation range for both movers are the same from -10 degrees to 10 degrees with an increment of 10 degrees. For a multiple-disc magnet mover, the mover can rotate with yaw angle. The yaw rotation data range is from 0 degree to 90 degrees with 15 degrees increment step.

The total number of combinations for 5-DOF lookup data is 23814 combinations. The total number of combinations for 6-DOF lookup data is 222264 combinations.

Table 7.1: Proto-MagFloor: 5-DOF lookup data range for a single-disc magnet mover.

DOF	Min value	Increment	Max value
Translation (mm)			
X	0.0	2.0	40.0
Y	0.0	2.0	40.0
Z	26.35	2.0	36.35
Rotation (deg)			
Roll ψ	-10.0	10.0	10.0
Pitch θ	-10.0	10.0	10.0
Total number of combination:			23814

Table 7.2: Proto-MagFloor: 6-DOF lookup data range for a four-disc magnet mover.

DOF	Min value	Increment	Max value
Translation (mm)			
X	0.0	2.0	40.0
Y	0.0	2.0	40.0
Z	16.0	2.0	30.0
Rotation (deg)			
Roll ψ	-10.0	10.0	10.0
Pitch θ	-10.0	10.0	10.0
Yaw ϕ	0.0	15.0	90.0
Total number of combination:			222264

7.1.3 Multivariate Linear Interpolation

To enhance the decoupling performance, multivariate linear interpolation was implemented in this experiment to solve the data switching problem. For a single-disc magnet mover, the maximum number of controllable degrees of freedom is 5. For a multiple-disc magnet mover, the maximum number of controllable degrees of freedom is 6.

The 5-DOF linear interpolation can be formulated by determining the related indices from the mover pose: (x_0, y_0, z_0, ψ_0, θ_0). The decoupling matrices are looked up using 5 state pairs (x_1, x_2), (y_1, y_2), (z_1, z_2), (ψ_1, ψ_2), and (θ_1, θ_2). For 5-DOF linear interpolation, there are $2^5 = 32$ matrices to be searched for estimation.

For 6-DOF linear interpolation, the yaw angle in the mover pose ϕ_0 is considered. By adding one additional state pair (ϕ_1, ϕ_2), the number of lookup data for estimation becomes $2^6 = 64$ matrices.

7.1.4 Control System and Long-Range Decoupling Strategy

The multi-DOF control diagram is illustrated in Fig. 7.2. By using the decoupling matrix $\mathbf{K}^+$, the cross-coupling effect can be decoupled and multiple PID controllers can be applied to control each degree of freedom separately. The pre-computed wrench matrices are stored in the lookup table. The corresponding wrench matrix can be looked up by using the mover pose obtained from the motion tracking system. An additional gravity compensator is used to compensate for the mover weight in a vertical motion.

The PID parameters for the 5-DOF single-disc magnet mover are shown in Table 7.3. The PID parameters for the 6-DOF multiple-disc magnet mover are shown in Table 7.4. Since the weight of both movers has comparable weight, most of the PID parameters in both translations and rotations are similar. Only D gains for roll and pitch angle and PID control for yaw rotation of the multiple-disc magnet mover were tuned.

Figure 7.3 represents the user interface of the control program in TwinCAT 3. The top part of the interface has toggle switches to enable the amplifiers, reset system errors, and enable the control program. The middle part shows PID control gains and motion command configurations. The bottom part displays motion reading from the sensors via UDP and path command functions. Since the main control algorithm and decoupling strategies were developed in MATLAB Simulink, the Simulink task processing time for both 5-DOF and 6-DOF maglev systems are less than 14 µs and 20 µs as shown in Fig. 7.4a and Fig. 7.4b respectively. This validates the feasibility of the developed algorithm for real-time control.

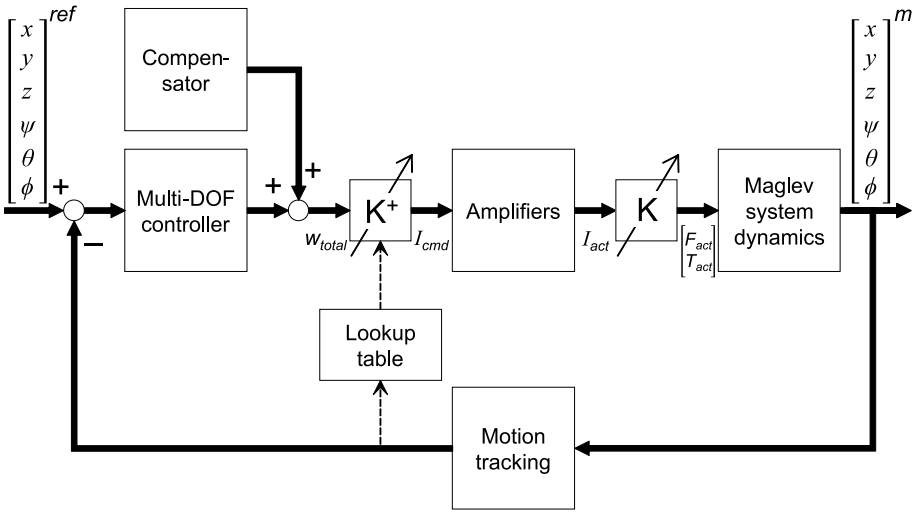


Figure 7.2: Proto-MagFloor: Multi-DOF PID control diagram.

Table 7.3: Proto-MagFloor: 5-DOF PID controller parameters for a single-disc magnet mover.

DOF	PID controller					
	P gain		I gain		D gain	
X	1200	N/m	6000	N/m·s	55	N·s/m
Y	1200	N/m	6000	N/m·s	55	N·s/m
Z	1200	N/m	6000	N/m·s	55	N·s/m
Roll ψ	1.5	N·m/rad	8	N·m/rad·s	0.055	N·m·s/rad
Pitch θ	1.5	N·m/rad	8	N·m/rad·s	0.055	N·m·s/rad

Table 7.4: Proto-MagFloor: 6-DOF PID controller parameters for a four-disc magnet mover.

DOF	PID controller					
	P gain		I gain		D gain	
X	1200	N/m	6000	N/m·s	60	N·s/m
Y	1200	N/m	6000	N/m·s	60	N·s/m
Z	1200	N/m	6000	N/m·s	60	N·s/m
Roll ψ	1.5	N·m/rad	8	N·m/rad·s	0.07	N·m·s/rad
Pitch θ	1.5	N·m/rad	8	N·m/rad·s	0.07	N·m·s/rad
Yaw ϕ	2.0	N·m/rad	8	N·m/rad·s	0.07	N·m·s/rad

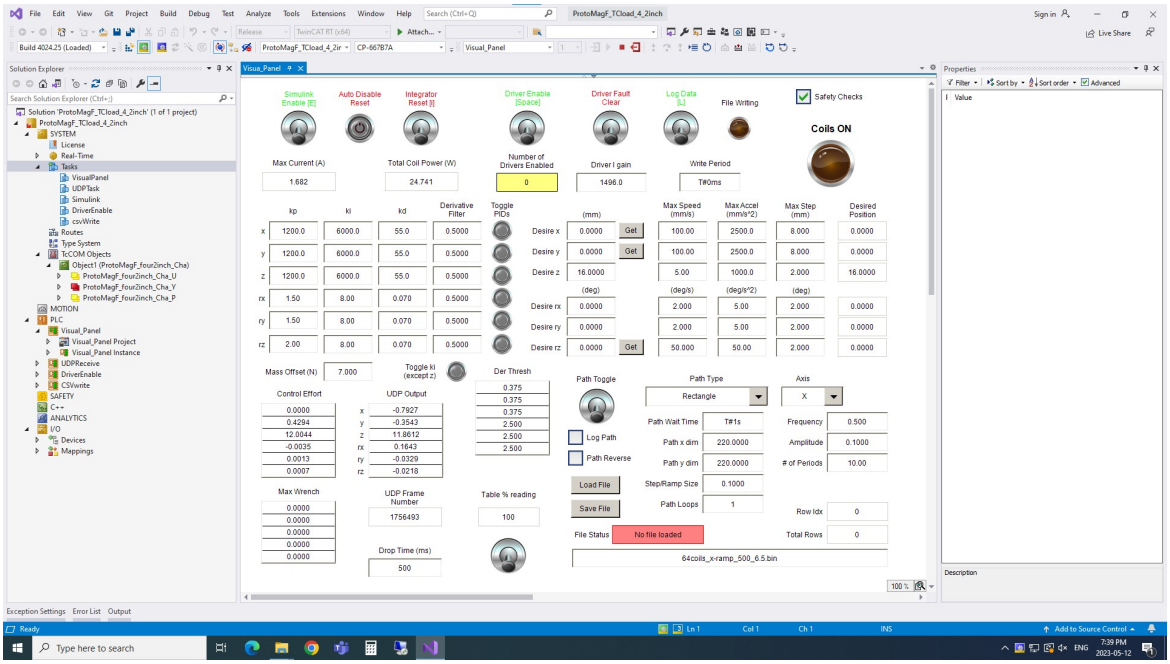
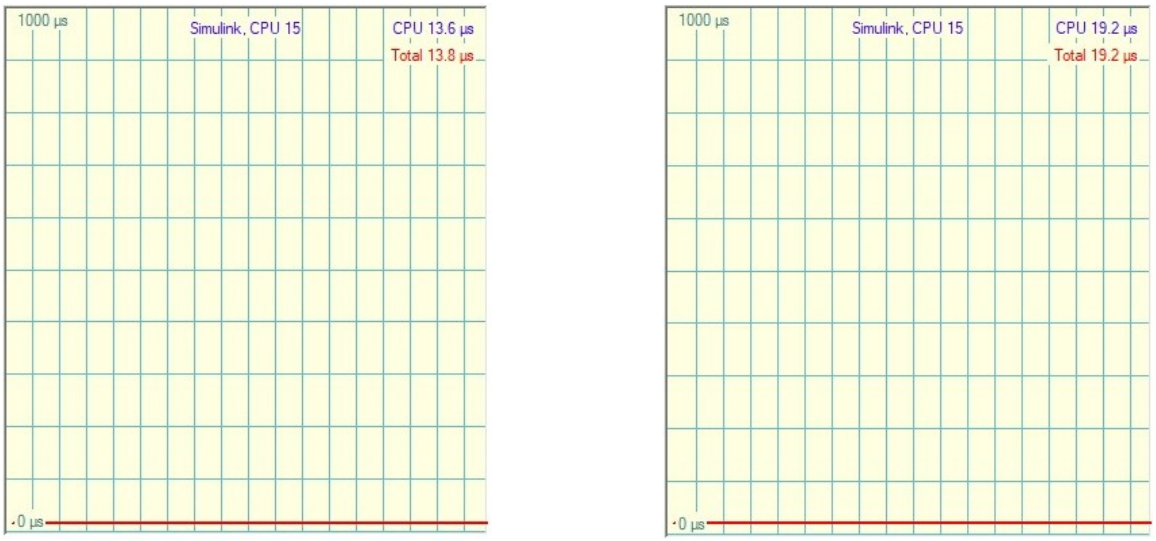


Figure 7.3: Proto-MagFloor: TwinCAT program user interface.



(a) (b)

Figure 7.4: Simulink task processing time in TwinCAT program. **(a)** 5-DOF system. **(b)** 6-DOF system.

7.2 Experiment Results on Proto-MagFloor: Single-Disc Magnet Mover

Experiment results on the Proto-MagFloor with a single 4-inch disc magnet mover are presented in this section. Experiments consist of step motion and long-range motion in both translation and rotation. Figure 7.5 represents the mover levitating above the system.

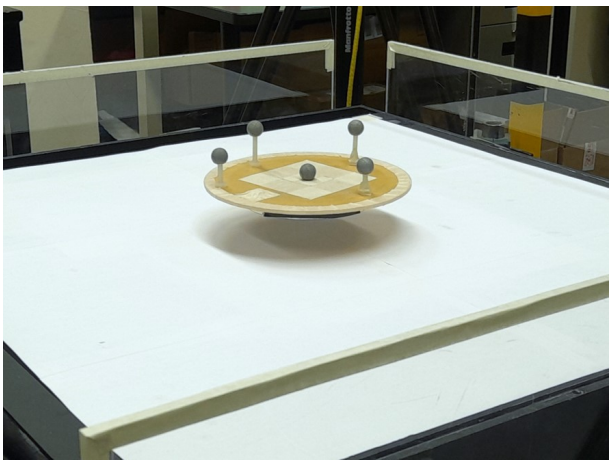


Figure 7.5: Proto-MagFloor with a single 4-inch disc magnet mover.

7.2.1 Step Motion Responses and Interpolation Implementation

First, the mover is controlled to move with step motions of 3 mm in x and y axes, and 2 mm in the z axis for translation. For rotation, the mover is rotated with a 2.5-degree step for both roll and pitch motion. The step response results of all five motions are plotted in Fig. 7.6. The large oscillations can be observed in roll and pitch rotation due to the data switching problem at -5 degrees which is a middle value between two lookup states: 0 degree and -10 degrees. With an implementation of the 5-DOF linear interpolation, the oscillations in both DOF are eliminated.

Next, the precision motion performance of all five motions, x, y, z, ψ, and θ, is shown in Fig. 7.7. The mover can be controlled with the precise step of 10 μm and 20 μm in x, y, and z axes; and 0.1 rad and 0.2 rad in roll ψ and pitch θ. High overshoot can be found in roll and pitch rotation with 0.1 rad step. These performances indicate that the system is capable of precise controls on all axes limited by the motion tracking sensor.

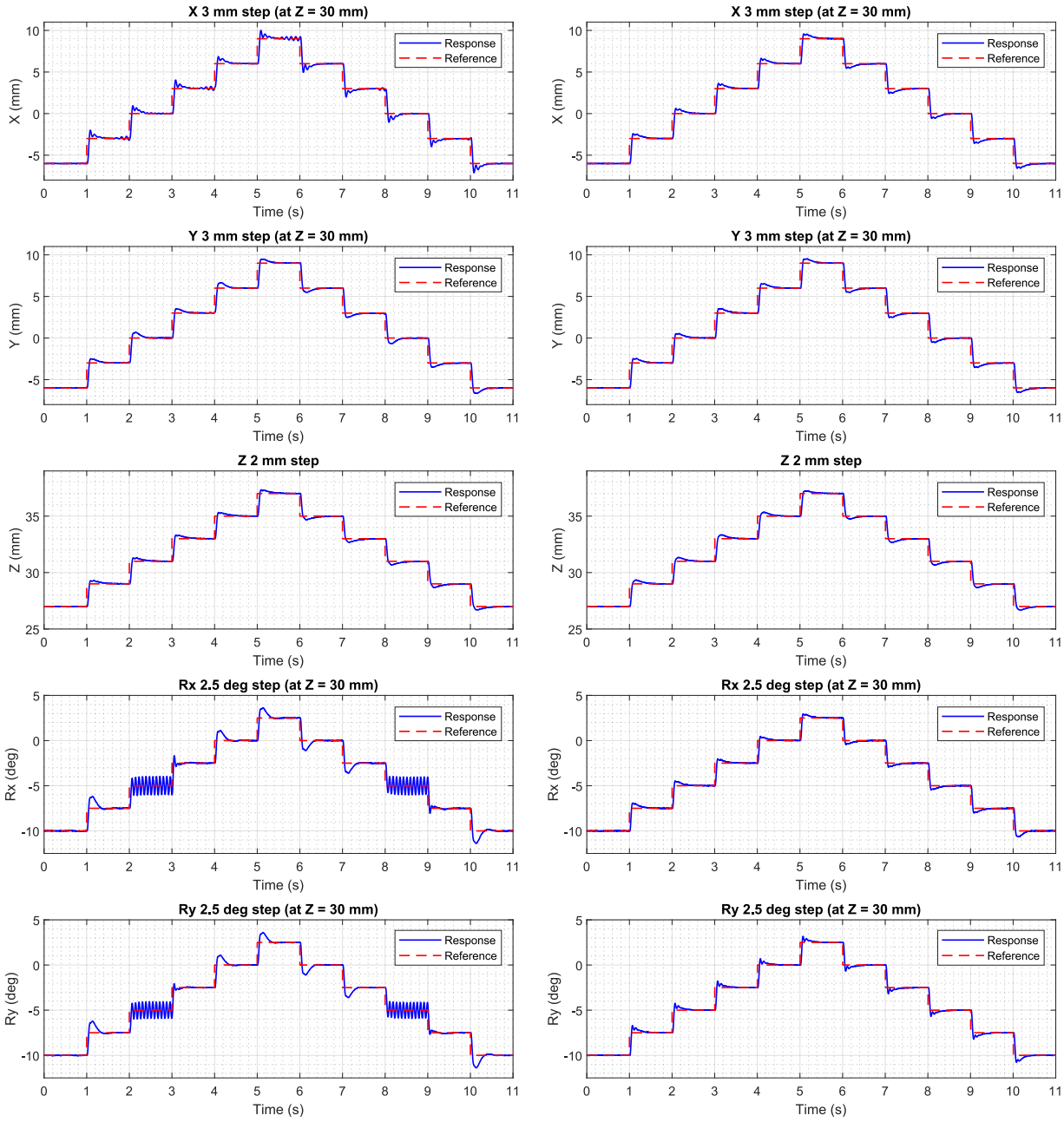


Figure 7.6: Proto-MagFloor single 4-inch PM experiment results 1: 5-DOF step motion. **(left)** without interpolation. **(right)** with interpolation.

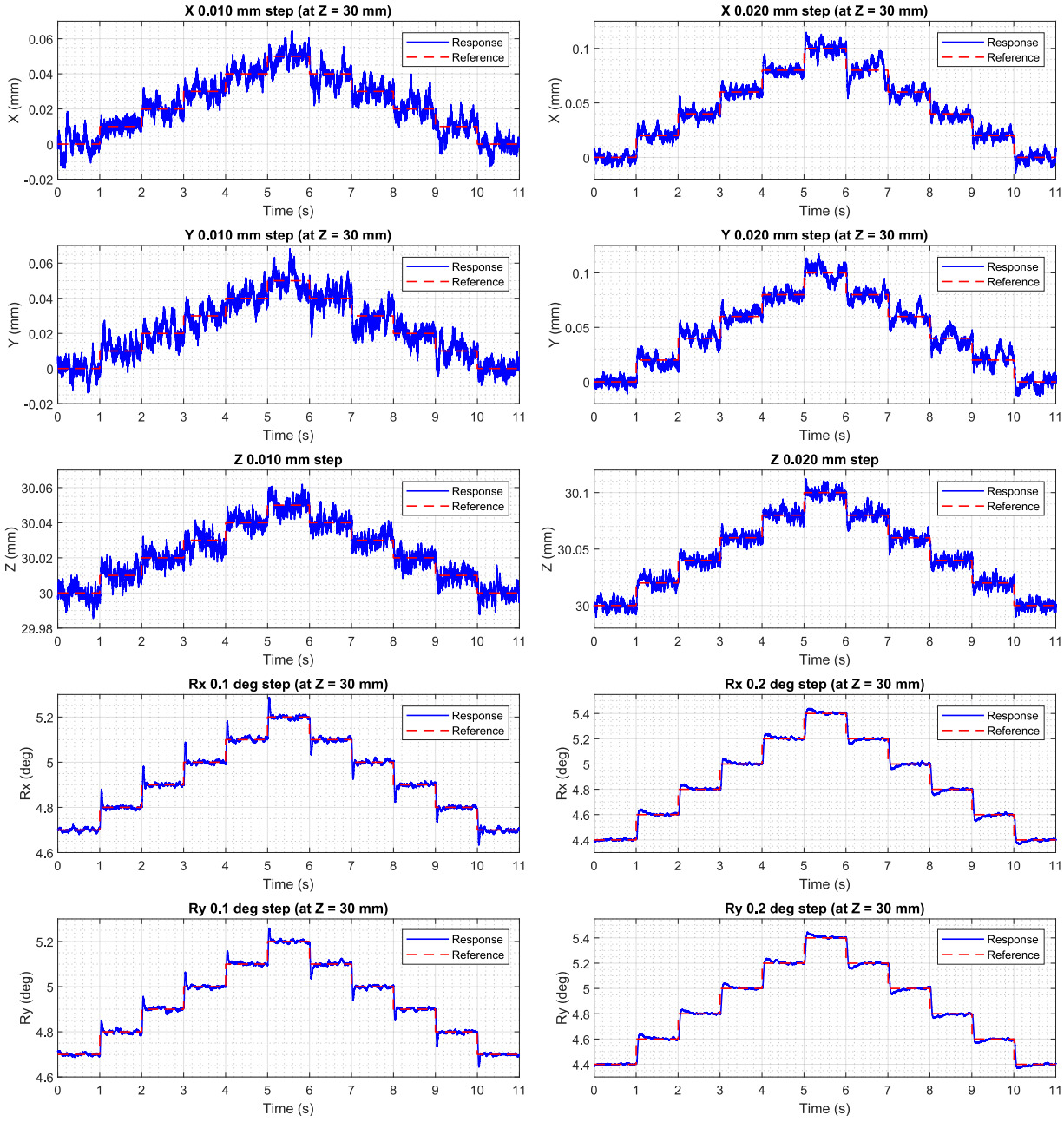


Figure 7.7: Proto-MagFloor single 4-inch PM experiment results 2: Fine step motion.

7.2.2 Long-Range Trajectory Tracking

To demonstrate the long-range levitation, the proposed long-range decoupling strategy was implemented. Two experiments have been conducted. The first experiment is translational trajectory tracking. The second experiment is the rotations in both roll and pitch.

Long-Range Translation

For trajectory tracking in translation, the motion range is defined to be ±190 mm in both x and y axes, and 26.35 mm to 36.35 mm in the z axis. Figure 7.8 represents the long-range motion over the Proto-MagFloor area and the motions of each axis are shown in Fig. 7.9. The ramp commands are applied on all x, y, and z translation axes. Meanwhile, the cross-coupling effect during the motion in roll and pitch can be observed within the range of ±1 degree. For example, large oscillations in roll (Rx) motion occur when the mover moves along the Y-axis and vice versa.

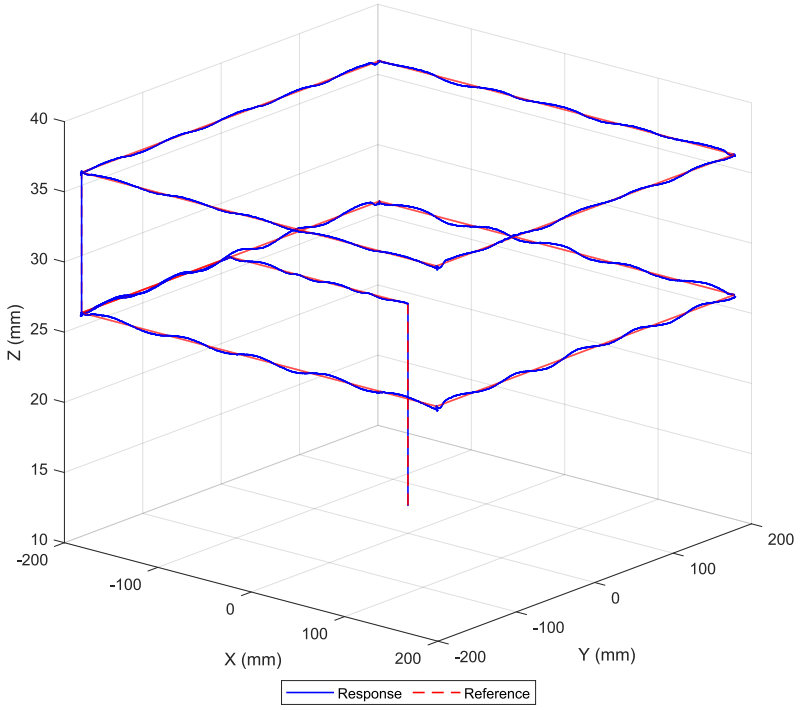


Figure 7.8: Proto-MagFloor single 4-inch PM experiment results 3: X-Y-Z full-range motion.

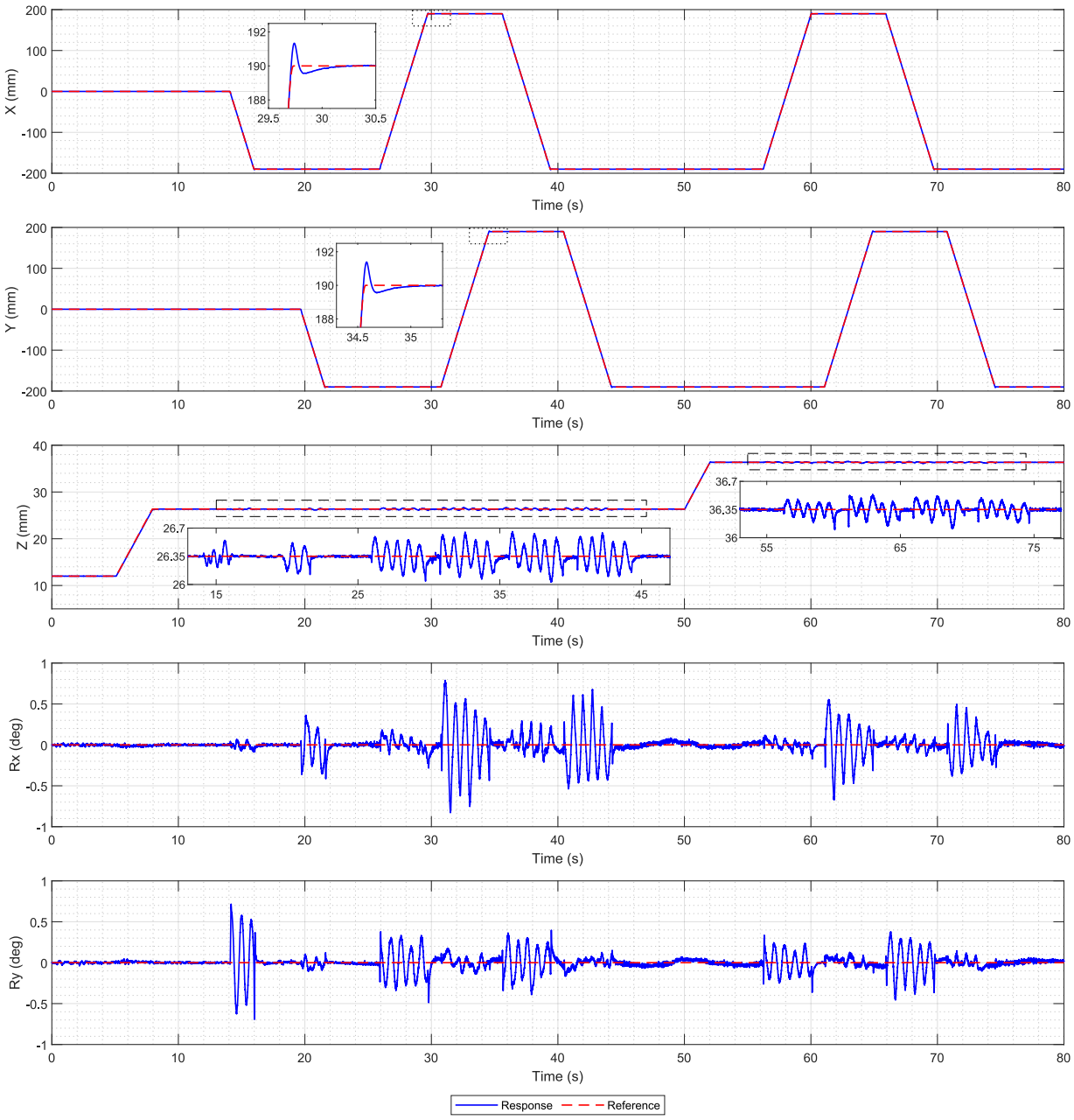


Figure 7.9: Proto-MagFloor single 4-inch PM experiment results 4: X-Y-Z full-range motion with 5-DOF responses.

Full-Range Rotation: Roll and Pitch

For rotation motion, to avoid the mover colliding with the base surface at a maximum rotation angle, the mover must be levitated with its center at z = 30 mm.

The results of full range rotation with the ramp command are shown in Fig. 7.10. The mover is rotated with roll ψ for ± 10 degrees. Then, the mover continued to rotate with the same rotation range for pitch θ. The responses in x, y, and z axes are within ± 40 µm. The rotation responses when not rotating are within 0.03 degrees.

Next, the mover is rotated in-place with ± 10 degrees for both roll and pitch as shown in Fig. 7.11. The trajectory tracking results in rotation demonstrate better performance. However, the oscillations in x, y, and z axes are ± 0.07 mm, which is larger than the previous experiment. The cross-coupling effect between x–pitch and y–roll can still be observed in this experiment.

Finally, the mover is rotated in-place with ± 20 degrees for both roll and pitch to evaluate the levitation performance out of the lookup range. The result plots as shown in Fig. 7.12 demonstrate the feasibility of the out-of-range rotation. However, the rotation tracking performance of the mover is worsened when the mover angle is larger than ± 10 degrees. Moreover, large oscillations occur in x and y are ± 1 mm and ± 0.3 mm for z axis.

This section demonstrates the levitation performance of the single-disc magnet mover on the Proto-MagFloor system. Without interpolation, large oscillations can be observed when the mover levitates in the middle of lookup states, especially in both rotations. By implementing a 5-DOF linear interpolation and decoupling strategy, the mover can move with smooth responses and be able to hover over the entire area of the coil array.

However, the remaining downside of this mover is yaw rotation control. Uncontrolled yaw rotation can disturb the motion responses in other degrees of freedom. Levitation experiments using multiple-disc magnet mover with yaw rotation are examined in the next section.

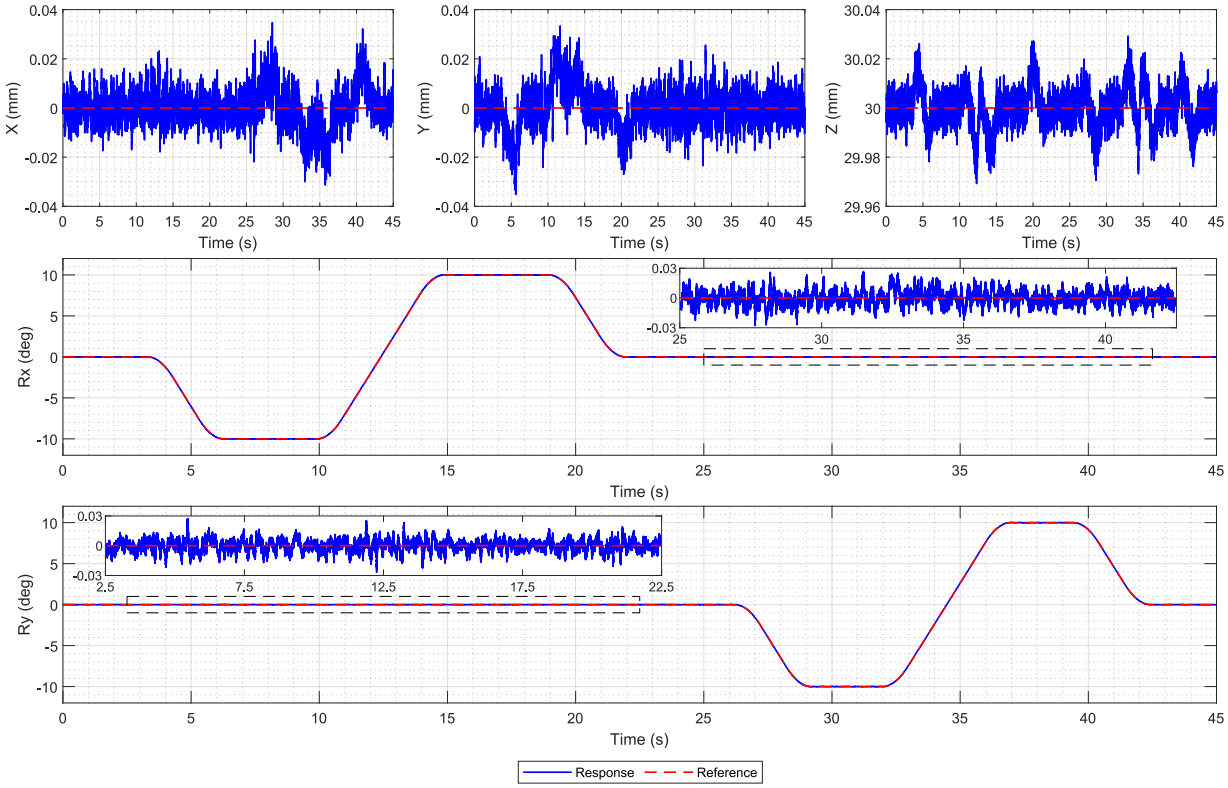


Figure 7.10: Proto-MagFloor single 4-inch PM experiment results 5: Roll and Pitch full-range motion.

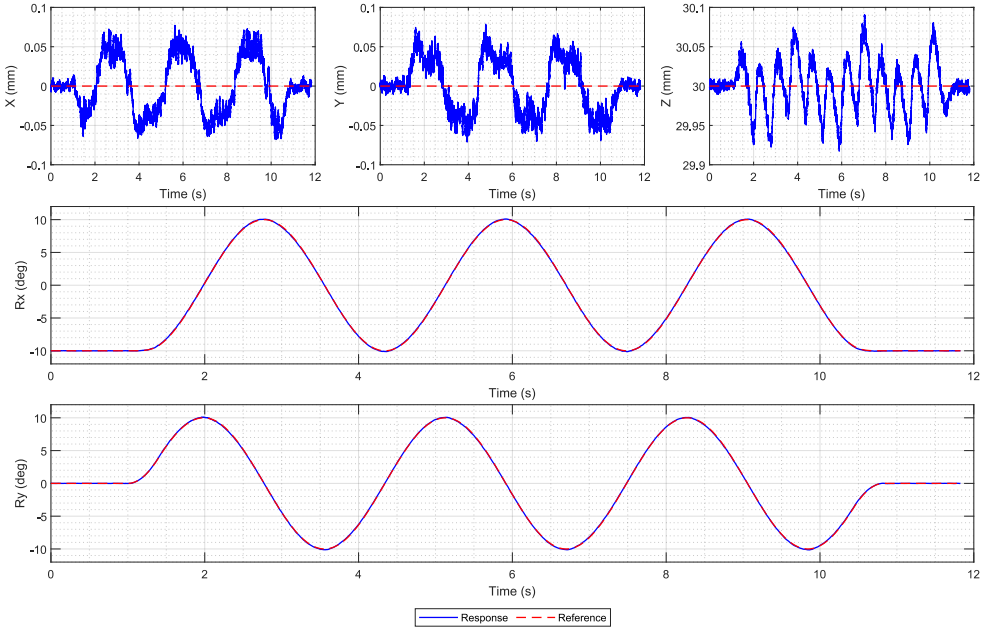


Figure 7.11: Proto-MagFloor single 4-inch PM experiment results 6: In-place rotation ±10 degrees.

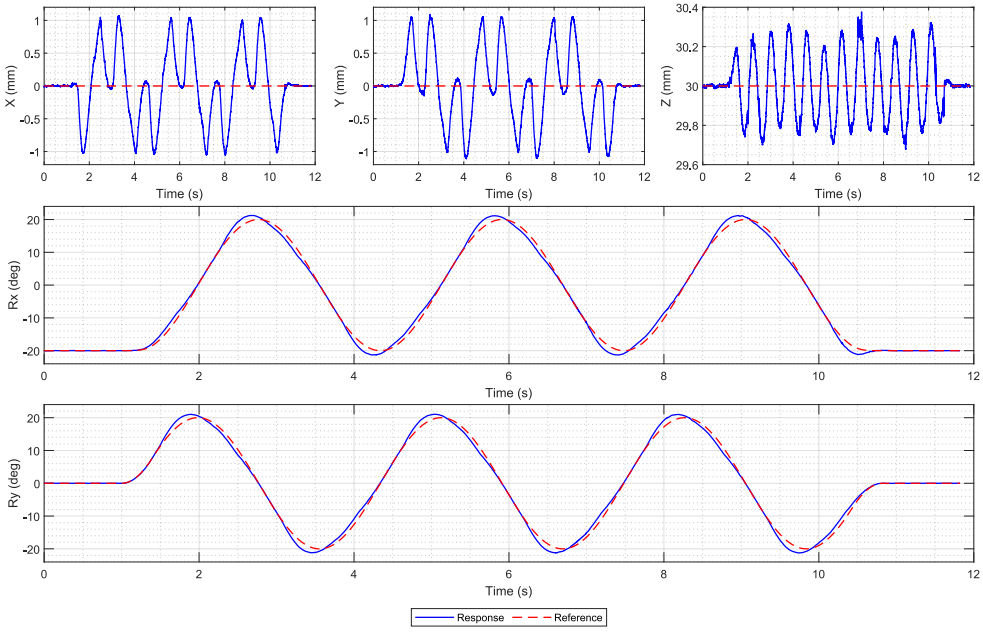


Figure 7.12: Proto-MagFloor single 4-inch PM experiment results 7: In-place rotation ±20 degrees.

7.3 Experiment Results on Proto-MagFloor: Multiple-Disc Magnet Mover

Experiment results on the Proto-MagFloor with a four 2-inch disc magnet mover are presented in this section. Similar to a single-disc magnet, experiments consist of step motion and long-range motion in both translation and rotation including yaw rotation. Figure 7.13 represents the mover levitating above system with roll and pitch angles.

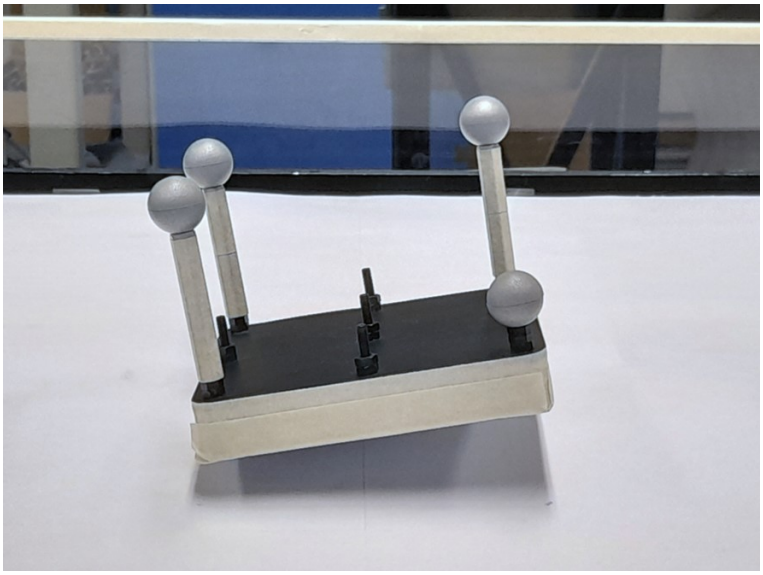


Figure 7.13: Proto-MagFloor with a four 2-inch disc magnet mover.

7.3.1 Step Motion Responses

For step motion, the mover is controlled to move with step motions of 3 mm in x and y axes, and 2 mm in the z axis. For rotation, the mover is rotated with 2.5-degree steps for both roll and pitch motion, and 1-degree steps for yaw motion. The step response results of all six motions are plotted in Fig. 7.14.

All step motions in translation and yaw rotation were conducted with the mover center levitates at z = 20 mm. For roll and pitch rotations, the mover center levitates to z = 30 mm to avoid the collision. The step responses in 5-DOF except yaw rotation have similar responses. However, the yaw step responses have a large overshoot even though the mover is rotated with a small angle up to 5 degrees.

Next, the fine-step motion performance of all six motions is shown in Fig. 7.15 for translation and Fig. 7.16 for rotation. The mover was controlled to move with the precise step of 20 μm and 50 μm in x, y, and z axes; and 0.1 deg and 0.2 deg in roll ψ, pitch ϕ, and pitch θ. For translation, the 20 μm step responses has large noise with random spike but the change of step still can be observed. For rotation, the step responses has high overshoot and long oscillation, especially in yaw motion.

By comparing the 20 μm step motion results of the multiple-disc magnet mover with the single-magnet mover, the multiple-disc magnet mover has larger oscillations than the single-disc mover.

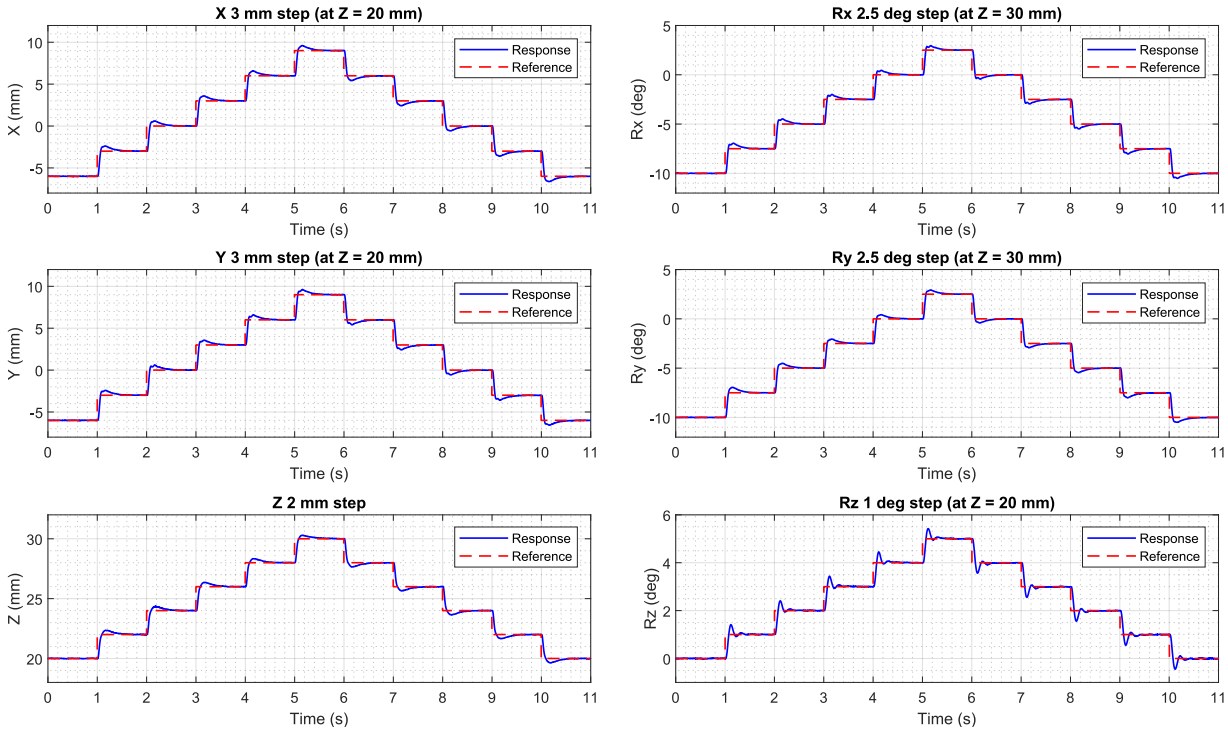


Figure 7.14: Proto-MagFloor four 2-inch PM experiment results 1: 6-DOF step motion.

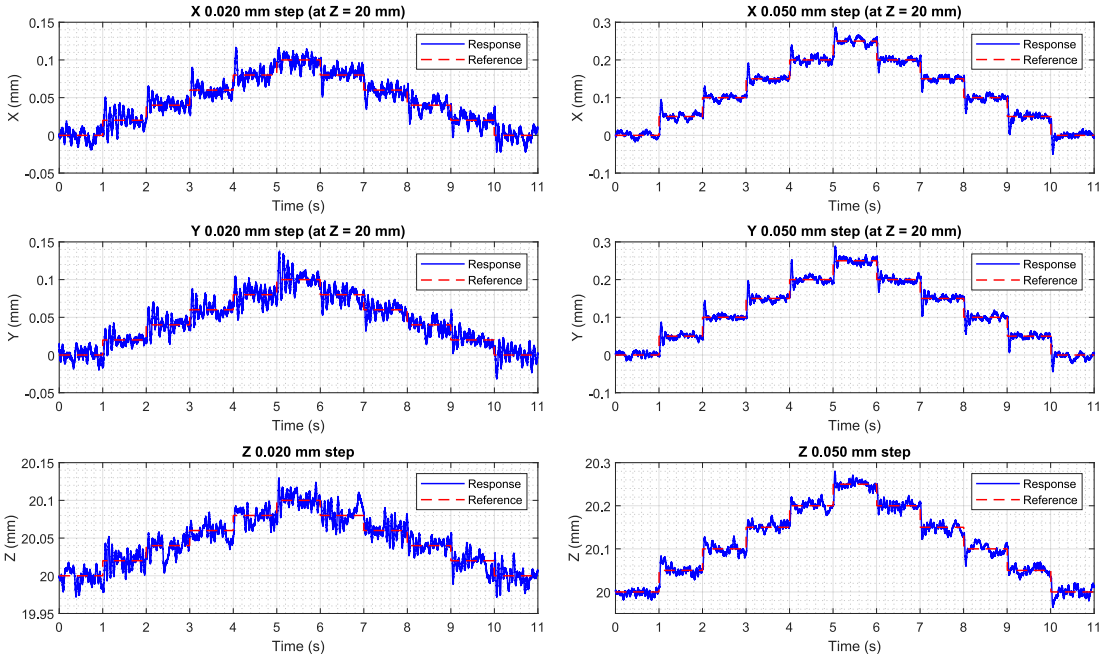


Figure 7.15: Proto-MagFloor four 2-inch PM experiment results 2: X-Y-Z fine step motion.

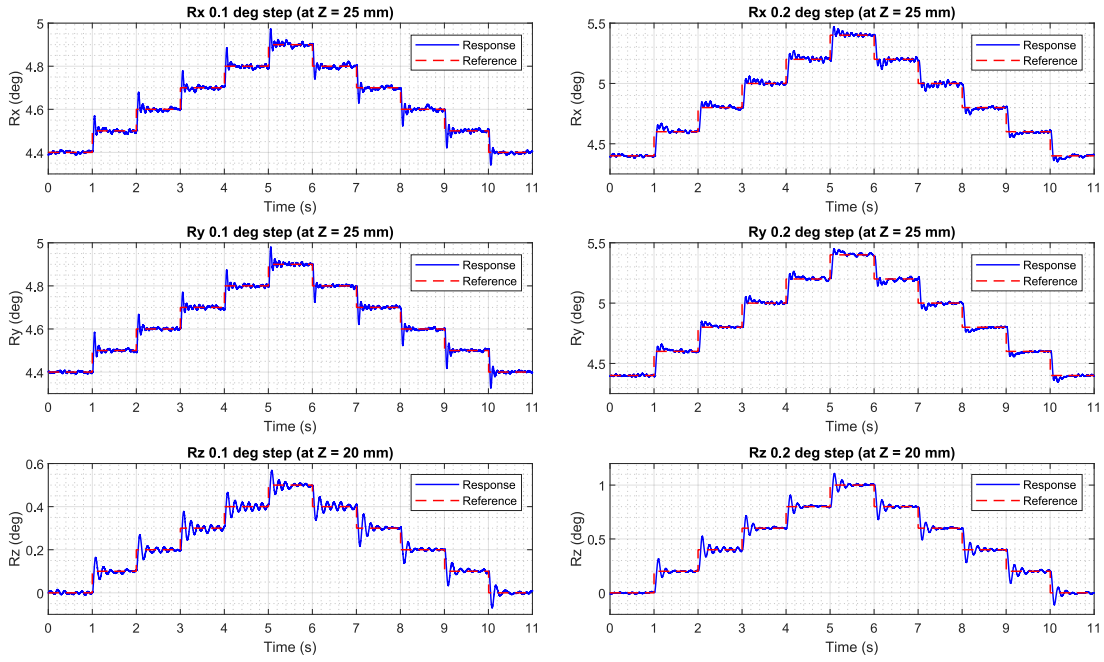


Figure 7.16: Proto-MagFloor four 2-inch PM experiment results 3: Roll-Pitch-Yaw fine step motion.

7.3.2 Long-Range Trajectory Tracking

To demonstrate the long-range motion control of the system and the implementation of the developed algorithm, two experiments have been conducted. The first experiment is the long-range translation. The second experiment is the rotational command following.

Long-Range Translation

For trajectory tracking in translation, two motion paths are defined for experiments. The first long-range translation path is a planar motion of ± 75 mm at z = 20 mm as shown in Fig. 7.17. The second long-range translation path is a planar motion of ± 150 mm at z = 20 mm as shown in Fig. 7.18.

For both long-range motions, the motion in x and y axes can follow the ramp command. However, large oscillations occur on other axes when the mover is moving along the path. For z motion, the mover oscillates within the range of ± 0.75 mm. The roll and pitch motions have large oscillations of ± 2 degrees and the range of the yaw motion is within ± 0.5 degrees except for the first part in ± 150 mm path. Most large oscillations emerge when the mover moves along the x axis from -75 mm to 75 mm or from -150 mm to 150 mm.

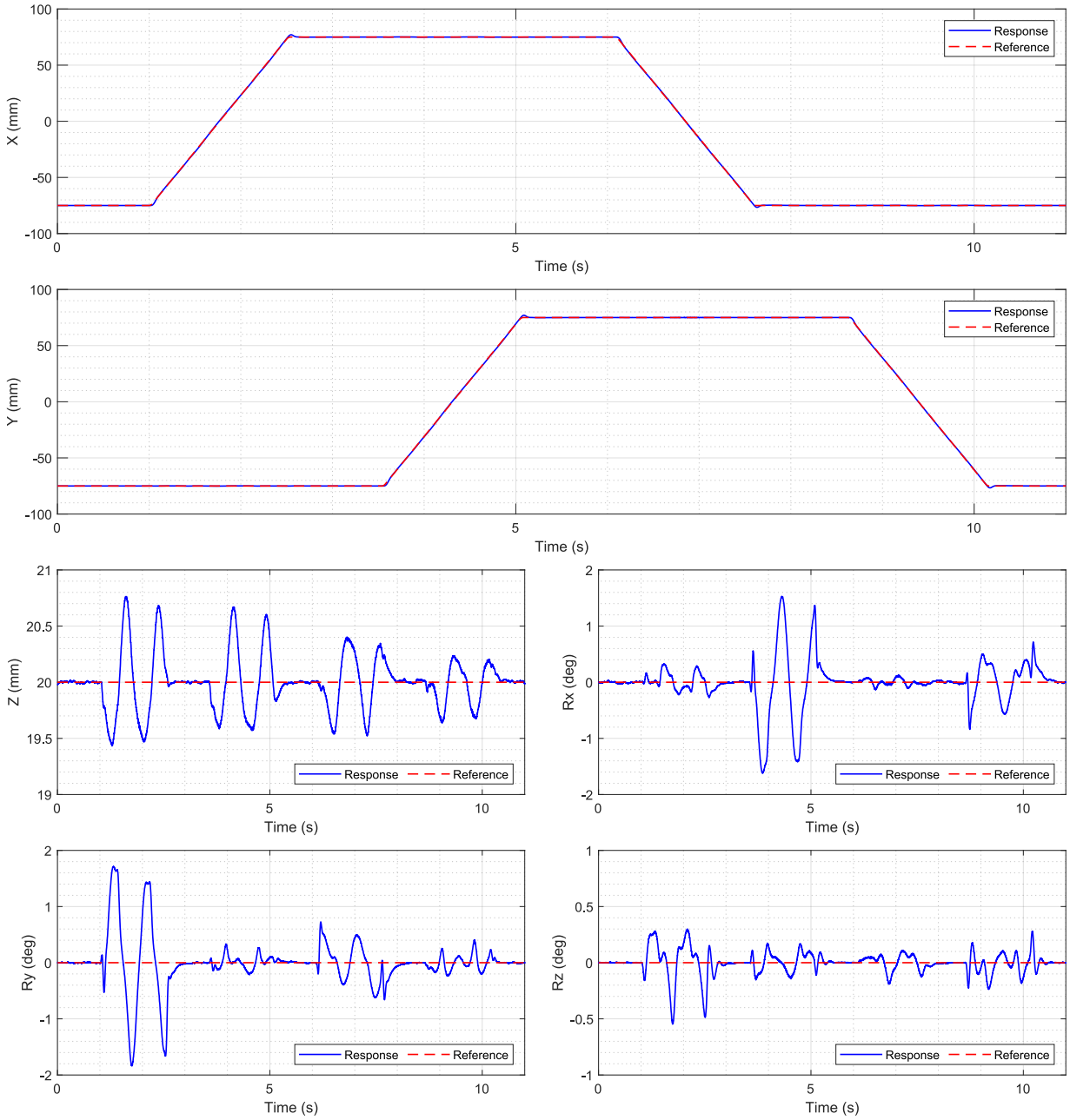


Figure 7.17: Proto-MagFloor four 2-inch PM experiment results 4: ±75 mm XY-plane long-range motion.

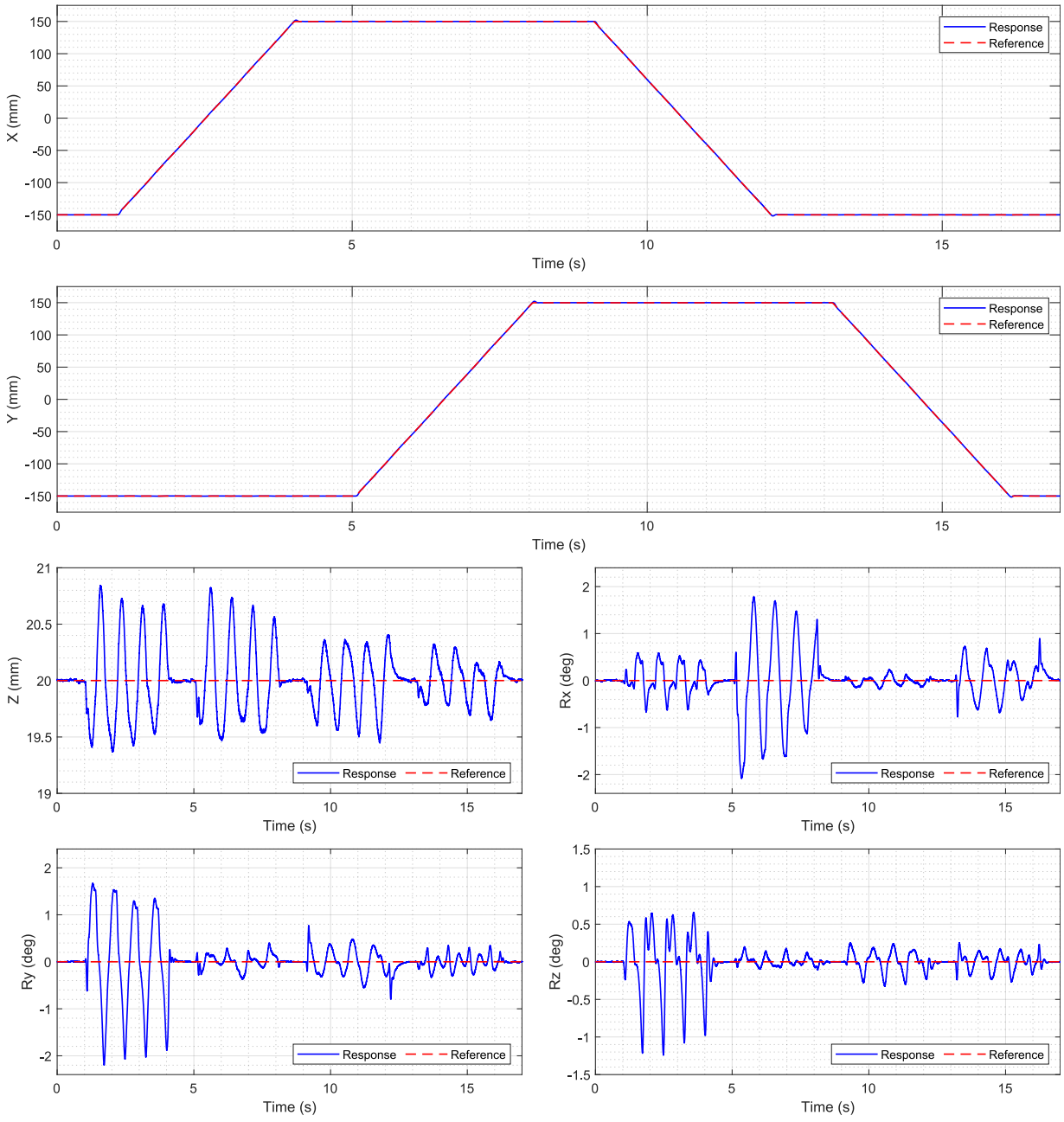


Figure 7.18: Proto-MagFloor four 2-inch PM experiment results 5: ±150 mm XY-plane long-range motion.

Full-Range Rotation: Roll and Pitch

To avoid the mover colliding with the coil array surface when the mover levitates at the maximum roll or pitch angle, the mover center is levitated to z = 30 mm before rotation. For roll and pitch rotation, two experiments were conducted: full-range rotation with ramp command and in-place rotation.

The first experiment is full-range rotation with ramp command as shown in Fig. 7.19. The mover first moves with roll angle for ±10 degrees then moves with pitch angle for ±10 degrees. The results demonstrate good command tracking performance for roll and pitch rotation. For other DOF, the x and y axis error are within ±0.03 mm, and ±0.025 mm for z axis. The yaw rotation error is within ±0.02 degrees.

Second, the mover is rotated in-place with ±10 degrees in both roll and pitch as shown in Fig. 7.20. The command tracking results demonstrate good tracking performance. The responses in other DOF are larger than the ramp command experiment. The errors in x and y axis are ±0.06 mm, ±0.125 mm for z axis,and ±0.2 degrees for yaw rotation.

Full-Range Rotation: Yaw

For yaw rotation, the analysis of the multiple-disc magnet mover design demonstrated that the mover can become unstable when the mover rotates at the central region of the coil array which consumes a high current. In this experiment, therefore, the mover is moved to (x, y) = (38.1, 0) at z = 16 mm before rotation. Then, the mover is controlled to rotate about the vertical axis from 0 to 360 degrees with an angular speed of 180 deg/s.

The full-range yaw rotation experiment was conducted with a yaw rotation speed of 180 deg/s. Figure 7.21 represents the yaw rotation result and error. Even though the mover was not rotated at the central region of the active coil array, large periodic errors of ±4 degrees in yaw motion can be observed at certain yaw angles.

Meanwhile, large errors in other DOF during the full-range yaw rotation can be observed in Fig. 7.22. In translation, several spikes occur in all axes periodically. For roll and pitch rotation, the error range is within ±1.5 degrees.

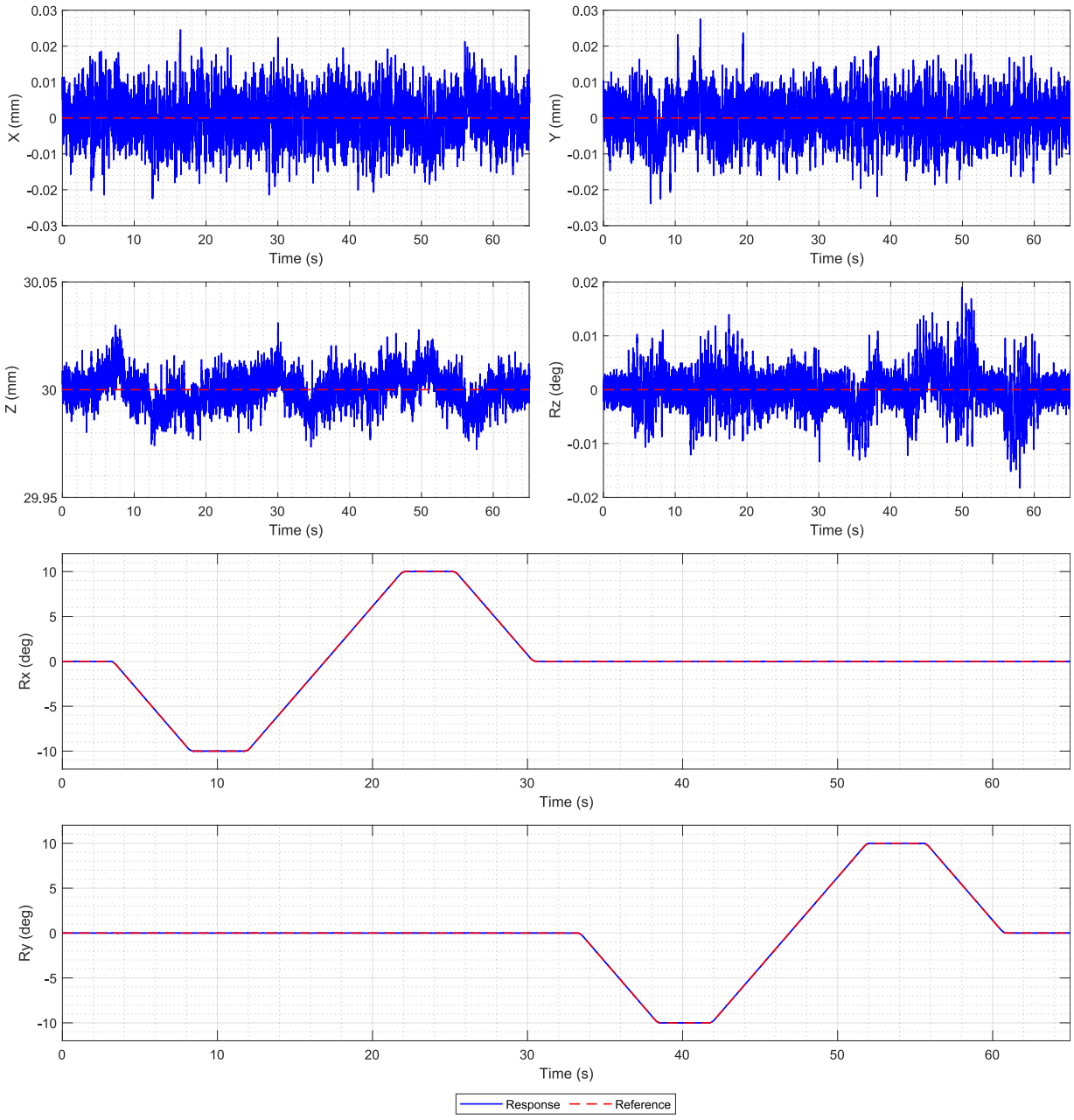


Figure 7.19: Proto-MagFloor four 2-inch PM experiment results 6: ±10 degrees Roll and Pitch full-range motion.

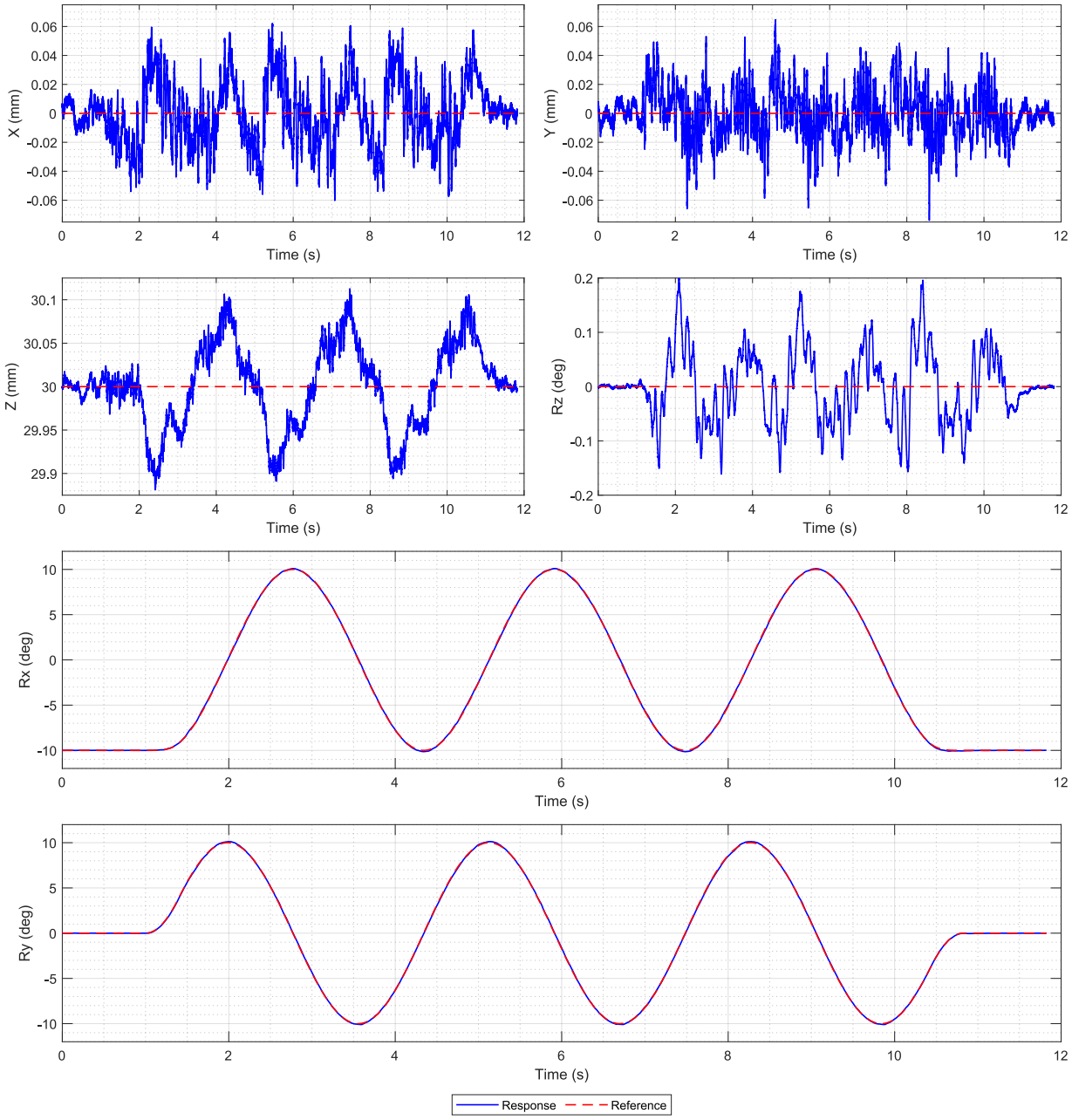


Figure 7.20: Proto-MagFloor four 2-inch PM experiment results 7: ±10 degrees Roll and Pitch in-place rotation.

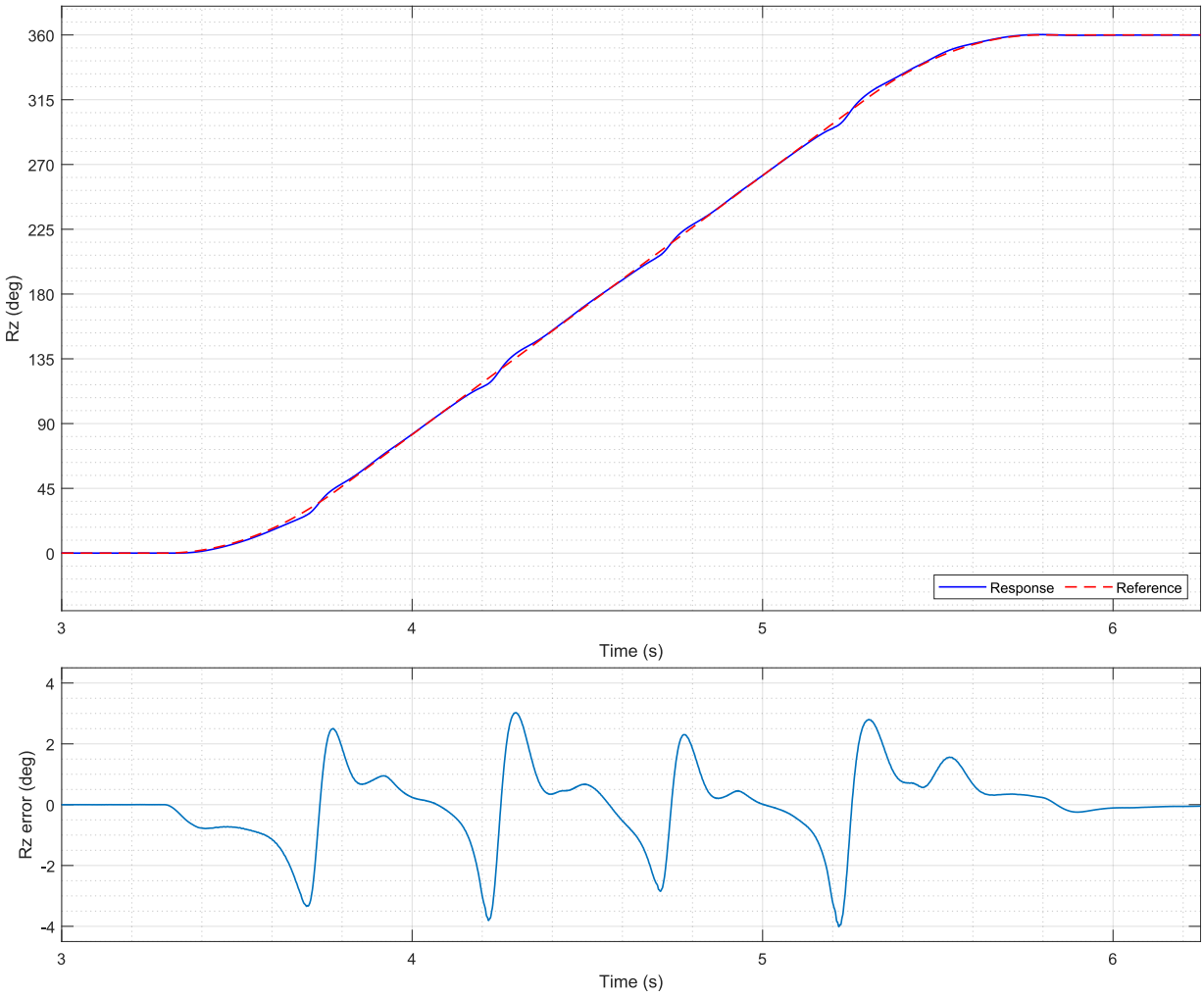


Figure 7.21: Proto-MagFloor four 2-inch PM experiment results 8: 360 degrees Yaw rotation with angular speed of 180 deg/s.

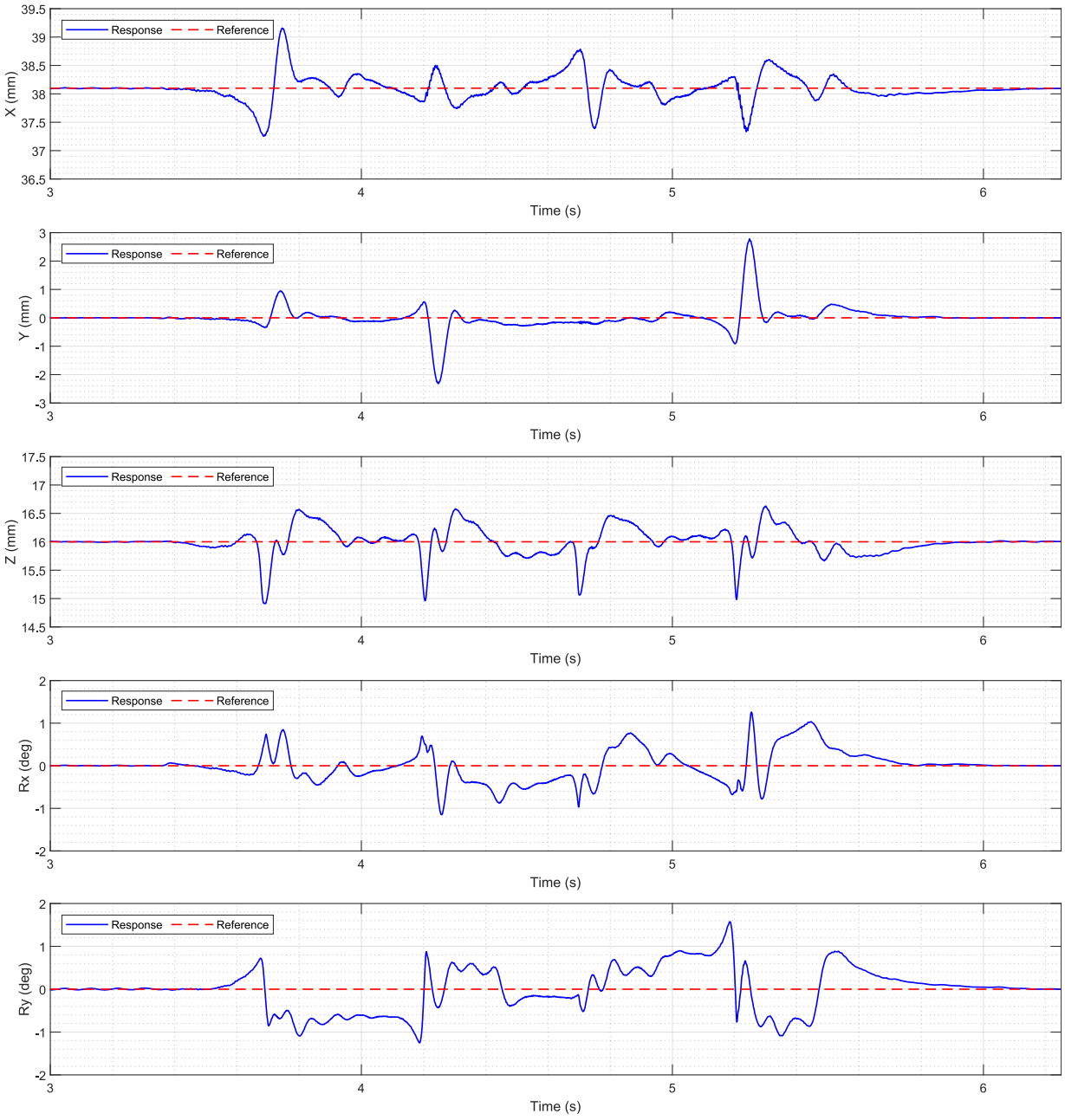


Figure 7.22: Proto-MagFloor four 2-inch PM experiment results 8: Other DOF responses.

7.4 Summary

This chapter presents implementation and levitation experiments on the planar maglev prototype, Proto-MagFloor, with a single 4-inch magnet mover and a four 2-inch magnet mover. By using lookup table method, the decoupling performance when the mover is levitated at the middle of the lookup data, especially roll and pitch rotations. With an implementation of the multivariate linear interpolation, the decoupling performance was significantly enhanced. The decoupling strategy for long-range levitation was successfully implemented for both movers.

Chapter 8

Conclusions

8.1 Conclusions

In this thesis, the modular planar maglev system has been developed. The design of this system aims to enhance the flexibility of modern smart manufacturing. The system has a modular coil array and disc magnet mover. The experiments conducted in this thesis demonstrated a proof-of-concept for the maglev-based omnidirectional conveyor system.

Modular Planar Magnetic Levitation Stator Design

The developed novel planar maglev system is based on the Lorentz force principle or Lorentz levitation. First, the Lorentz force and torque or wrench model between a single-disc magnet and a single coil was introduced in Chapter 3. The magnetic nodes method and Gaussian quadrature technique were used to simplify the model computation.

The cross-coupling effect in the maglev system can be formulated by the wrench matrix, which contains forces and torques from each coil to the magnet mover. One solution to the cross-coupling effect is using a wrench–current decoupling matrix. The decoupling matrix is a pseudoinverse of the wrench matrix.

The design of the modular planar maglev stator was described in Chapter 4. The stator consists of a coil array and modular support structure. Square coil dimensions were designed and optimized by the Fabry factor and vertical levitation force. Electrical power distribution and amplifiers are installed inside the support structure. The Maglev Floor

system was built in RoboHub. In addition, two planar maglev prototypes, 10-Coil Testbed and Maglev Floor Prototype (Proto-MagFloor), were built for pilot testing.

Disc-Magnet Mover Design

Analysis and design of the disc-magnet mover were described in Chapter 5. For a single-disc magnet, an analysis of the condition numbers of the wrench matrices between the coil array and the disc magnet indicated that the disc magnet with a comparable or larger diameter than the coil tends to have lower condition numbers, in other words, better controllability.

For a multiple-disc magnet mover, the mover comprises four 2-inch disc magnets. The layout of the magnets was optimized by considering condition number, maximum current, and total power consumption. Subsequent analysis of the mover with various yaw angles revealed the central region is not suitable for yaw rotation due to the high current required.

Wrench–Current Decoupling Enhancement Using Multivariate Linear Interpolation

With discrete data in the lookup table, the decoupling performance can deteriorate when the mover levitates in the middle of two data states and cause the switching problem. A multivariate linear interpolation was used to estimate the wrench–current decoupling matrix at any mover poses within the data range.

An implementation of the 5-DOF and 6-DOF linear interpolation was demonstrated in Chapters 6 and 7. With interpolation, large oscillations due to the switching problem can be eliminated. This technique significantly enhances the decoupling performance.

Wrench–Current Decoupling Strategy for Long-Range Planar Motion

For long-range planar motion, the decoupling strategy using short-range lookup data was introduced in Chapter 3. The lookup data has the range of quarter coil area. The active coil set is selected from the mover location. Then, the wrench–current decoupling matrix is estimated from lookup data and relative mover pose.

An implementation of the decoupling strategy for long-range levitation on the Proto-MagFloor was presented in Chapter 7. This strategy was successfully applied to both single-disc and multiple-disc magnet movers.

8.2 Future Works

This research developed a novel modular planar magnetic levitation system, including a wrench model, stator, mover, and levitation enhancement techniques. From system evaluation, there are still many development opportunities for future works as follows:

The first part is the development of the planar maglev system.

- Even though the lookup table method can be applied for real-time decoupling, a real-time wrench model for disc magnet mover is still required. With the real-time model, the decoupling matrix can be computed at any mover pose similar to the Halbach array with the harmonic model [95–98].
- The modular planar electromagnet stator can be redesigned to be more compact. For example, a smaller coil allows the designer to use a smaller disc magnet for the mover to maintain controllability. Several commercial products can be replaced by customized components with a dedicated design for the system to reduce space usage.
- The camera vision system has the advantage of motion tracking for large levitation areas. However, the setup time is long and the feedback is inconsistent for each operation. Therefore, the embedded motion tracking sensor such as a hall effect sensor [99] is more suitable. The design of the embedded sensor circuit unit is required.
- A multiple-disc magnet mover, which was designed in this work, can be controlled with six degrees of freedom. However, the levitation performance must be improved, especially yaw rotation. An alternative design of the multiple-disc magnet is required.

After the development of the system, the system implementation for real-world applications should be evaluated.

- The original purpose of this system is to be used for industrial material handling as the omnidirectional conveyor. Hence, the development of advanced algorithms for motion planning or payload variation can increase the flexibility of the smart manufacturing system.
- With precision motion, the system can operate as a multi-DOF precision stage for high-precision machining [100] or laboratory microscopy.
- Since this system can provide non-contact motion, this system is also applicable to clean room applications where particle control is required.
- Meanwhile, the system can be applied to robotics. The system is expected to perform collaborative tasks with other movers, machines, or robots.

References

[1] F. S. Fogliatto, G. J. C. da Silveira, and D. Borenstein, "The mass customization decade: An updated review of the literature," *International Journal of Production Economics*, vol. 138, no. 1, pp. 14–25, 2012.

[2] A. Radziwon, A. Bilberg, M. Bogers, and E. S. Madsen, "The smart factory: Exploring adaptive and flexible manufacturing solutions," *Procedia Engineering*, vol. 69, pp. 1184–1190, 2014, 24th DAAAM International Symposium on Intelligent Manufacturing and Automation, 2013.

[3] J. Browne, D. Dubois, K. Rathmill, S. P. Sethi, and K. E. Stecke, "Classification of flexible manufacturing systems," *The FMS magazine*, vol. 2, pp. 114–117, 1984.

[4] A. K. Sethi and S. P. Sethi, "Flexibility in manufacturing: A survey," *International Journal of Flexible Manufacturing Systems*, vol. 2, pp. 289–328, 1990.

[5] cellumation. Cellular conveyor, celluveyor. [Online]. Available: https://cellumation.com/products/celluveyor

[6] M. Lütjen, M. Teucke, M. Isenberg, H. Thamer, C. Uriarte, and S. Kunaschk, "Design of SmartGate technologies for enhanced material handling," *International Journal of Advanced Logistics*, vol. 2, no. 1, pp. 26–37, 2013.

[7] C. Uriarte, A. Asphandiar, H. Thamer, A. Benggolo, and M. Freitag, "Control strategies for small-scaled conveyor modules enabling highly flexible material flow systems," *Procedia CIRP*, vol. 79, p. 433–438, 2019.

[8] OMRON. Autonomous mobile robot. [Online]. Available: https://industrial.omron.eu/en/products/autonomous-mobile-robot

[9] H.-W. Lee, K.-C. Kim, and J. Lee, "Review of maglev train technologies," *IEEE Transactions on Magnetics*, vol. 42, no. 7, pp. 1917–1925, 2006.

[10] J. K. Nøland, "Prospects and challenges of the hyperloop transportation system: A systematic technology review," *IEEE Access*, vol. 9, pp. 28 439–28 458, 2021.

[11] SCMAGLEV. SCMAGLEV: Superconducting Maglev. [Online]. Available: https://www.scmaglev.com/

[12] J. J. Abbott, E. Diller, and A. J. Petruska, "Magnetic methods in robotics," *Annual Review of Control, Robotics, and Autonomous Systems*, vol. 3, no. 1, pp. 57–90, 2020.

[13] C. Elbuken, M. B. Khamesee, and M. Yavuz, "Eddy current damping for magnetic levitation: downscaling from macro- to micro-levitation," *Journal of Physics D: Applied Physics*, vol. 39, no. 18, pp. 3932–3938, 2006.

[14] M. P. Kummer, J. J. Abbott, B. E. Kratochvil, R. Borer, A. Sengul, and B. J. Nelson, "OctoMag: An electromagnetic system for 5-DOF wireless micromanipulation," *IEEE Transactions on Robotics*, vol. 26, no. 6, pp. 1006–1017, 2010.

[15] P. Kazemzadeh Heris and M. B. Khamesee, "Design and fabrication of a magnetic actuator for torque and force control estimated by the ANN/SA algorithm," *Micromachines*, vol. 13, no. 2, 2022.

[16] D. Craig and M. B. Khamesee, "Motion control of a large gap magnetic suspension system for microrobotic manipulation," *Journal of Physics D: Applied Physics*, vol. 40, no. 11, pp. 3277–3285, 2007.

[17] X. Zhang and M. B. Khamesee, "Adaptive force tracking control of a magnetically navigated microrobot in uncertain environment," *IEEE/ASME Transactions on Mechatronics*, vol. 22, no. 4, pp. 1644–1651, 2017.

[18] J. Kim, H. Choi, and J. Kim, "A robust motion control with antiwindup scheme for electromagnetic actuated microrobot using time-delay estimation," *IEEE/ASME Transactions on Mechatronics*, vol. 24, no. 3, pp. 1096–1105, 2019.

[19] T. Xu, J. Zhang, M. Salehizadeh, O. Onaizah, and E. Diller, "Millimeter-scale flexible robots with programmable three-dimensional magnetization and motions," *Science Robotics*, vol. 4, no. 29, p. eaav4494, 2019.

[20] A. Lim, A. Schonewille, C. Forbrigger, T. Looi, J. Drake, and E. Diller, "Design and comparison of magnetically-actuated dexterous forceps instruments for neuroendoscopy," *IEEE Transactions on Biomedical Engineering*, vol. 68, no. 3, pp. 846–856, 2021.

[21] P. Berkelman and M. Dzadovsky, "Extending the motion ranges of magnetic levitation for haptic interaction," in *World Haptics 2009 - Third Joint EuroHaptics conference and Symposium on Haptic Interfaces for Virtual Environment and Teleoperator Systems*, 2009, pp. 517–522.

[22] S. A. Pedram, R. L. Klatzky, and P. Berkelman, "Torque contribution to haptic rendering of virtual textures," *IEEE Transactions on Haptics*, vol. 10, no. 4, pp. 567–579, 2017.

[23] S. Aghajani Pedram, R. Klatzky, O. Isaac-Lowry, and P. Berkelman, "Virtual roughness perception using coil array magnetic levitation haptic interface: Effects of torque feedback," in *Haptics: Neuroscience, Devices, Modeling, and Applications*. Berlin, Heidelberg: Springer Berlin Heidelberg, 2014, pp. 513–520.

[24] M. Mehrtash, N. Tsuda, and M. B. Khamesee, "Bilateral macro–micro teleoperation using magnetic levitation," *IEEE/ASME Transactions on Mechatronics*, vol. 16, no. 3, pp. 459–469, 2011.

[25] A. Smirnov, N. Uzhegov, T. Sillanpää, J. Pyrhönen, and O. Pyrhönen, "High-speed electrical machine with active magnetic bearing system optimization," *IEEE Transactions on Industrial Electronics*, vol. 64, no. 12, pp. 9876–9885, 2017.

[26] S. Wang, H. Li, D. Yuan, S. Wang, S. Wang, T. Zhu, and J. Zhu, "Oscillations and size control of Titanium droplet for electromagnetic levitation melting," *IEEE Transactions on Magnetics*, vol. 54, no. 3, pp. 1–4, 2018.

[27] M. Moghani and M. R. Kermani, "A lightweight magnetorheological actuator using hybrid magnetization," *IEEE/ASME Transactions on Mechatronics*, vol. 25, no. 1, pp. 76–83, 2020.

[28] S. Pisetskiy and M. Kermani, "High-performance magneto-rheological clutches for direct-drive actuation: Design and development," *Journal of Intelligent Material Systems and Structures*, vol. 32, no. 20, pp. 2582–2600, 2021.

[29] P. Kumar, S. Malik, E. Toyserkani, and M. B. Khamesee, "Development of an electromagnetic micromanipulator levitation system for metal additive manufacturing applications," *Micromachines*, vol. 13, no. 4, 2022.

[30] H. E. Farag, E. Toyserkani, and M. B. Khamesee, "Non-destructive testing using eddy current sensors for defect detection in additively manufactured titanium and stainless-steel parts," *Sensors*, vol. 22, no. 14, 2022.

[31] L. Zhou and J. Wu, "Magnetic levitation technology for precision motion systems: A review and future perspectives," *International Journal of Automation Technology*, vol. 16, no. 4, pp. 386–402, 2022.

[32] N. Arora, M. U. Khan, L. Petit, F. Lamarque, and C. Prelle, "Design and development of a planar electromagnetic conveyor for the microfactory," *IEEE/ASME Transactions on Mechatronics*, vol. 24, no. 4, pp. 1723–1731, 2019.

[33] Planar Motor Inc. Planar Motor System. [Online]. Available: http://www.planarmotor.com

[34] Beckhoff Automation GmbH & Co. KG. XPlanar: Planar motor system. [Online]. Available: https://www.beckhoff.com/en-en/products/motion/xplanar-planar-motor-system

[35] Bosch Rexroth AG. ctrlX FLOW^{6D}: The planar system with 6 six dimensions. [Online]. Available: https://apps.boschrexroth.com/microsites/ctrlx-automation/en/portfolio/ctrlx-flow

[36] B&R Industrial Automation GmbH. ACOPOS 6D. [Online]. Available: https://www.br-automation.com/en-ca/products/mechatronic-systems/acopos-6d

[37] B. V. Jayawant, "Electromagnetic suspension and levitation techniques," *Proc. Royal Soc Lond. A, Math. Phys. Sci.*, vol. 416, pp. 245–320, 1988.

[38] R. L. Hollis and S. E. Salcudean, "Lorentz levitation technology: a new approach to fine motion robotics, teleoperation, haptic interfaces, and vibration isolation," in *International Symposium on Robotics Research*, 1993.

[39] W.-J. Kim and D. L. Trumper, "High-precision magnetic levitation stage for photolithography," *Precision Engineering*, vol. 22, no. 2, p. 66–77, 1998.

[40] X. Shan, S.-K. Kuo, J. Zhang, and C.-H. Menq, "Ultra precision motion control of a multiple degrees of freedom magnetic suspension stage," *IEEE/ASME Transactions on Mechatronics*, vol. 7, no. 1, pp. 67–78, 2002.

[41] J. C. Compter, "Electro-dynamic planar motor," *Precision Engineering*, vol. 28, no. 2, pp. 171–180, 2004.

[42] W.-J. Kim, N. Bhat, and T. Hu, "Integrated multidimensional positioner for precision manufacturing," *Proceedings of the Institution of Mechanical Engineers, Part B: Journal of Engineering Manufacture*, vol. 218, no. 4, pp. 431–442, 2004.

[43] S. Verma, W.-J. Kim, and H. Shakir, "Multi-axis maglev nanopositioner for precision manufacturing and manipulation applications," *IEEE Transactions on Industry Applications*, vol. 41, no. 5, pp. 1159–1167, 2005.

[44] Y. Lai, Y. Lee, and J. Yen, "Design and servo control of a single-deck planar maglev stage," *IEEE Transactions on Magnetics*, vol. 43, no. 6, pp. 2600–2602, 2007.

[45] W.-J. Kim, S. Verma, and H. Shakir, "Design and precision construction of novel magnetic-levitation-based multi-axis nanoscale positioning systems," *Precision Engineering*, vol. 31, no. 4, pp. 337–350, 2007.

[46] J. W. Jansen, C. M. M. van Lierop, E. A. Lomonova, and A. J. A. Vandenput, "Magnetically levitated planar actuator with moving magnets," *IEEE Transactions on Industry Applications*, vol. 44, no. 4, pp. 1108–1115, 2008.

[47] P. Berkelman and M. Dzadovsky, "Single magnet levitation by repulsion using a planar coil array," in *2008 IEEE International Conference on Control Applications*, 2008, pp. 108–113.

[48] X. Lu and I. Usman, "6D direct-drive technology for planar motion stages," *CIRP Annals Manuf. Technol.*, vol. 61, no. 1, pp. 359 – 362, 2012.

[49] P. Berkelman and M. Dzadovsky, "Magnetic levitation over large translation and rotation ranges in all directions," *IEEE/ASME Transactions on Mechatronics*, vol. 18, no. 1, pp. 44–52, 2013.

[50] M. Miyasaka and P. Berkelman, "Magnetic levitation with unlimited omnidirectional rotation range," *Mechatronics*, vol. 24, no. 3, pp. 252–264, 2014.

[51] C. Schaeffel, M. Katzschmann, H. Mohr, R. Gloess, C. Rudolf, C. Mock, and C. Walenda, "6D planar magnetic levitation system - PIMag 6D," *Mechanical Engineering Journal*, vol. 3, no. 1, pp. 15–00 111–15–00 111, 2016.

[52] F. Xu, X. Xu, and M. Chen, "Prototype of 6-DOF magnetically levitated stage based on single axis Lorentz force actuator," *Journal of Electrical Engineering and Technology*, vol. 11, no. 5, p. 1216–1228, 2016.

[53] H. Zhu, T. J. Teo, and C. K. Pang, "Design and modeling of a six-degree-of-freedom magnetically levitated positioner using square coils and 1-D Halbach arrays," *IEEE Transactions on Industrial Electronics*, vol. 64, no. 1, pp. 440–450, 2017.

[54] M. Dyck, X. Lu, and Y. Altintas, "Magnetically levitated rotary table with six degrees of freedom," *IEEE/ASME Transactions on Mechatronics*, vol. 22, no. 1, pp. 530–540, 2017.

[55] F. Xu, R. Peng, T. Zheng, and X. Xu, "Development and validation of numerical magnetic force and torque model for magnetically levitated actuator," *IEEE Transactions on Magnetics*, vol. 55, no. 1, pp. 1–9, 2019.

[56] H. Zhu, T. J. Teo, and C. K. Pang, "Magnetically levitated parallel actuated dual-stage (Maglev-PAD) system for six-axis precision positioning," *IEEE/ASME Transactions on Mechatronics*, vol. 24, no. 4, pp. 1829–1838, 2019.

[57] R. Gloess and A. Goos, "Magnetic levitation stages for planar and linear scan application with nanometer resolution," *International Journal of Applied Electromagnetics and Mechanics*, vol. 63, no. 1, p. 105–117, 2020.

[58] M. Takahashi, H. Ogawa, and T. Kato, "Compact maglev stage system for nanometer-scale positioning," *Precision Engineering*, vol. 66, pp. 519–530, 2020.

[59] T. Hu and W.-J. Kim, "Extended range six-DOF high-precision positioner for wafer processing," *IEEE/ASME Transactions on Mechatronics*, vol. 11, no. 6, pp. 682–689, 2006.

[60] H. Shakir and W.-J. Kim, "Nanoscale path planning and motion control with maglev positioners," *IEEE/ASME Transactions on Mechatronics*, vol. 11, no. 5, pp. 625–633, 2006.

[61] W.-J. Kim and H. Maheshwari, "High-precision control of a maglev linear actuator with nanopositioning capability," in *Proceedings of the 2002 American Control Conference (IEEE Cat. No.CH37301)*, vol. 5, 2002, pp. 4279–4284 vol.5.

[62] S.-K. Kuo, X. Shan, and C.-H. Menq, "Large travel ultra precision x-y-θ motion control of a magnetic-suspension stage," *IEEE/ASME Transactions on Mechatronics*, vol. 8, no. 3, pp. 334–341, 2003.

[63] J. W. Jansen, "Magnetically levitated planar actuator with moving magnets : electromechanical analysis and design," Ph.D. dissertation, Eindhoven University of Technology, Eindhoven, Netherlands, 2007.

[64] I. Usman and X. Lu, "Force ripple attenuation of 6-DOF direct drive permanent magnet planar levitating synchronous motors," *IEEE Transactions on Magnetics*, vol. 51, no. 12, pp. 1–8, 2015.

[65] I. Usman, "Long stroke magnetic levitation planar stages," Ph.D. dissertation, University of British Columbia, Vancouver, Canada, 2015.

[66] M. Dyck, "Magnetically levitated six degree of freedom micro-machining rotary table," Master's thesis, University of British Columbia, Vancouver, Canada, 2014.

[67] R. Gloess, "Mag-6D a new mechatronics design of a levitation stage with nanometer resolution," in *Proceedings of the 31st ASPE Annual Meeting 2016*, 2016, pp. 423–427.

[68] H. Zhu, T. J. Teo, and C. K. Pang, "Conceptual design and modeling of a six degrees-of-freedom unlimited stroke magnetically levitated positioner," in *2014 IEEE/ASME International Conference on Advanced Intelligent Mechatronics*, 2014, pp. 1569–1574.

[69] X. Li, H. Zhu, J. Ma, T. J. Teo, C. S. Teo, M. Tomizuka, and T. H. Lee, "Data-driven multiobjective controller optimization for a magnetically levitated nanopositioning system," *IEEE/ASME Transactions on Mechatronics*, vol. 25, no. 4, pp. 1961–1970, 2020.

[70] T. J. Teo, H. Zhu, and C. K. Pang, "Modeling of a two degrees-of-freedom moving magnet linear motor for magnetically levitated positioners," *IEEE Transactions on Magnetics*, vol. 50, no. 12, pp. 1–12, 2014.

[71] H. Zhu, C. K. Pang, and T. J. Teo, "Analysis and control of a 6 DOF maglev positioning system with characteristics of end-effects and eddy current damping," *Mechatronics*, vol. 47, pp. 183–194, 2017.

[72] H. Zhu, T. J. Teo, and C. K. Pang, "Flexure-based magnetically levitated dual-stage system for high-bandwidth positioning," *IEEE Transactions on Industrial Informatics*, vol. 15, no. 8, pp. 4665–4675, 2019.

[73] P. Berkelman and M. Dzadovsky, "Large motion range magnet levitation using a planar array of coils," in *2009 IEEE International Conference on Robotics and Automation*, 2009, pp. 1609–1610.

[74] P. Berkelman and M. Dzadovsky, "Magnet levitation and trajectory following motion control using a planar array of cylindrical coils," in *ASME 2008 Dynamic Systems and Control Conference*, 2008, pp. 767–774.

[75] P. Berkelman and M. Dzadovsky, "Novel design, characterization, and control method for large motion range magnetic levitation," *IEEE Magnetics Letters*, vol. 1, pp. 0 500 104–0 500 104, 2010.

[76] P. Berkelman and Y.-S. Lu, "Long range six degree-of-freedom magnetic levitation using low cost sensing and control," *Journal of Robotics and Mechatronics*, vol. 32, no. 3, pp. 683–691, 2020.

[77] M. Miyasaka, "Modeling, analysis, and design for magnetic levitation with unlimited roll and pitch rotations and a pen-shaped haptic interface handle," Master's thesis, University of Hawaii at Manoa, Honolulu, HI, 2012.

[78] X. Lu, P. Tang, A. H. Slocum, and R. Chen, "Robotic devices and methods for fabrication, use and control of same," Patent WO2018/176 137Al, Oct 4, 2018.

[79] U. P. L. Bentfeld and R. Brinkmann, "Planar drive system, stator module and sensor module," Patent WO2019/129 561Al, Jul. 4, 2019.

[80] C. Fabry, "Sur le champ magnétique au centre d'une bobine cylindrique et la construction des bobines de galvanomètres," *La Lumière électrique*, vol. 17, pp. 133–141, 1898.

[81] D. B. Montgomery, *Solenoid magnet design.* New York: Wiley-Interscience, 1969, p. 6.

[82] J. Hagedorn, F. S.-L. Blanc, and J. Fleischer, Eds., *Handbook of coil winding.* Berlin: Springer Vieweg, 2018, p. 147.

[83] E. P. Furlani, *Permanent magnet and electromechanical devices: materials, analysis, and applications.* San Diego, CA: Academic, 2001.

[84] H. Allag and J.-P. Yonnet, "3-D analytical calculation of the torque and force exerted between two cuboidal magnets," *IEEE Transactions on Magnetics*, vol. 45, no. 10, pp. 3969–3972, 2009.

[85] J. W. Jansen, J. P. C. Smeets, T. T. Overboom, J. M. M. Rovers, and E. A. Lomonova, "Overview of analytical models for the design of linear and planar motors," *IEEE Transactions on Magnetics*, vol. 50, no. 11, pp. 1–7, 2014.

[86] G. Akoun and J.-P. Yonnet, "3D analytical calculation of the forces exerted between two cuboidal magnets," *IEEE Transactions on Magnetics*, vol. 20, no. 5, pp. 1962–1964, 1984.

[87] E. P. Furlani, "A formula for the levitation force between magnetic disks," *IEEE Transactions on Magnetics*, vol. 29, no. 6, pp. 4165–4169, 1993.

[88] F. Bancel, "Magnetic nodes," *Journal of Physics D: Applied Physics*, vol. 32, no. 17, pp. 2155–2161, 1999.

[89] J.-P. Yonnet and H. Allag, "Three-dimensional analytical calculation of permanent magnet interactions by "magnetic node" representation," *IEEE Transactions on Magnetics*, vol. 47, no. 8, pp. 2050–2055, 2011.

[90] F. Xu, Y. Lv, X. Xu, and V. Dinavahi, "FPGA-based real-time wrench model of direct current driven magnetic levitation actuator," *IEEE Transactions on Industrial Electronics*, vol. 65, no. 12, pp. 9635–9645, 2018.

[91] X. Zhang, C. Trakarnchaiyo, H. Zhang, and M. B. Khamesee, "Magtable: A tabletop system for 6-DOF large range and completely contactless operation using magnetic levitation," *Mechatronics*, vol. 77, p. 102600, 2021.

[92] S. C. Chapra and R. P. Canale, *Numerical Methods for Engineers*, 6th ed. McGraw-Hill Education, 2010.

[93] C. Trakarnchaiyo, Y. Wang, and M. B. Khamesee, "Design of a compact planar magnetic levitation system with wrench–current decoupling enhancement," *Applied Sciences*, vol. 13, no. 4, 2023.

[94] C. Stewart, "Implementation of a modular magnetic levitation planar motor," Master's thesis, University of Waterloo, Waterloo, Canada, 2023.

[95] J. de Boeij, E. A. Lomonova, and A. Vandenput, "Modeling ironless permanent-magnet planar actuator structures," *IEEE Transactions on Magnetics*, vol. 42, no. 8, pp. 2009–2016, 2006.

[96] J. W. Jansen, C. M. M. van Lierop, E. A. Lomonova, and A. J. A. Vandenput, "Modeling of magnetically levitated planar actuators with moving magnets," *IEEE Transactions on Magnetics*, vol. 43, no. 1, pp. 15–25, 2007.

[97] J. M. M. Rovers, J. W. Jansen, J. C. Compter, and E. A. Lomonova, "Analysis method of the dynamic force and torque distribution in the magnet array of a commutated magnetically levitated planar actuator," *IEEE Transactions on Industrial Electronics*, vol. 59, no. 5, pp. 2157–2166, 2012.

[98] Z. Xu, X. Zhang, and M. B. Khamesee, "Real-time data-driven force and torque modeling on a 2-D Halbach array by a symmetric coil considering end effect," *IEEE Transactions on Magnetics*, vol. 58, no. 11, pp. 1–10, 2022.

[99] H. Yu and W.-J. Kim, "A compact Hall-effect-sensing 6-DOF precision positioner," *IEEE/ASME Transactions on Mechatronics*, vol. 15, no. 6, pp. 982–985, 2010.

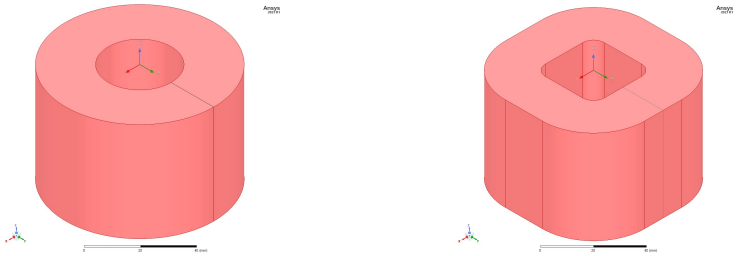
[100] H. Zhou, H. Deng, and J. Duan, "Hybrid fuzzy decoupling control for a precision maglev motion system," *IEEE/ASME Transactions on Mechatronics*, vol. 23, no. 1, pp. 389–401, 2018.

APPENDICES

Appendix A

Simulation Settings

A.1 ANSYS: Cylindrical and Square Coils



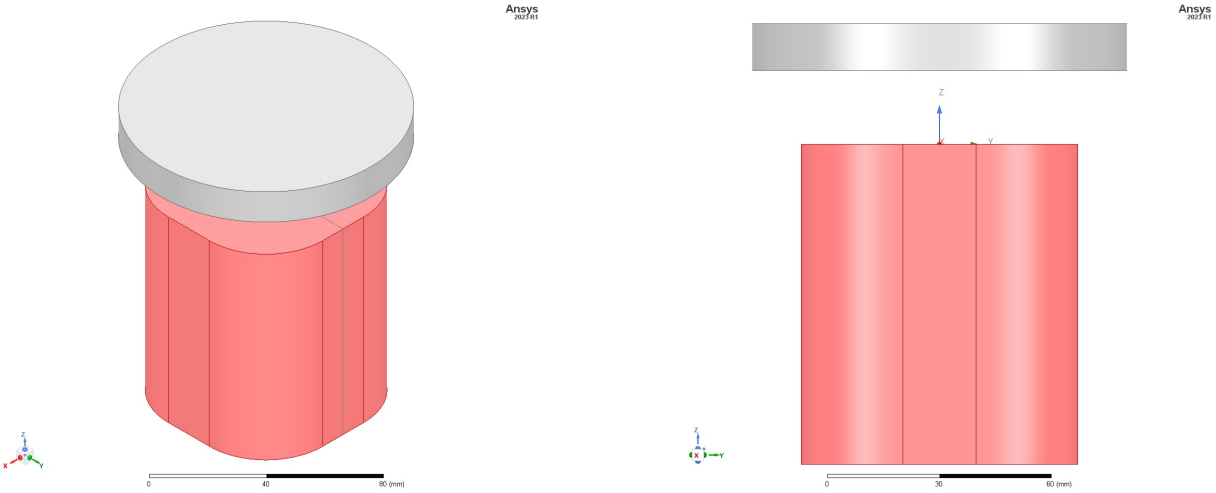
(a) (b)

Figure A.1: ANSYS coil models. **(a)** Cylindrical coil. **(b)** Square coil.

Table A.1: Simulation settings: Comparison between cylindrical and square coils in Figure 4.2.

Maxwell 3D simulation parameters		**Value**	**Unit**
Coil	D_o: Outer width	75.00	mm
(* For square coil)	D_i: Inner width	31.75	mm
	R_o: Outer corner radius *	27.625	mm
	R_i: Inner corner radius *	6.00	mm
	H: Height	50.435	mm
	Current excitation: Stranded, CCW	560	A
Analysis setup	Mesh: Maximum element length	5	mm
	Percent error	0.01	%

A.2 ANSYS: Vertical Force between Disc Magnet and Coil with Different Heights



(a) (b)

Figure A.2: ANSYS single-coil single-disc magnet model. **(a)** Isometric view. **(b)** Front view.

Table A.2: Parametric simulation settings: Vertical force in Figure 4.3.

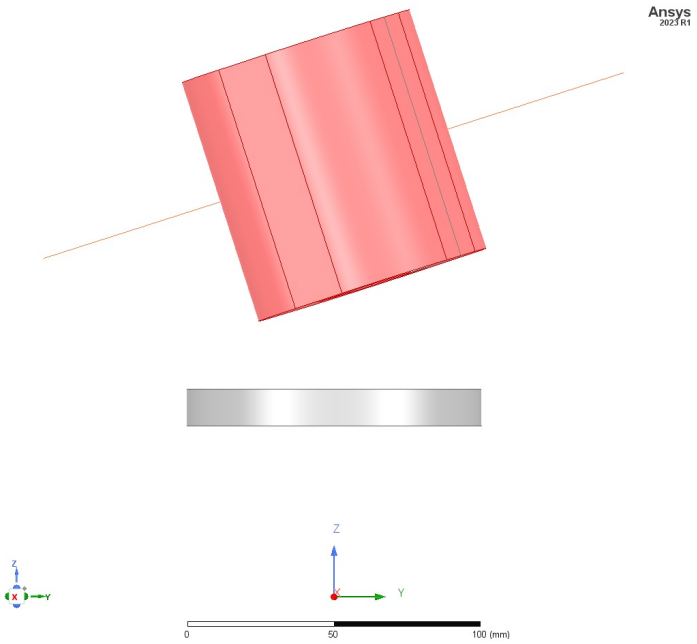
Maxwell 3D parametric simulation parameters		**Value**	**Unit**
Coil	D_o: Outer width	75.00	mm
(* Sweep variable)	D_i: Inner width	31.75	mm
	R_o: Outer corner radius	27.625	mm
	R_i: Inner corner radius	6.00	mm
	d: Magnet wire diameter	1.31	mm
	N_{vert}: Vertical winding turns *	30 : 5 : 90	turns
	H: Height	$d\,(N_{vert}) + 10\%$	mm
	Current excitation: Stranded, CW	960	A
Disc magnet	Diameter	101.6	mm
Neodymium N50	Thickness	12.7	mm
4” dia. × 1/2” thick	μ_r: Relative permeability	1.05	
+Z magnetization	B_r: Remanence	1.45	T
	Vertical gap between magnet and coil	20.0	mm
Analysis setup	Mesh: Length-based element max.	5	mm
	Percent error	0.01	%

A.3 ANSYS: Forces and Torques between Single-Coil Single-Magnet for Wrench Model Validation

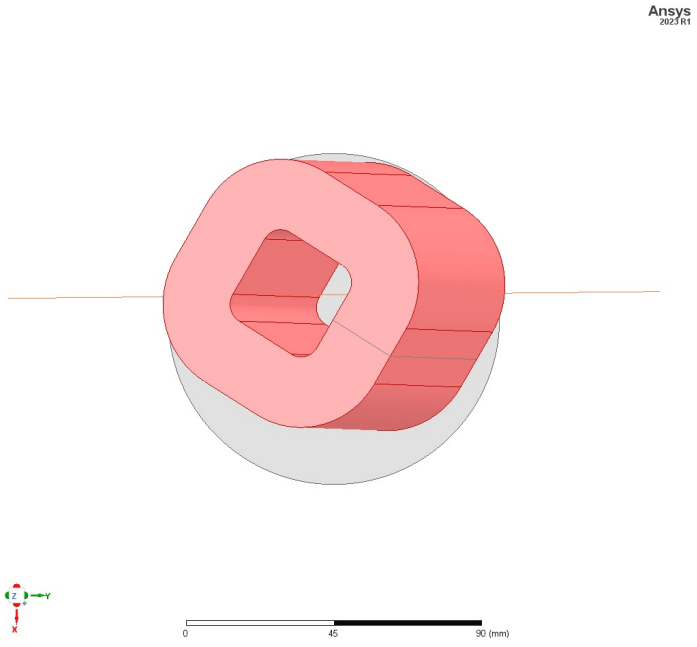
Table A.3: Parametric simulation settings: Forces and torques validation in Figure 3.6b.

Maxwell 3D parametric simulation parameters		**Value**	**Unit**
Coil	D_o: Outer width	75.00	mm
	D_i: Inner width	31.75	mm
	R_o: Outer corner radius	27.625	mm
	R_i: Inner corner radius	6.00	mm
	H: Height	86.46	mm
	Current excitation: Stranded, CCW	4800	A
Disc magnet	Diameter	101.6	mm
Neodymium N50	Thickness	12.7	mm
4" dia. × 1/2" thick	μ_r: Relative permeability	1.05	
+Z magnetization	B_r: Remanence	1.45	T
Path range	X axis (x)	$-0.0105\,y - 7.3772$	mm
(* Sweep variable)	Y axis (y) *	$-100.0 : 10 : 100.0$	mm
	Z axis (z)	$0.3202\,y + 83.4794$	mm
	Roll angle (ψ)	17.8440	degrees
	Pitch angle (θ)	−0.6679	degrees
	Yaw angle (ϕ)	−31.0465	degrees
Experiment setup	Magnet to sensor distance	65.35	mm
Analysis setup	Mesh: Length-based element max.	5	mm
	Percent error	0.01	%

X and Z motion paths are determined from raw motion data using `polyfit` function in MATLAB.



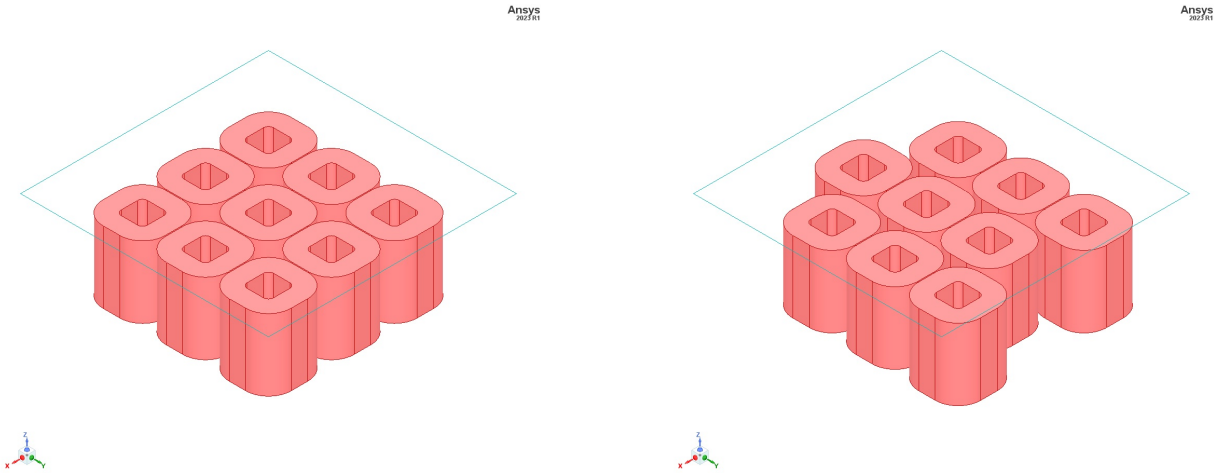
(a)



(b)

Figure A.3: ANSYS measurement setup model with a motion path. **(a)** Front view. **(b)** Top view.

A.4 ANSYS: Straight and Zigzag Coil Array



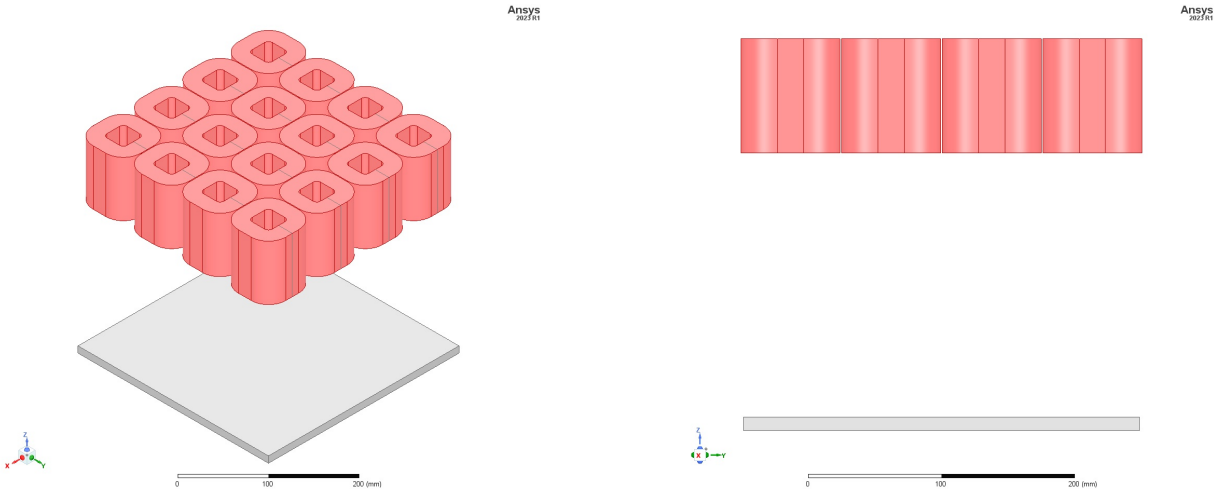
(a) (b)

Figure A.4: ANSYS coil array models. **(a)** Straight configuration. **(b)** Zigzag configuration.

Table A.4: Simulation settings: Array configuration comparison in Figure 4.5.

Maxwell 3D simulation parameters		**Value**	**Unit**
Coil	D_o: Outer width	75.00	mm
	D_i: Inner width	31.75	mm
	R_o: Outer corner radius	27.625	mm
	R_i: Inner corner radius	6.00	mm
	H: Height	86.46	mm
	Current excitation: Stranded, CW	960	A
Array configuration	Coil pitch x (center-to-center)	76.20	mm
	Coil pitch y (center-to-center)	76.20	mm
	Row offset (For zigzag configuration)	38.10	mm
Observation plane	XY plane	300×300	mm^2
	Z	20	mm
Analysis setup	Mesh: Length-based element max.	5	mm
	Percent error	0.1	%

A.5 ANSYS: Coil Array with Steel Sheet



(a) (b)

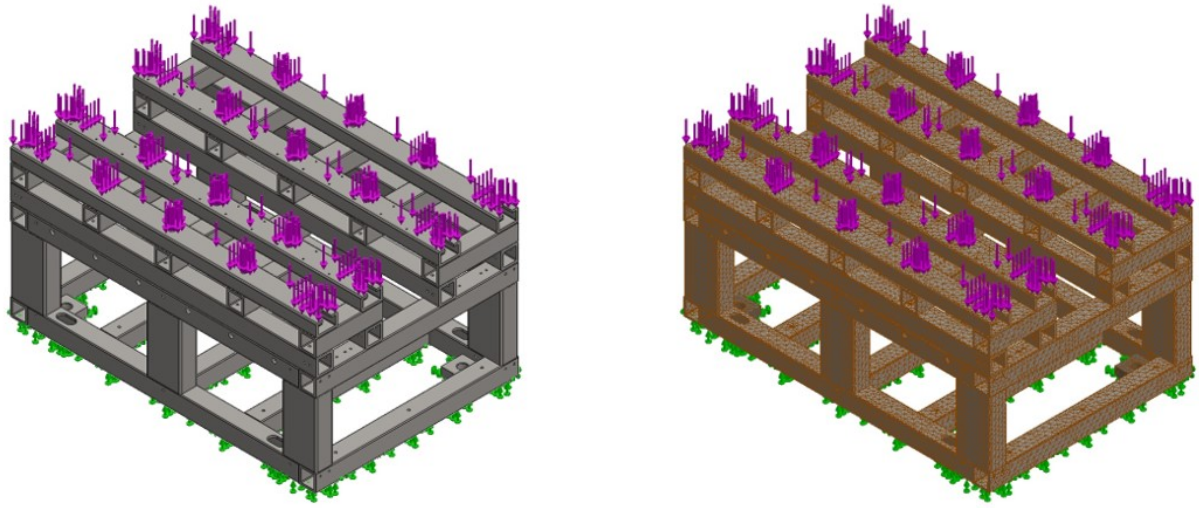
Figure A.5: ANSYS coil array with steel sheet model. **(a)** Isometric view. **(b)** Front view.

Table A.5: Parametric simulation settings: 4-by-4 coil array with steel sheet in Figure 4.8a.

Maxwell 3D parametric simulation parameters		**Value**	**Unit**
Coil	D_o: Outer width	75.00	mm
	D_i: Inner width	31.75	mm
	R_o: Outer corner radius	27.625	mm
	R_i: Inner corner radius	6.00	mm
	H: Height	86.46	mm
	Current excitation: Stranded, CW	6720	A
Steel sheet	Width × Length	150 × 150	mm^2
Material: steel_1010	Thickness	10	mm
(* Sweep variable)	Vertical gap *	$-75 : -25 : -250$	mm
Analysis setup	Mesh: Length-based element max.	10	mm
	Percent error	0.01	%

steel_1010 is available in ANSYS Electronics material library.

A.6 SolidWorks: Stress Analysis on Steel Table



(a) (b)

Figure A.6: SolidWorks stress analysis setup. **(a)** Vertical force 7200 N. **(b)** Model mesh.

Table A.6: Simulation settings: Steel Table with Vertical Load in Figure 4.11.

SolidWorks stress analysis simulation parameters		**Value**	**Unit**
Material: ASTM A500 grade B Cold-Rolled Steel (HSS: Hollow Structural Steel)			
	Mass density	7850	kg/m^3
	Elastic modulus	1.99×10^{11}	N/m^2
	Shear modulus	7.72×10^{10}	N/m^2
	Tensile strength	4.00×10^{8}	N/m^2
	Yield strength	3.17×10^{8}	N/m^2
Analysis setup	External load (Vertical: $-Z$ direction)	7200	N
	Mesh: Curvature-based mesh		
	Max element size	2.03	inch
	Min element size	0.41	inch

Appendix B

List of Publications

B.1 Published Journal Articles

1. Chanuphon Trakarnchaiyo, Yang Wang, and Mir Behrad Khamesee, "Design of a compact planar magnetic levitation system with wrench–current decoupling enhancement," *Applied Sciences*, vol. 13, no. 4, 2023.
   DOI: https://doi.org/10.3390/app13042370

2. Xiaodong Zhang, Chanuphon Trakarnchaiyo, Heng Zhang, and Mir Behrad Khamesee, "Magtable: A tabletop system for 6-DOF large range and completely contactless operation using magnetic levitation," *Mechatronics*, vol. 77, p. 102600, 2021.
   DOI: https://doi.org/10.1016/j.mechatronics.2021.102600

B.2 In-process Journal Articles

1. Zhenchuan Xu, Chanuphon Trakarnchaiyo, Curtis Stewart, and Mir Behrad Khamesee, "Modular maglev: Design and implementation of a modular magnetic levitation system to levitate a 2D Halbach array".
   Submitted to *Mechatronics* on August 16, 2022 (Updated on August 17, 2023.)

2. Chanuphon Trakarnchaiyo, and Mir Behrad Khamesee, "A novel wrench–current decoupling strategy to extend the use of small lookup data for long-range maglev planar motor".
   Submitted to *Actuators* on July 28, 2023 (Updated on August 17, 2023.)